STUDY OF FROST GROWTH ON HEAT EXCHANGERS USED AS OUTDOOR COILS IN AIR SOURCE HEAT PUMP SYSTEMS

By

SANKARANARAYANAN K P

Bachelor of Engineering in Mechanical Engineering
Regional Engineering College
Durgapur, West Bengal, India
2001

Master of Science in Mechanical Engineering
Oklahoma State University
Stillwater, Oklahoma, USA
2005

Submitted to the Faculty of the
Graduate College of the
Oklahoma State University
in partial fulfillment of
the requirements for
the Degree of
DOCTOR OF PHILOSOPHY
May, 2011

STUDY OF FROST GROWTH ON HEAT EXCHANGERS USED AS OUTDOOR COILS IN AIR SOURCE HEAT PUMP SYSTEMS

Dissertation Approved:

Dr. Daniel Fisher

Dissertation Adviser

Dr. Jeffrey Spitler

Dr. Lorenzo Cremaschi

Dr. A. H. Johannes

Dr. Mark. E. Payton

Dean of the Graduate College

ACKNOWLEDGMENTS

Mere words are not enough to convey my gratitude to Dr. Daniel Fisher, my graduate school advisor. He has given life to the term 'advisor' by being a teacher and a friend not only in the academic matters but in personal matters also. His positive outlook, optimism and friendly nature taught me how to be a good researcher and above all a good person. My transformation from a computer programming hater to a programming enthusiast is all due to his encouragement and training. One day I wish to be as good a programmer as your are, Dr. Fisher.

My PhD project was co-advised by Dr. Lorenzo Cremaschi who really helped me get interested in the refrigeration systems. I learned a lot from his hard work and meticulousness. He was very friendly and approachable when ever I went to him with problems.

A big part of my studies at Oklahoma State University was influenced by Dr. Jeff Spitler. The courses I took with Dr. Spitler and discussions I had with him are among the best training I had in my entire academic life. I learned a lot from him on how to look at an engineering problem from a research perspective.

Many thanks go to Dr. A. J Johannes for being in my dissertation committee. His different perspective on the material I presented for Preliminary and Qualifier exam enabled me to think about some issues I would never have thought.

I would like to acknowledge the financial support from the Oklahoma Center for Advancement of Science & Technology (OCAST). I would also like to acknowledge the technical and financial support from Heat Transfer Center of Excellence of Johnson Controls Inc. Dr. Calvin Iu at HT CoE - JCI was very helpful in getting me up to

speed with their simulation code and explain various topics related to the heat pump design.

As is the case with any academic project, this work is also influenced a great deal by many friends and colleagues. Thanks go to my lab mate Ehsan Moallem for being tough and critical during meetings. Your insight and help is very much appreciated. I am also indebted to numerous other people who helped in building and running the experimental facility; especially Chris Carrol, Shanshan Cai and Tommy Hong. Word of thanks will not do justice to the friendship I had with Edwin Lee, my ERL office mate who, during our coffee breaks, taught me so much about computer programming. I would also like to extend my thanks to all my other friends in Stillwater who made the weekend gatherings memorable. I wish you guys all the best this life has to offer.

This dissertation would have been impossible if not for the complete understanding and sacrifice of my beloved wife Divya Krishnan. She was such a source of support for me to finish this milestone. My thanks also goes to my Sister Radha and my brother Harish for their support and encouragement.

My parents, Sri Padhmanabhan and Smt. Lakshmy, sacrificed every joy in their youth to bring three of us up and give us a good education. If not for their selfless sacrifice I would not be standing here with this academic achievement. My father always used to tell us that education is the best asset one can earn. I hope I have fulfilled his wish. I dedicate this dissertation to my parents without whom this endeavor would have not been possible.

Last but not the least, I would like to thank God Almighty for giving me inspiration and support during difficult times.

TABLE OF CONTENTS

LIST OF TABLES

LIST OF FIGURES

Figure Page

Nomenclature

Variables

$\dot{m}$	Mass flow rate (kg/s)
$\dot{Q}$	Heat transfer rate (W)
$\dot{V}$	Volumetric flow rate [m^3/s]
σ	Area ratio in pressure calculations
A	Area (m^2)
$A_{br,coil}$	Coil Bare Tube Area $[m^2]$
$A_{o,coil}$	Coil Total Outside Area $[m^2]$
C_p	Specific heat$(J/kg - /k)$
COP	Coefficient of performance
D	Diameter (m)
D_h	Hydraulic Diameter [m]
D_{AB}	Binary diffusion coefficient (m^2/s)s
e	Error in measured variable
f	Friction factor
F_d	Fin/Tube Depth [m]
F_p	Fin Spacing [m]
Fo	Fourier number
G	Mass flux $(kg/m^2 - s)$
H	Fin Height [m]
h	Heat transfer coefficient $(W/m^2 - K)$
h_m	Mass transfer coefficient (m/s)
h_{sg}	Latent heat of ablimation (J/kg)
HP	Heated perimeter (m)

i Enthalpy (J/kg)

Ja Jacob number

k Thermal conductivity $(W/m-K)$

K_i, K_e Inlet and exit coefficients

L_l Louver Length [m]

L_p Louver Pitch [m]

L_α Louver Angle $[^o]$

N_r Row Number

Nu Nusselt number

P Pressure (Pa)

P_f Fin Pitch [m]

P_r Row Pitch [m]

$P_{f,ref}$ Reference Fin Pitch [m]

Pr Prandtl number

R Specific gas constant for water vapor$(J/kg-K)$

Re Reynolds number

RH Relative humidity []

S_{fi} Fin spacing (m)

St_k Stanton number based on frost roughness

T Temperature (C)

t Time (s)

T_p Tube Pitch [m]

u Velocity in axial direction (m/s)

WP Wetted perimeter (m)

Y Dimensionless coordinate

y Dimensional coordinate (m)

$y(t)$ Roughness of frost layer

Greek Symbols

β	Empirical constant used for frost conductivity
δ	Thickness (m)
η	Fin efficiency
γ	Kinematic viscosity (m^2/s)
λ	Parameter used in fin efficiency calculation
μ	Dynamic viscosity $(Pa-s)$
ρ	Density (kg/m^3)
θ	Dimensionless temperature

Subscripts

∞	Bulk air
a	Air
$cond$	Conduction
$diff$	Diffusion
f	Frost
fi	Fin
fs	Frost surface
i	Grid counter
l	Latent
r	Refrigerant
s	Surface, Sensible
$surf$	Surface
tp	Triple point
v	Vapor

CHAPTER 1

INTRODUCTION

1.1 Introduction

Air-to-Air heat pumps provide cooling and heating to conditioned spaces by transferring heat with the ambient (outdoor) air. Such heat pumps typically work in a vapor compression cycle with two air-to-refrigerant heat exchangers; one of them in the conditioned space and one in outdoors. In cooling mode the indoor heat exchanger acts as an evaporator, while the outdoor heat exchanger is the condenser. In heating season the two heat exchangers switch roles and the indoor heat exchanger is the condenser while the outdoor heat exchanger works as an evaporator. Refrigerant in the evaporator operates at a lower temperature than the ambient air. In cooler climates during the heating season when the outdoor temperature is usually around (or below) freezing, the operating temperature of outdoor coil is typically below freezing. If the surface temperature of outdoor coil falls below the dew point of the incoming air, water vapor in the air starts to condense and if the temperature is below freezing, the condensed droplets start to freeze on the heat exchanger surfaces. Growth of frost on heat exchanger surfaces results in deterioration of the heat transfer performance. Energy has to be expended at regular intervals to remove the frost and as a result overall efficiency of the heat pump is affected.

Frost growth affects the heat pump performance by four different mechanisms. First

the frost layer on the heat exchanger acts as an added resistance to the heat transfer, which contributes to low performance. Secondly, frost layer also decreases the free flow area of the coil and thus the velocity of air is increased. This mechanism increases the heat transfer performance. Thirdly, the growth of frost on the heat exchanger surface increases the air side pressure drop and thus increases fan power. The fourth mechanism is a direct result of increased pressure drop and use of a constant speed fan for the outdoor coil. With an increased pressure drop, the operating point of the fan will ride down the fan curve thereby reducing the air flow rate across the coil. A decrease in air flow rate directly translates to a reduced heat transfer rate. In real operating conditions the first and fourth effects dominate compared to the second effect. Thus, overall growth of frost is detrimental to the heat pump performance.

Due to higher energy efficiency requirements, the heat pump industry is motivated to go to microchannel technology. Microchannel heat exchangers provide higher capacities with significantly lower coil area. Thus microchannels reduce the cost of the unit due to reduced material cost and also reduce operating costs due to higher efficiencies. While microchannels have been successfully implemented on the condenser side of air-conditioners, their applicability in heat pumps has still not been achieved. As described before outdoor units in heat pumps face frosting problem when used in cooler climates. In microchannels it is observed that the problem of frosting is even more serious and the rate of frost growth is significantly higher compared to conventional fin and tube coils. As a result defrost cycles will increase which amounts to reduced overall capacity of the unit. The heat pump industry is not yet able to justify using microchannel technology due to the reduced energy efficiency in the heating season even though the cost is significantly lower.

Frost growth, is a complex phenomenon with combined transient heat and mass

transfer. The problem is complicated by the moving boundary which occurs during frost growth. A comprehensive treatment of frost growth is difficult given the large number of variables that contribute to the effect. Fundamental research to understand the phenomenon is limited to simple geometries. The present work is focused on developing a model for frost growth which can be used in conjunction with a transient heat pump simulation program for air-to-air heat pumps. The objectives and unique contributions of current research are presented in the following sections.

1.2 Objectives

The present research is motivated by the need to incorporate a microchannel heat exchanger in the outdoor unit of a heat pump. The objectives of current research can be categorized as follows:

1. Develop a mathematical model for frost growth that can be used for both fin-tube and microchannel heat exchangers. This includes extensive review of literature for existing models.

2. Conduct experiments to obtain frost growth data for microchannel and fin-and-tube HX. The objective of the experimental data would be to validate the new frost growth model.

3. Incorporate the frost growth model for fin-and-tube and microchannel heat exchangers in a whole system simulation program.

A detailed literature review concerned with frost growth is presented in Chapter 2. An experimental facility designed for the purpose of heat exchanger frost growth experiments is described in Chapter 3. Chapter 3 also describes frost growth

experiments on fin-tube and microchannel heat exchangers. Chapter 5 describes frosting experiments on heat pumps conducted to study the effect of frost growth on the system parameters. A mathematical model for frost growth is presented and its basis is discussed in Chapter 4. Results obtained from the model for stand alone coil are also presented in Chapter 4 along with its validation against the measurements obtained from experiments. Chapter 6 presents the plan for future research.

1.3 Unique Contributions

The main contribution of this research is an experimentally validated frost growth model that can be applied to both fin-tube and microchannel heat exchangers. Major contributions that will be produced from this research are enumerated below.

1. While numerous models for frost growth exist for flat plate geometries and a few for fin-tube heat exchangers, no model exists in the literature that has been successfully demonstrated for use with microchannel heat exchangers. Models available for fin-tube heat exchangers are based on finite difference or finite volume solution methods. Such models are not suitable for application in a system simulation environment due to the high computational overhead. This research will develop a new frost growth model applicable to both fin tube and microchannel heat exchangers.

2. A second contribution of this research is the development of a quasi-steady state system simulation to support the frost growth model. Successful implementation of a transient frost growth model in a steady state heat pump simulation environments is achieved by modifying an existing steady state algorithm. Since dynamics introduced by frost growth are slow compared to the dynamics of the vapor compression system caused by compressor, it is

reasonable to use a quasi-steady state algorithm. The advantage of such an approach is that it can be accomplished by modifying an existing simulation program. This development will make it possible to evaluate the effects of frost growth on system performance. The governing equations are studied analytically and a necessary condition that allows quasi-steady assumption is derived.

3. Heat exchanger will be discretized in the direction of air flow to account for variation in frost profile. This will help in predicting the frost weight and outlet air conditions more accurately. The knowledge of amount of frost on the heat exchanger is important to determine the amount of energy that needs to be spent in defrosting.

4. Air side effects due to non-uniform frost growth have been ignored by previous studies. The model presented in this study will take into account the air-side effects of non-uniform frost growth. Redistribution of air flow on the face of the coil will be accounted for by a pressure equalization algorithm and its associated effects on heat exchanger performance will be analyzed.

5. Finally experimental data sets for frost growth on both fin-and-tube heat exchangers (available in literature) and microchannel heat exchangers (not available in literature) will be developed. Important parameters such as frost thickness at different locations, frost weight and heat exchanger performance will be measured. Such data sets can be used in future studies.

CHAPTER 2

LITERATURE REVIEW

Research into the phenomenon of frost growth has been carried out by numerous researchers starting as early as the middle of 20^{th} century. Most of the research until last decade primarily focused on understanding the characteristics of the frost layer and its growth on flat plates. Since mid 1980s focus of frost research shifted heavily to geometries which are applicable to heat exchangers. Frost growth models for geometries such as plate fin and conventional fin-tube were developed. The approach undertaken by most researchers is to start with the basic differential equations for heat and mass transfer and solve them analytically with the use of heat transfer coefficients obtained from experiments. Review of frost growth research can be classified into three broad groups viz.

1. Characteristics of frost growth: This group deals with the determination of physical properties of frost layer like density, conductivity, porosity etc. Every publication in this group is aimed in developing a correlation for the required quantities based on experiments.

2. Frost growth on flat plate: The rate of frost growth and factors affecting the frost growth are the major questions answered in this group of publications. Both experimental and numerical approaches are undertaken by researchers.

3. Frost growth on heat exchanger geometries: Geometries that are applicable for heat exchangers are considered in this group. Approach taken is mostly

semi-analytical with support from experimental data.

In this chapter important work done in each group mentioned above is discussed. Focus is given on the approach taken and major conclusions drawn from each work.

2.1 Characteristics of Frost Growth

Yonko and Sepsy (1967) worked on thermal conductivity of the frost layer. They presented both analytical analysis and empirical correlations. Empirical correlation for thermal conductivity was presented as function of frost density. The correlations were developed based on the experiments performed by the authors. Authors also presented different correlations from previous researchers. While the correlation for frost conductivity contained only frost density, the spread in the experimental data was explained by the authors to be a result of difference in macroscopic structure of frost. As a supporting point to their claim, authors demonstrated that two frost layers of same thickness but different internal build up had different thermal conductivities using a simple compound wall approach. Though convincing the authors did not provide any theoretical evidence regarding the effects of macroscopic structures.

Brian et al. (1969) conducted experiments to determine the characteristics of the frost layer. Properties of frost layer such as density and conductivity were correlated as functions of the stream variables such as humidity, Reynolds number and time since the start of frosting. An experimental set up with a flat copper plate maintained at cryogenic temperatures was used and humidified nitrogen gas is blown so that forced convection is dominant. Authors observed that whole process could be divided into two parts. In the first part, frost layer grows gradually and as a result decreasing heat transfer rates and increasing frost surface temperature. In

the second part heat transfer rate and frost surface temperature remains constant even though frost thickness increases. This observation is quite different from expected behavior since it is expected that thicker frost decreases the overall conductivity and heat transfer rates should drop. Authors supported this claim by arguing that in the second part density of frost increases (increasing conductivity) which will compensate any increase in resistance due to thickness. Results reported were measured during the second part. Uniform thickness was assumed to exist on the test apparatus, which was measured using a micrometer. The density was measured indirectly from the thickness data and weight of frost. Authors also reported the temperatures of frost layer at different heights from the plate. It was shown that the rate of change of temperature at layers near to the cold plate is high and in the outer layers the temperature change is less. Frost thickness was found to increase with increasing humidity and decreasing Reynolds number. Authors also found that an increase in density resulted in an increase in conductivity. Models for frost density and frost conductivity were also proposed which showed good agreement with the measured data.

An experimental study to relate frost thermal conductivity to the type of frost was done by Hayashi et al. (1977a). The facility was designed to vary the plate temperature ($0\ to\ -25^oC$), air absolute humidity ($0.0045 - 0.01$) and air velocity ($1\ m/s - 6\ m/s$). The objective was to classify the frost formation types and then to correlate frost characteristics (conductivity and density) based on these frost formation types. Classification was based on the photographic observations made during different times of frost formation. Authors classified frost formation into four major groups based on the plate surface temperature and concentration difference between air and the surface. Each group was further classified into subgroups depending on the shape of the frost at its initiation. Authors noticed a parabolic relation between frost density and time at any surface temperature. However, the

rate of change of frost density in the initial stages were remarkably different for different frost formation types. Experimental results were published for conductivity of frost as a function of density. An expression for effective thermal conductivity of frost was presented based on the structural analysis of frost. The authors did not the present the method used for data reduction for thermal conductivity and also did not present any uncertainty in the heat flux.

Hayashi et al. (1977b) used the same experimental setup used by Hayashi et al. (1977a) to develop a frost growth model. From the photographic observations, they classified the total time for frost growth into three periods, viz. Crystal growth period, Frost layer growth period and Frost layer full growth period. The authors suggested that the second period called '*frost layer growth period*' is the most important of the three. The analysis was based on frost deposition on a cylinder. This approach was a result of the assumption that frost columns existed at the beginning of frost layer growth period. Considering the frost pattern after crystal growth period as hollow cylinder, the frost growth during frost layer growth period was treated as a three dimensional diffusion problem. Model presented in the paper cannot be effectively used in a simulation program since many parameters (heat and mass transfer related coefficient) used by the authors are obtained from experiments they performed. Authors presented plots showing the variation of frost height with time. It was observed that the results are improved by accounting for the variation in frost density. Based on the experimental data a correlation of frost density was presented as a function of surface temperature.

Auracher (1987) attempted to quantify the effects of all modes of heat transfer occurring in a frost layer. The objective was to come up with an expression for thermal conductivity with the consideration of radiation, convection, conduction and diffusion. Author presented the data obtained from experimental setup, which

was designed to isolate the effects of each of the mechanism. Each mechanism is separately analyzed and an order of magnitude analysis performed to determine the contribution. Effects of radiation on the conductivity of the frost was found to be negligible (about 1% of the effective thermal conductivity). Natural convection could occur inside frost layer depending on the geometry and temperature of frost layer. However, it was noted by the author that in order to have significant contribution from natural convection the temperature gradient needs to be high which normally is not the case inside a frost layer. Thus it was mentioned that natural convection inside frost layer can be neglected. It was concluded that the thermal conductivity is affected mainly by diffusion and conduction. Since no details were provided regarding the experimental setup the correlations presented for thermal conductivity should be used with caution.

A model to determine the thermal conductivity of frost was developed by Şahin (2000). Analysis followed in the paper deals with the frost forming during early crystallization stage. The work was motivated in part to confirm the hypothesis that thermal conductivity of frost is not a function of density alone, at least in the early stages. It was the opinion of the author that the characteristics of frost is highly dependent on the temperature of the surface at which frost formed. While frost is made up of ice crystals and void spaces trapped in between the crystals, for modeling purposes it was divided into columns of packed ice and air. A one dimensional heat transfer and mass diffusion was assumed in the frost layer. In developing the model, a new parameter called volumetric ratio, which is ratio of volume of ice to the total volume (ice and air void) was introduced. An energy and mass balance on the control volume containing frost(ice crystal and air surrounding) was formulated. The formulation presented itself similar to the heat conduction equation. The coefficient term for temperature gradient is then defined as the conductivity of frost (ice and air void). It could be seen that the equation obtained

for conductivity takes a form of volume averaging of the conductivities of ice and air with an additional term. This additional term accounted for added density due to diffusion of water vapor into the frost layer. From the resulting equation, an expression for local frost conductivity is obtained. With the local frost conductivity, the author derives an expression for effective thermal conductivity of entire frost layer by integrating it for the thickness of the layer. The model showed that the effective thermal conductivity of frost layer is higher when the temperature at which frost formed was higher. Results were also reported for different air temperatures, air humidity ratios and Reynolds number. From the numerical results the authors concluded that the frost conductivity depends on all frost layer properties and not the density alone. This was especially true in early growth stages. It has to be noted that the development of model is based on a structure of layer which exists only in the early stages of frost initiation and as such the efficacy of model in later stages of frost growth is suspect.

Yun et al. (2002) took a different approach in developing the heat and mass transfer correlations related to frost growth. Correlations for density, thermal conductivity, heat and mass transfer coefficients were developed based on the frost surface roughness. Experiments were carried out at controlled air temperature and humidity to obtain various quantities such as frost thickness, frost weight, rate of heat transfer etc. They defined surface roughness as 'difference between hill and valley of frost'. Roughness of frost layer was measured using a precision micrometer. A correlation was presented for calculating the roughness value as a function of time. Roughness correlation had a high error ($\pm 20\%$) associated and is a function of time alone. Though such a model might be applicable in a frost model, the correlation presented in the paper is very specific to geometry and location of frost growth and thus is not useful in a heat pump simulation. In order to efficiently use the roughness data, authors used the modified Prandtl mixing-length approach.

Turbulent boundary layer thickness along with roughness value was used to correlate friction factor. Further authors used the friction factor values to correlate heat transfer coefficients. In addition to roughness value (in form of friction factor) Reynold's number and Prandtl number was also used in heat transfer correlations.

Quite a bit of work has been done in the past in determining the frost characteristics such as density and conductivity. Most of the work was based on experimental approach to calculate density and use theoretical modeling to correlate conductivity. A general form that is established and accepted is that frost density is a function of frost surface temperature and frost conductivity is a function of density. Though it is generally accepted that frost density is a function of frost surface temperature and frost conductivity is a function of frost density, no consensus exists on what the form of correlation should be.

2.2 Frost Growth on Simple Geometries

First attempt to address the need for a model which can handle changes in environmental parameters was done by Jones and Parker (1974). Authors expressed the time rate of change of frost density and frost thickness in terms of environmental parameters, frost surface temperature and spatial rate of change of surface temperatures. Temperature and spatial change of temperature at frost surface were obtained by application of heat balance at the surface. The model behaved very well under different conditions due to the first principle approach. Since the resulting equations are singular when frost density and thickness are zero, which happens during initiation of frost growth, model will depend heavily on initial assumptions of frost density and thickness. These guessed values can be made better by performing a parametric analysis. Parametric analysis was performed by varying frost thickness and frost density within ranges and checking against numerical stability. It was

found that the initial value of frost thickness can be as small as 2×10^{-5} m. Authors recommended that a density value which is significantly lower than actual frost density value will be acceptable but did not provide a specific value or range.

Schneider (1978) conducted frosting experiments using cylindrical tube. The experiments covered a range of Reynolds number, air temperature, air relative humidity and surface temperature. Experiments were targeted towards developing correlations for thickness of frost layer as a function of experimental variables. Author presented three different correlations based on different assumptions. It was observed from the experiments that frost thickness was not dependent on the Reynolds number. The data presented by the authors also showed that the frost thickness is not influenced by the difference in vapor pressure in air and frost layer. These observations was in direct contradiction to previously published studies which claimed frost growth is significantly affected by parameters such as Reynolds number and vapor pressures in air and frost surface. A maximum error of $\pm 10\%$ was reported between the correlation and experimental data, while authors claim a 'probable'error of $\pm 3.7\%$. The error values reported are questionable since the authors did not mention the approach taken for measurement in their experiments. Uncertainties in their measurements were also not reported.

An experimental study on the frost growth on flat plates under forced convection was studied by Östin and Andersson (1991). The experimental variables that were controlled were plate temperature, air relative humidity and air velocity. Measured variables included frost thickness, frost mass and surface temperatures. Average density was calculated using measured values for thickness and frost weight. Authors measured thermal conductivity of frost by solving a one-dimensional transient heat conduction equation. It was observed and reported that the plate temperature had negligible effect on the frost mass, while the thickness increased

with decrease in plate temperature. As the relative humidity changed however it was noted that both frost mass and frost thickness increased. However for all cases frost mass and frost thickness increased with time. A preliminary check for the experimental data, using a simple model available in literature showed the data to be within ±10%. There were two interesting observations made by the authors. First observation was that there are two conspicuously different trends for increase of frost density with time. It was observed that the frost density increased linearly until some time and stayed constant for some time. After that the density again started to increase linearly. The region where frost density did not changed was called as 'plateau'. Second interesting observation was regarding the frost thermal conductivity. It was reported that frost thermal conductivity increased with frost thickness until some thickness after which there was a sudden increase in thermal conductivity. The thickness where conductivity increased suddenly coincided with the 'plateau'. Both these observations were attributed to the possible melting and refreezing of frost layer which happens when the frost surface temperature reaches the triple point of water.

A numerical model based on volume-averaging technique was proposed by Tao, Besant and Rezkallah (1993) to determine the frost density and frost thickness. The model is useful only in frost layer growth period as defined by Hayashi et al. (1977a), and cannot be applied during the initiation stage. Model relied on determining the volume fraction of ice and air-water vapor mixture using the gas relationships. Authors suggested that the densification (increase of frost density with time) is dependent on the frost structure during early growth period; this is consistent with other researchers. They claimed that the temperature and density at different frost depths vary almost linearly, with temperature showing higher linearity. Temporal variation of heat flux was reported for two different plate temperatures. It was shown that for lower plate temperatures the heat flux drops

faster. The frost surface rises sharply for low plate temperatures thereby reaching the triple point temperature quickly. Results consistent with other researchers for frost thickness were also reported. The value used by many authors for diffusivity of water vapor in air was questioned by the authors and they suggested that the effective diffusivity could be as much as 7 times higher.

Le Gall et al. (1997) presented a method to model frost growth in the period after the initial crystal growth phase. In order to accomplish this the governing equations were solved using 'Local Averaging Technique' method. In such a method the total domain of solution is divided into different control volumes. Any property is calculated for that control volume and for the whole volume an average volume is calculated by weighting the local property with the local volume. Frost layer was assumed to be a 1-dimensional pseudo homogeneous medium. Their study contained both theoretical and experimental components and they also attempted validating the model using experimental data from other researchers. Authors used the frost condition at the end of initial crystal growth phase as initial condition for their model. Frost layer was assumed to be fully grown when the frost surface temperature reaches triple point of water. This assumption is used and reported by previous researchers. It was noted by the researchers that significant error could result from a bad estimate of diffusion coefficient. It was argued by the authors that use of diffusion coefficient obtained from Fick's law results in gross errors. Reason for this discrepancy were identified as the complex mechanism and effects of heat transfer and mass transfer on each other. Fick's law simplifies the problem by assuming that heat transfer does not affect the accompanying mass transfer. A correction term (termed as Diffusion resistance factor) was introduced to the value of diffusion coefficient obtained by Fick's law in order to match the experimental observations.

Na and Webb (2004*b*) developed governing equations for frost growth based on a control volume approach. Following an earlier paper by the same authors[Na and Webb (2004*a*)], the frost surface is considered to be supersaturated. Air is said to be supersaturated at frost surface when the local vapor pressure is higher than the saturation vapor pressure at the surface temperature. This necessarily means that water vapor is highly unstable in its gaseous state and condenses very fast. Experiments were performed to correlate thermal conductivity of frost. Frost thickness was determined by measuring with a micrometer. Data was taken at intervals of 10 - 30 minutes. In heat pump applications this interval is pretty big considering the fact that the frost cycles are shorter compared to some other applications. Thermal conductivity was expressed in terms of weighting factor as defined by Sanders (1974). Weighting factor is defined as a numerical value which is used to calculate the thermal conductivity given the maximum and minimum values. In order to be able to predict varying thermal conductivity, the weighting factor needs to be varying as frost grows. Weighting factor was determined from the experimental data and presented as correlations against frost base surface temperature. In order to solve the governing equation they used initial condition for frost density as specified by Jones and Parker (1974). Authors compared the prediction of the saturated model and the super saturation model against the experimental data. It was reported that saturated model over predicts the frost growth rate by 50%.

Lee and Ro (2005) proposed two models to predict growth of frost on a flat plate; one in which water vapor was assumed to be saturated at frost layer, while in the second model water vapor at frost surface was assumed to be super-saturated. Authors presented a detailed treatment of governing equations along with a computational procedure to solve the equations. It was observed that solution to governing equations were affected by the initial value of frost thickness and frost

density. The dependence on frost density was found to be more significant than frost thickness. Authors reported satisfactory results could be obtained by using an initial frost thickness value as low as $2.0 \times 10^{-5} m$. It was reported that no initial value of frost density resulted in a good match to experimental data. This observation was in line with most other researchers where an agreement on acceptable initial guess is not available. Also presented were the effects of environmental parameters such as air humidity ratio, plate temperature, air temperature and air velocity. Results consistent with previous works were obtained. While the simple model (saturation model) gave acceptable results, authors presented the effect of using a detailed model with different degrees of supersaturation. It was observed that as the degree of supersaturation degree varied from 0 to 1, error due to results from model decreased first and the increased. Thus it was clear that correct value of degree of super-saturation needs to be used to obtain the benefits of detailed model.

Most of the work done is done for flat plates with a few papers available for frost growth on cylinders. While dealing with frost growth model on flat plates or cylinders, the split between theoretical modeling and experimental approach seems equal. Theoretical approach undertaken by most researchers is to discretize governing partial differential equations. Discretized equations are then solved using finite difference or finite volume approach. Only a few papers are published which provide closed form solutions for governing equations. It is noted and accepted in the literature that the phenomenon is too complex to present itself a closed form solution.

2.3 Frost Growth on Heat Exchanger Geometries

Hosoda and Uzuhashi (1967) conducted an experimental study using fin-tube heat exchangers. Objective of their study was to develop equations pertaining to

properties such as density and conductivity of frost layer growing on a heat exchanger surface. In addition to the aforementioned objective, authors also developed correlations for heat transfer and pressure drop across heat exchangers. An experimental setup was used to study the effects of varying air temperature, air humidity and fluid temperature. Authors measured and used air velocity values in their correlations. Frost growth was quantified by measuring the weight of accumulated frost. Method used by the authors was not sophisticated; accumulated frost was scraped and collected in a pan and weighed separately. Authors presented theories regarding the development of frost based on air and plate temperatures. They claimed that at comparatively low air temperatures ($0 - 10^oC$) and high relative humidities ($> 70\%$), major factors affecting growth of frost were plate temperature and wind velocity. Low density frost grows at low temperature and low wind velocity, while at high plate temperature and higher wind velocities a high density ice-like frost is the result. Correlations presented for heat transfer and pressure drop do not reflect the physics of the problem since the parameters correlated are dimensional. It has to be kept in mind that since these correlations are highly dimensional, it's use for heat exchangers different from those used by authors might result in incorrect results.

Barrow (1985) studied frost growth on heat exchanger surfaces with and without fins. This paper studies the reason for capacity degradation during frosting. Four different possibilities are evaluated viz. increase in roughness, reduction in air mass flow, insulating effect of frost layer. While the first two increase the heat transfer the last two phenomenon tend to reduce the heat transfer rate. Of these reduction in air mass flow is found to have maximum effect. A revolutionary claim by the researchers is that the insulating effect of frost layer is of least impact. Comparison of effect of frost on flat plate and finned plate is carried out. Authors concluded that the knowledge of frost characteristics is more important only in flat plates and for

heat exchangers it is more useful to study the overall effect with the associated fan.

Effect of frost growth on performance of heat pump system is studied using a commercial unit by Ameen (1993). Simulation model based on different correlations developed previously was used to compare against the experimental results. Experiments were conducted for same air inlet temperature and different air relative humidities. It was reported that as the relative humidity was increased, the amount of frost growth also increased. During the frost growth period, the capacity of evaporator for higher humidity conditions is higher at initial period, and low at later stages. This is because higher humidity levels result in higher heat and mass transfer initially and also causes higher rates of frost growth, which deteriorates heat transfer characteristics. Simulation results are compared to experimental observations and values such as frost weight, heating capacity, COP and evaporator temperatures are reported. While the general trends matched reasonably well, it lacked in predicting certain characteristic features. Experimental observations showed that frost growth rate is higher at initial stages and flattened out later in the cycle. Simulation results however showed a steady increase in frost growth. Simulation also did not capture the initial enhancement in heat transfer which is observed commonly.

Thomas et al. (1999) and Chen et al. (1999) described an experimental facility designed to perform frost experiments. The facility had the ability to vary the temperature of base plate ($-35^oC\ to\ -40^oC$), air temperature ($-10^oC\ to\ -20^oC$) and air relative humidity ($80\% - 100\%$). An automated laser scanning system was used to measure the thickness of the frost growing on the fin surfaces. Fins were placed in pre-etched slots on the base plate. After each test fins were removed and then weighed separately. This method, as per the authors claim enabled them to determine the frost mass accumulation distribution. Other variables of interest like heat transfer rate and pressure drop were also measured. Two different tests with

different air temperature and humidity ratios were reported. Authors presented the contour, point and orthographic plots as obtained from laser scanner. A thicker frost was found to form near the leading edge and base of the fin. It was also noted that the rate of drop in frost thickness is higher in a direction normal to air flow (parallel to cold base), while the rate of drop in direction of air flow was found to be less. The frost surface was found to be smoother in higher humidity tests. For each fin using the measured values of accumulated frost mass and thickness were used to determine density. An uncertainty of 14% for density calculation was reported by the authors.

A numerical model along with the validation was presented by Chen et al. (2000*a*) and Chen et al. (2000*b*). Model was built based on 2-D transient heat transfer in fins and 1-D transient heat transfer in frost layer. Air flow rate was assumed constant and the air side condition was assumed to be turbulent. Model aimed to predict frost parameters such as frost height, density and heat exchanger parameters such as heat transfer rate and pressure drop. Model results reported by the authors were acceptable for frost parameters and heat transfer rate. Though authors did predict the pressure drop, it was found very sensitive to frost layer thickness such that even a slight error in thickness prediction would throw pressure drop prediction into unacceptable values.

Storey and Jacobi (1999) studied the effect of streamwise vortices on frost growth on fins. Authors presented both experimental findings and also theoretical treatment of frost growth. They proposed a simple scaled form of energy balance at frost surface which after making a few assumptions can be solved to get frost thickness at any time. Dimensionless frost thickness was shown to vary as the square root of environmental time (dimensionless time). Environmental time was defined in terms of other dimensionless quantities such as Biot number (Bi), Fourier

number (Fo), Lewis number (Le) and time in seconds. In an attempt to relax the assumption of constant mass deposition on the surface which was not realistic, a follow up work was done by Robinson and Jacobi (2001). Authors started with the same heat balance equation as before but removed the assumption that amount of mass deposited is same through out the time period. The analysis resulted in a system of equation which could be solved to get frost thickness and frost surface temperatures. Even this work suffered from another major assumption; an assumption that all of the mass removed from air freezes on the surface . This is not a good assumption and could give higher frost surface temperatures. The model proposed in this work takes the work done by Storey and Jacobi (1999) as foundation and relaxes some of it's assumptions.

In the first of a two paper series, Seker et al. (2004b) described the development of a model for frost growth on fin-and-tube heat exchanger. The model was developed from basic energy and diffusion equations with the assumption that all frost properties are represented as average properties. This assumption lead to simplifications in the governing equations which lend itself to comparatively simple solutions. The experiments were aimed at studying the effect of frost on the heat exchanger performance (UA) and pressure drop. A parametric study was done by changing the air temperature, surface temperature, relative humidity of air and air mass flow rate. It was observed that increase in air temperature increased heat transfer coefficient, frost thickness and pressure drop for heat exchanger, while an increase in surface temperature decreased all three calculated variables. An increase in air relative humidity resulted in an increase in the heat transfer coefficient, frost thickness and pressure drop. Change in air mass flow rate produced results similar to those obtained by varying the humidity of air. In all of the model results it was noted that the UA of the heat exchanger increases with time, which is not consistent with many other investigators. In the second paper, Seker et al. (2004a)

reported the observations from an experimental facility designed to perform frosting tests on heat exchangers. The facility contained an environmental chamber maintained at test conditions. Air is drawn from the chamber into a duct which houses the test section. Experiments were conducted with constant air and heat exchanger temperatures and air relative humidity while varying air flow rate. The experiments were performed with two different heat exchangers having different fin pitches. The results from the experiments were not consistent with the model results. The authors claimed that it was due to the thin layer of frost present in experiments while the model assumed clean surface at the beginning.

In the first published work studying the frost growth in a commercially available heat pump unit, Kim and Groll (2003) compared conventional fin-tube heat exchangers and microchannel heat exchangers. The unit was tested with conventional fin-tube heat exchanger as base case. Further tests were conducted by replacing the outdoor coil with different heat exchangers. Study was targeted towards applicability of microchannel heat exchangers as outdoor coil in heat pump systems. This is one of the two papers which has direct bearing to the research proposed here. Authors compared baseline (conventional fin-tube HX) with five different microchannel heat exchangers installed in the outdoor unit of an heat pump. Effects of factors like fin density, heat exchanger inclination angle on the performance of whole unit was studied. Performance in both cooling and heating mode was studied. One of the important conclusions was with respect to the effect of fin density in microchannel heat exchangers. Contrary to published work till then, it was believed that increase in air side heat transfer area increases the performance. Authors found out that in angular configurations the fin density did not have any significant impact and even importantly in vertical arrangement lower fin density resulted in better cooling performance. Performance of units in heating mode was also studied and time between consecutive defrost reported for various

cycles. It was observed that time required to initiate defrost decreased in each subsequent cycle. It was hypothesized by authors that water retained in microchannel heat exchangers was the cause for faster defrost initiation. However it was also noted that keeping heat exchangers at an angle did not help frosting times. The reason suggested by the authors was that the surface tension of water droplets was greater than gravitational force even at an inclined configuration. The effect of fin density however had some effect on frosting times. It was seen that lower fin density reduced the speed of frost growth which is advantageous. In summary the conclusion of authors was that while microchannel heat exchangers are beneficial in cooling mode, its performance in heating mode is greatly reduced by faster frost growth. The paper did not provide any details about the frost growth parameters or related heat transfer and pressure drop relations. As a result it did not provide a good base to study frosting performance of microchannel heat exchangers.

Xia et al. (2006) presented one of the first paper which entirely focused on frost growth in folded fin flat tube heat exchangers. Such heat exchangers resembles microchannels on the air side. The study consisted of running 5 different heat exchangers in a controlled environmental chamber and allowing frost to grow. UA-LMTD method formulated by the authors in a previous paper [Xia and Jacobi (2004)] was used to calculate the air side heat transfer coefficient. Pressure drop across the heat exchanger is measured by differential pressure transducer. Frost thickness was measured using images captured by a CCD. Authors also presented a model for frost thickness at any given time. Presented results show that thickness obtained from images matched those from model reasonably well. From observations and analyzing images authors concluded that the method in which frost affected heat transfer is by converting louvered flow to duct flow by blocking louvers. Results consistent with other published work were noted with regards to heat transfer and pressure drop. Another important observation of authors was

regarding the manner in which frost growth takes place in subsequent cycles. It was observed that parameters related to frost growth become steady periodic after three or four cycles. Amount of frost collected in the heat exchanger during frosting period reached an asymptote value after 4 cycles. The initial increase in frost weight was attributed to water retention in the coils. After four cycles the amount of water retained was same in each cycle. Authors presented the variation of pressure drop in each cycle. It was seen that the pressure drop in each subsequent cycle increases until third cycle after which the value becomes constant. Though authors claim the reason is retained water, doubts arise due to the fact that the initial pressures for each cycle are approximately same.

CHAPTER 3

EXPERIMENTAL STUDY OF FROST GROWTH ON HEAT EXCHANGERS

3.1 Introduction

Frost growth experiments performed on a stand alone heat exchanger coil (both fin-tube and microchannel) will be presented in this chapter. The experiments were carried out at Oklahoma State University towards developing datasets that can be used for validation of frost growth model as applied to heat exchangers. Majority of frost growth studies has been related to frost growth in simple geometries such as flat plates or cylinders. This is due to the complexity and large number of variables present in an experimental procedure with frosted heat exchangers. The previous chapter reviewed the frost growth literature in detail. A brief discussion of relevant experimental work is presented in the following paragraph.

An extensive review of frost growth studies done for simple geometries is given by O'Neal and Tree (1985). Stoecker (1957) conducted frosting experiments on fin-tube heat exchangers under the conditions of constant air flow and varying air flow. Chepurnoi et al. (1985) studied the effect of various fin spacing on frost growth on finned air coolers. Frost growth rate and energy transfer potential of louvered fin-tube heat exchangers were studied experimentally under different air relative humidities, air face velocities and fin pitch by Kondepudi and O'Neal (1989). In a later study, Kondepudi and O'Neal (1991) studied the performance of heat

exchangers with wavy and corrugated fins under frosting conditions. Performance of heat exchanger was characterized on the basis of change in enthalpy potential during frosting. Thomas et al. (1999) and Chen et al. (1999) presented an experimental study to measure frost parameters on flat fins. They presented the variation of frost thickness along the depth of the fin. Overall heat transfer coefficient and pressure drop across a fin and tube heat exchanger with flat fins was studied by Seker et al. (2004a). The experimental results were compared to the values obtained from a simulation model presented in a previous paper by the same authors. Yan et al. (2005) presented an experimental study performed on a fin and tube heat exchanger under frosting conditions with three different fin types. Xia et al. (2006) studied the effect of frost, defrost and refrost on flat tube heat exchangers with folded fins. They presented a method to measure thickness of frost using images acquired by a CCD camera.

In many operating conditions the frost growth is not uniform along the length of the heat exchanger. Non-uniform frost growth on heat exchangers has been studied from a modeling perspective (Chen et al., 2000*a*; Tso et al., 2006; Yang et al., 2006b). However, all experimental studies performed to date consider the frost to be uniform on the face of the coil and apply the frost properties at a single measured location to the whole heat exchanger. Non-uniform frost growth results in a continuous redistribution of air flow on the face of the coil. Such a redistribution in the air flow will affect both the frost growth and the performance of the heat exchanger. Also using frost thickness at the measured location for the whole heat exchanger introduces error in the estimation of the overall heat transfer coefficient. In this chapter an experimental study of fin and tube heat exchangers that frost non-uniformly is presented. Frost growth profiles at different locations of the heat exchanger are presented. The overall heat transfer coefficient of the heat exchanger is calculated by taking into account the non-uniformity of frost thickness, and a

comparison to results obtained from a uniform thickness assumption is presented.

3.2 Description of the Facility

A facility was designed and built in the Advanced Technology Research Center (ATRC) at Oklahoma State University, Stillwater to perform frost growth experiments. Experimental facilities for studying the frost growth phenomenon on flat plates (Hayashi et al., 1977a; Östin and Andersson, 1991), cylinder (Lee and Ro, 2001) and other heat exchanger geometries (Thomas et al., 1999; Xia et al., 2006) are reported in literature. The variables that were varied in all the facilities included plate/fluid temperature, air temperature, air humidity and air velocity. The facilities described in the literature falls into one of the two categories viz. Tunnel based approach and Chamber based approach. Coil level frost growth experiments discussed in this chapter utilizes a tunnel based approach. A chamber based experimental set up will be discussed in 5.2 in the context of whole system experiments. The experimental facility, associated instrumentation, control and calibration procedures are discussed. A detailed uncertainty analysis for the measured and calculated variables is also presented. A detailed explanation of the design and construction of the facility is provided by Cai (2009).

The facility consists of a closed loop duct with a wind tunnel which will act as the testing section. The loop consists of fan, humidifier, cooling coil, turning vanes, heating coil, test coil, flow measuring nozzle and related instrumentation at different locations. A view of the test loop with major components is shown in Figure 3.1.

The test section consists of an inner duct of dimensions 1 ft×1 ft inside a 2 ft×2 ft outer duct. The idea of concentric ducts was adopted to give a guard space for temperature measurements. The test coil is placed in front of the inner duct and is

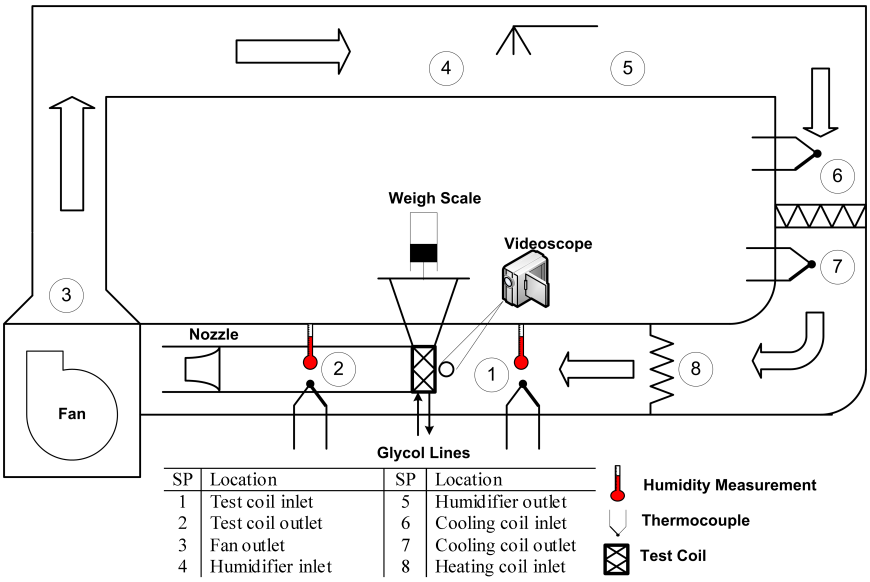

Figure 3.1: Schematic of the Air Loop

hung from a precision scale which will measure the weight of the coil throughout the duration of the experiment. A nozzle placed downstream of the coil is used for measuring the flow through the heat exchanger. The placement and specifications of the nozzle follows ASHRAE (2001). The test coil is attached to the inner duct using a thin plastic wrap so that all of the air flowing through the coil will enter the nozzle for flow measurement. Plastic wrap also allows free vertical movement of the coil for weight measurements. A detailed view of the test section is given in Figure 3.2.

An ultrasonic humidifier is placed in the duct to introduce moisture to the air stream. Cooling of air is achieved by a cooling coil through which Dynalene HC-50 is passed at low temperature. The dynalene is cooled by a low temperature chiller. The cooling coil is sized to have enough capacity so that exiting air is at saturated conditions at a temperature below the test setpoint. Flow through the coil is controlled to maintain the outlet humidity ratio at the test condition. Inlet dry bulb at the test coil is brought back to test condition by reheating the air with the help of a 1.4 KW electric heating coil. Output of heating coil is controlled by a variac. The process undergone by the air from the inlet of test coil to outlet of heating coil

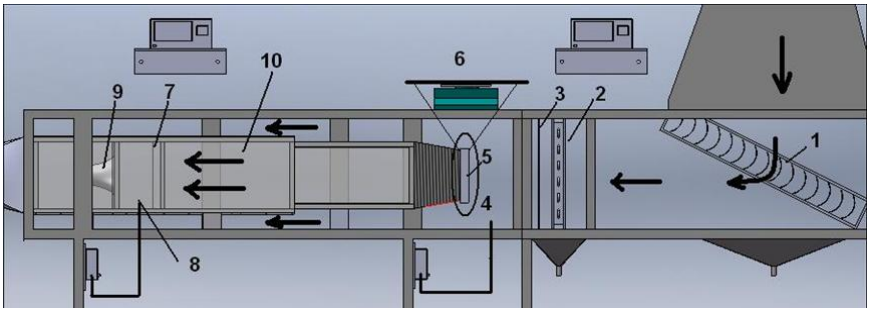

1	Turning vanes	2	Heating Coil
3	Inlet TC grid	4	Inlet dewpoint Sensor
5	Test coil	6	Precision weigh scale
7	Outlet TC grid	8	Outlet dewpoint sensor
9	Nozzle		

Figure 3.2: Detailed View of the Test Section

for a typical H2 condition specified by ARI (2008) is shown on a psychometric chart in Figure 3.3.

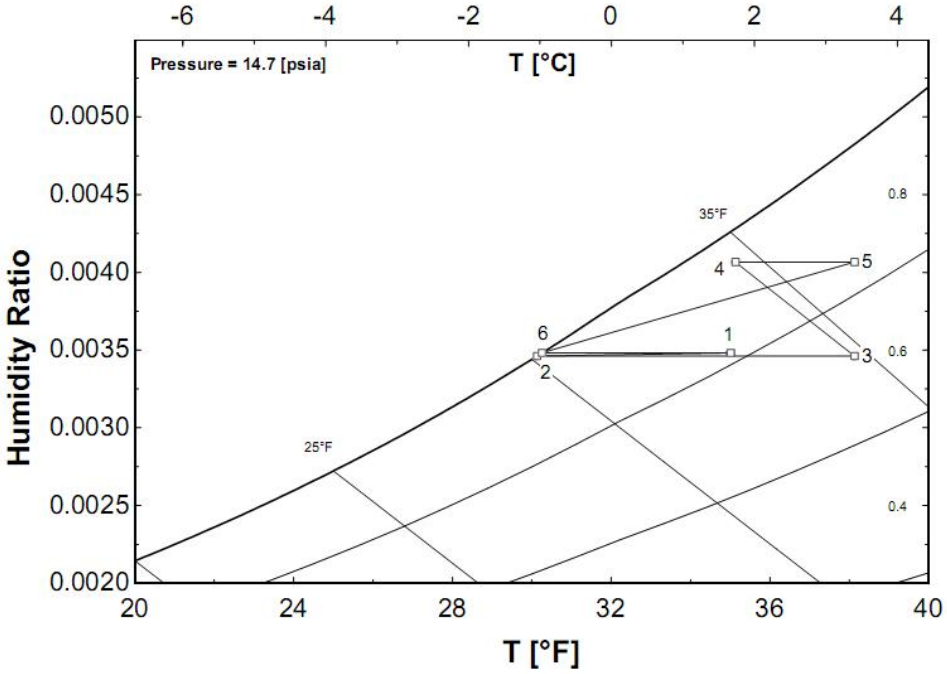

1-2	Test coil	4-5	Sensible heating in the duct
2-3	Sensible heating in duct	5-6	Cooling coil
3-4	Humidification process	6-7	Heating coil

Figure 3.3: Typical process undergone by process air for ARI H2 test Condition

Another important component of the facility is the glycol loop, which provides cold and hot fluid to the test coil. Frost is grown on the test coil by running cold fluid through the coil and defrost is achieved by running hot fluid through the coil. A cold tank and a hot tank separately maintains a supply of glycol at conditions required for frosting and defrosting respectively. Process fluid in the loop is an ethylene glycol-water solution (50% by vol.). Fluid in the cold tank is cooled by a chiller through a plate heat exchanger. Fine temperature control on the cold tank is achieved with the help of a electric resistance heater. A positive displacement pump is used to pump the fluid from the tanks to the test coil. Use of cold and hot tanks adds thermal mass to the system thereby eliminating the need for mixing to achieve the required inlet temperatures. Different experimental conditions are achieved by changing the tank set points rather than by mixing hot and cold tank fluid. Flow rate of the process fluid is measured using a Coriolis flow meter while temperature is also measured at various locations. A schematic of the fluid loop is given in Figure 3.4. Configuration of the cold and hot tanks are shown in Figure 3.5.

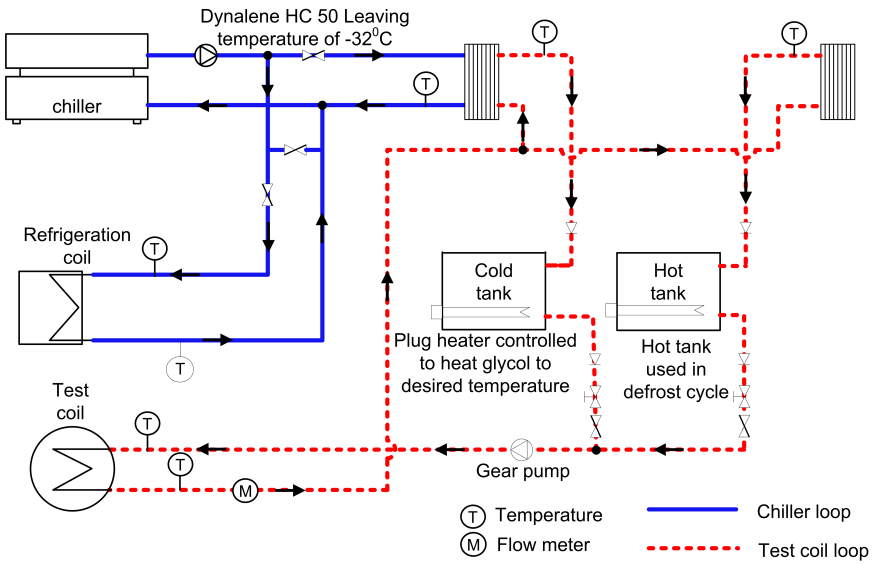

Figure 3.4: Schematic of the Fluid Loop showing both Test Coil Loop and Chiller Loop

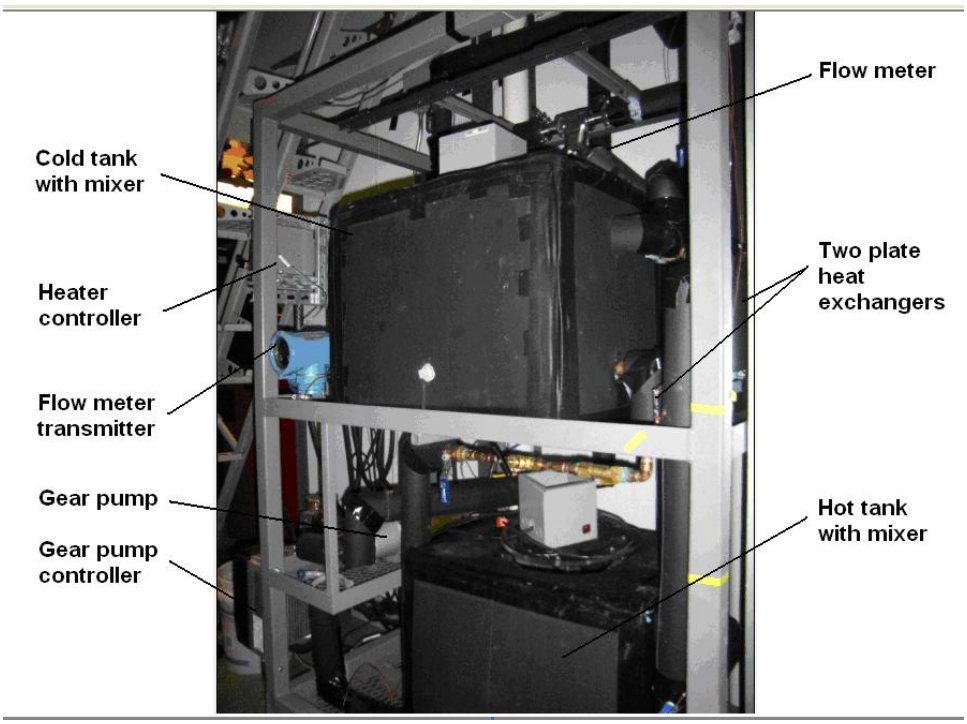

Figure 3.5: Picture of the Glycol Cart (Tanks, Heaters, Gear pump and Flow meter visible)

3.2.1 Chiller

A low temperature chiller capable of delivering 2.0 $tons$(7.03 kW) of cooling at -25^{0}F(-32^{0}C) serves the cooling requirement of the entire facility lab. Chiller supplies cold process fluid (Dynalene HC-50) to the cooling coil and also to the cold tank. Chiller is a compact water cooled packaged unit and is capable of achieving close tolerances to setpoint temperature. A process pump inside the chiller pumps the cold fluid to cooling coil and cold tank. A 25 gallon tank inside the chiller acts as a thermal reservoir so that the temperature swings occurring due to varying loads is minimized. Process fluid setpoint is achieved by the chiller by cooling fluid to a lower temperature followed by heat input from two heaters.

3.2.2 Hot and Cold Tank Heaters

Two 2.0 kW heaters are used one in each of the cold and hot ethylene glycol tanks to maintain required tank setpoints. Since the chiller outlet temperature is very low, the cold tank would go below the required setpoint if not heated. An SCR controller is attached to each heater to vary the heat input based on the temperature of the fluid in the tank. The controller is proportionally fired and the length of firing is based on a voltage input given to it by an external program. The heater is controlled via an analog signal (0-10 V) as determined by a PID controller algorithm implemented in a LabVIEW program. A T-type thermocouple is placed in a thermal well inside the tank to measure the fluid temperature in the tank.

3.2.3 Fan & Pump

A backward curved centrifugal fan is used to move the air in the tunnel. The fan is connected to a variable frequency drive so that its speed can be changed as desired. The frequency drive is connected to LabVIEW which sends an output signal based on the air flow rate. At constant fan speed, as frost grows the pressure drop across the coil increases and flow rate drops. The program is written such that a PID controller would either send out the signal (0-10 VDC) to the variable frequency drive to hold the flow rate constant or hold the fan speed constant. For experiments where the flow rate is allowed to drop as pressure increases, the program sends out a constant voltage determined by initial flow rate. Under the current configuration the fan can provide a maximum flow rate of 400 cfm.

A magnetic drive gear pump moves ethylene glycol in the test coil loop. Since the pump is a positive displacement pump, it can withstand higher head without losing much flow. This is very desirable since there is a high pressure drop associated with

pumping glycol through microchannel coils. The pump is connected to a power supply through an inverter drive. The flow rate could be varied by changing the RPM which can be externally set via a 0-10 VDC signal from the LabVIEW program. During all the tests in this study the flow through the test coil is held constant.

3.3 Measurement & Instrumentation

The facility contains instrumentation for measuring temperatures, humidity, flow rates, pressure drop and frost weight. Each instrument is calibrated as necessary and a detailed uncertainty analysis is performed. A brief description of different instrumentation will be given in this section. Further details are available in Cai (2009).

3.3.1 Temperature Measurement

Temperature measurement are made at different locations in both the air loop and the fluid loop. Air temperatures upstream and downstream of the test coil are measured using a thermocouple grid consisting of T-type thermocouples. The reading from different thermocouples in the grid are averaged by the LabVIEW program to obtain a single temperature value for that location. The upstream (inlet) thermocouple grid contains 16 thermocouples in a 4x4 configuration, while the downstream (outlet) grid contains 9 thermocouples in a 3x3 configuration. A 4-wire RTD is placed on each grid to cross check the thermocouple readings. While RTDs react slowly to temperature changes they are more accurate and can be used to check the thermocouple readings. The layout of thermocouples in the inlet and outlet grids are shown in Figure 3.6. Ethylene glycol temperatures at the inlet and

outlet of the test coil are made using pt-100 grade RTD. Other temperature measurement locations include dynalene temperatures at the inlet and outlet of the air loop cooling coil, ethylene glycol temperatures at the inlets to the hot and cold tanks and the fluid temperature inside the cold and hot tanks. Details of temperature measuring instruments are given in Table 3.1. RTDs and thermocouples were both calibrated based on the procedure described by Hern (2004). Though Hern suggested a precision thermopile to check the chiller bath temperature, this was not done for the present study. For the chiller bath uncertainty the values suggested by Hern (2004) are used since the same equipment is used.

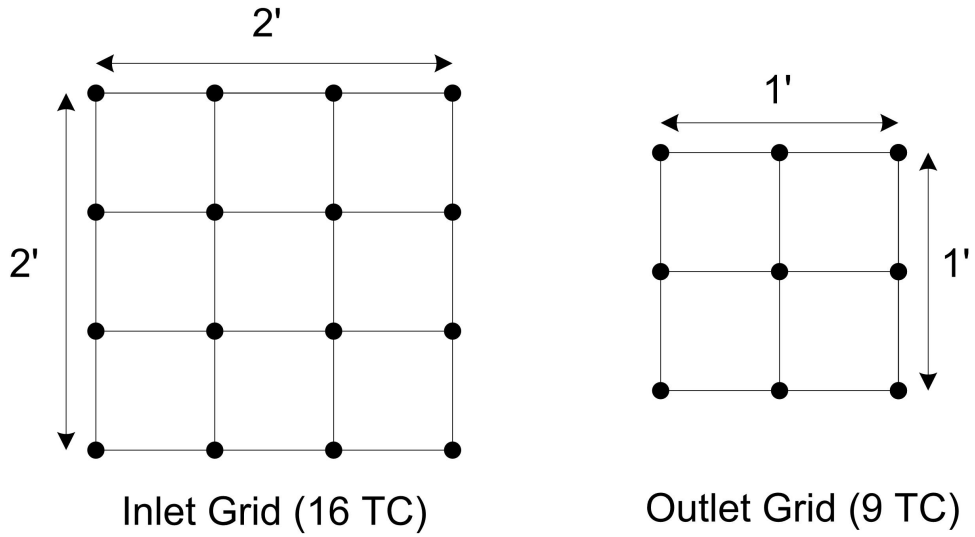

Figure 3.6: Layout of Inlet and Outlet Thermocouple Grids

3.3.2 Dewpoint Measurement

Since the frost growth phenomenon results in both sensible and latent heat transfer across the coil, it is necessary to measure the moisture content before and after the coil. As a result we need to measure at least one other moist air property other than the air temperature upstream and downstream of the coil. Due to simplicity and

lack of available space a dew point meter is used for obtaining the moisture content. A chilled mirror sensor (GE Optica series), with a pressure boss and a sampling system is used. Since the dew point measurement locations were at the lowest pressure points in the system the sensor would not see the required flow velocity without use of a sampling system. Dew point temperature along with the drybulb temperature (measured using thermocouples) is used in psychrometric calculations to give all other moist air properties like humidity ratio, enthalpy and relative humidity. The location of the dewpoint measurement can be seen in Figure 3.2

3.3.3 Pressure Measurement

Pressure drop is measured at two different locations in the air stream by a differential pressure transducers. The first pressure difference measurement is across the test coil. Another differential pressure transducer is used across a 4" nozzle to calculate the air flow rate. Calculation of the air flow rate from a measured pressure drop across an airflow nozzle followed the method specified in ASHRAE (2001). The accuracy of the pressure transducers are verified by calibrating it against a high precision micro-manometer. It was found that the transducer followed the manufacturer's accuracy values very well in the desired range of operation.

3.3.4 Glycol Flow Measurement

In order to establish a heat balance across the coil and to obtain the net heat transfer for air side heat transfer coefficient calculation, it is necessary to measure the flow rate of glycol. A Coriolis flow meter is used to measure the flow with an accuracy of $\pm 0.1\%$. Cai (2009) mentions that a flow meter with maximum flow rating significantly higher than the experimental conditions is used due to low pressure drop in that particular model. Since the published accuracy of the

instrument is based on the flow and not the full scale of the instrument, it is beneficial to use a model with a lower pressure drop.

3.3.5 Air Flow measurement

In order to measure the air side heat transfer, we need to know the flow rate of air through coil. ASHRAE (2001) has laid out the method to obtain the flow rate using measurement of pressure drop across a flow nozzle. A 4" elliptical nozzle is used, and the pressure drop is measured across the nozzle using the transducer described before. Pressure taps are located on each side of the rectangular enclosure upstream and downstream of the nozzle. Taps on each side of the nozzle are connected to give an averaged pressure reading. Equation (3.1) describes the method to obtain the air flow rate, when the pressure drop across the nozzle and the area of nozzle throat are known.

The expansion factor for the nozzle can be calculated as

$$Y = 1.0 - (0.548 + 0.71\beta^4)(1.0 - \alpha) \tag{3.1a}$$

Where α and β are parameters calculated from air properties. For the current setup where the nozzle is placed in square duct, the diameter ratio , $\beta = 0$. Alpha ratio (α) is calculated (in IP units) as

$$\alpha = 1.0 - 5.187\frac{\Delta P}{\rho R_a(T_{db} + 459.67)} \tag{3.1b}$$

With the area of nozzle throat(A_n) and expansion coefficient(C) known, the flow rate (Q_a) in IP units is then calculated as

$$Q_a = 1097Y\sqrt{\frac{\Delta P}{\rho}}CA_n \tag{3.1c}$$

Where $\Delta P =$ Pressure drop across nozzle [in H_2O]

$\rho =$ Air density [lbm/ft^3]

$T_{db} =$ Air stream temperature [F]

$R =$ Gas constant [ft-lbf/lb-^{0}R]

$A_n =$ Nozzle throat area [ft^2]

$Q_a =$ Volumetric flow rate [ft^3/min]

3.3.6 Frost Thickness Measurement

Frost thickness measurements have been reported by mechanical measurement techniques (Östin, 1992; Şahin, 1994), optical method (Thomas et al., 1999) and also using image processing methods (Xia et al., 2006). Mechanical measurement techniques are not accurate and also will disturb the experimental conditions including the frost growth. Optical measurements while non-invasive are hard to calibrate and will not produce good results due to the high reflectivity and roughness of the frost surface (Na and Webb, 2004*b*). Thus it was decided to obtain the thickness based on images. In order to capture the images a videoscope (VP300) from Everest VIT with a 4.9 ft(1.4 m) probe is used. The images may have edge distortion which will make the portions of the image near the perimeter to be curved. Thus care was taken to locate the camera such that the measurement location was at the center of the image. The videoscope continuously feeds the images to a local computer connected via an S-Video interface and an analog to

digital converter. Still images are obtained by capturing frames from the live feed.

A 3-axis traverse system described by Carrol and Peterson (2009) is used to move the camera to different locations of the heat exchanger. The movement of the camera is also controlled by the LabVIEW program. The program reads the predefined location coordinates and moves the camera. At each location the motor is halted for one minute, after which the program sends a signal to capture frames from the live feed. iViewPC software from GE Inspection technologies, is used for analyzing images obtained from videoscope. Multiple measurements are made in the measurement vicinity to make sure that the obtained value is representative value. From multiple measurement trials, the uncertainty in the thickness measurement,was estimated to be ± 0.03 mm for correctly focused images.

3.3.7 Frost Weight measurement

A precision digital weigh scale from Arlyn scales (model # Saw-L) is used to measure the weight of frost during the frosting period. The full scale of the instrument is 50 lbs (23 kg) with a manufacturer published accuracy of ± 0.2g. The test coil is suspended from the scale using metal strings and extended arm. Extended arm was used to eliminate any rotational effects that could occur during the fan operation. Duct is sealed upstream and downstream of the test coil using plastic wrap in a way that the vertical motion is not affected. To eliminate any stiffness effects of inlet and outlet pipes, the glycol tubes are long and coiled. In order to measure the weight during frosting period, it was necessary to stop the fan and let the scale stabilize. Tests were conducted by turning the fan off after equal intervals during frosting period and without turning the fan off. Behavior of the coil from frost growth perspective was similar and thus it was justified to stop the fan. After a number of trials it was found that stopping fan for one minute after every 10

minutes is sufficient.

3.4 Data Acquisition and Control

A Fluke 2680 data logging system was used to read the data from different sensors. The system can contain up to 6 modules with each module able to read measurements from 20 channels (10 for 4-wire RTDs). Two control boards (PCI-DAC 6703 for analog and PCI-DAS 6025 for digital) from Measurement Computing provides the control signals to all devices. Heaters, fan, gear pump and modulating valves are controlled by analog signals ranging from 0-10VDC, while ON/OFF valves and humidifiers are controlled by digital signals.

A LabVIEW program was developed to streamline various actions such as data acquisition, real time calculations, plotting and control. Channels are scanned every five seconds and the readings are transmitted to a central computer running LabVIEW via ethernet. Real time processing of data is performed to maintain the experimental setpoints and establish steady state conditions before starting each test. The program plots process variables and also allows manual override of device operation. A screenshot of the program window that lets the user to set test conditions and device operations is shown in Figure 3.7. Figure 3.8 shows the plot window where different process variables can be monitored.

3.5 Calculations & Uncertainty Analysis

In order to derive meaningful results from the experiments, primary measurements need to be processed and other quantities need to be derived from those. The uncertainty associated with any primary measurements will propagate through the calculations and introduce uncertainty in derived quantities. An uncertainty

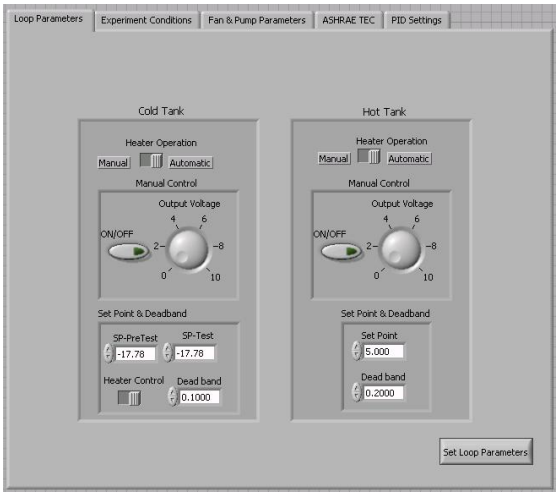

(a) LabVIEW User Interface for Heater Settings

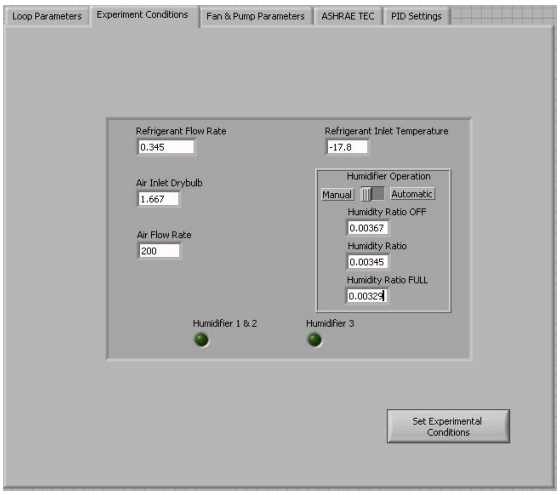

(b) LabVIEW User Interface for Specifying Test Conditions

Figure 3.7: Screenshot of LabVIEW Windows for User Interaction

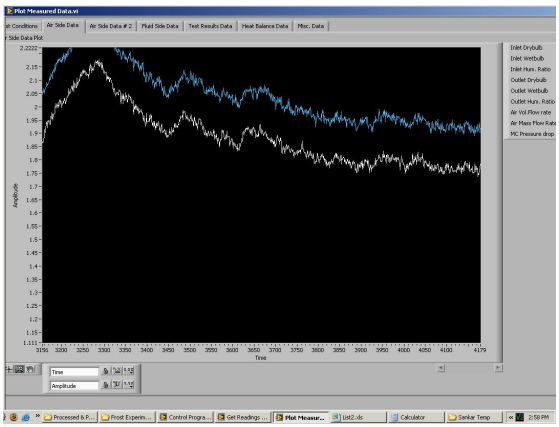

(a) Plot Window showing Air DB

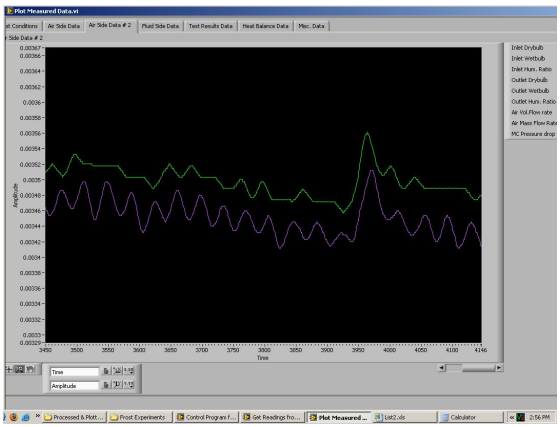

(b) Plot Window showing Air Humidity Ratio

Figure 3.8: Screenshot of LabVIEW Plot Windows for Monitoring

analysis will help us gain confidence in the results in addition to allowing us to derive meaningful conclusions. This section presents the methods used to calculate various quantities of interest and also the propagation of error for each variable. Kline and McClintock (1953) present a method to calculate the uncertainty associated with measurement and also with derived variables. If a variable is measured and there are n independent sources of error, then the final uncertainty in measurement is defined as

$$e_v = \sqrt{e_1^2 + e_2^2 + \cdots + e_n^2} \tag{3.2}$$

As mentioned before, uncertainty in measurement of a variable will propagate when used in calculating any other derived quantities. If a quantity is dependent on n measured variables, each of which is associated with an independent error value, the final uncertainty on the result can be calculated as

$$e_R = \sqrt{\left(\frac{\partial R}{\partial v_1}\right)^2 e_{v1}^2 + \left(\frac{\partial R}{\partial v_2}\right)^2 e_{v2}^2 + \cdots + \left(\frac{\partial R}{\partial v_n}\right)^2 e_{vn}^2} \tag{3.3}$$

This following sections applies the uncertainty theory described above to calculate the error associated with each quantities.

3.5.1 Temperature Differences

Air side temperatures are measured using T-type thermocouples and glycol side temperatures are measured using RTDs. Since temperature difference is a derived quantity from two separate temperature measurements, the final error associated with the temperature difference as:

$$e_{\Delta T} = \sqrt{e_{T,i}^2 + e_{T,o}^2} \tag{3.4}$$

where $e_{\Delta T}$ = uncertainty in temperature difference

$e_{T,i}$ = uncertainty in inlet temperature

$e_{T,o}$ = uncertainty in outlet temperature

After calibration the uncertainties associated with T-type thermocouples and RTDs are calculated as 0.15^0 C and 0.1^0 C respectively. Incorporating these uncertainty values into the calculation we get the final error in temperature difference as

Air Side: $e_{\Delta T} = \pm 0.21^0 C$

Glycol Side: $e_{\Delta T} = \pm 0.14^0 C$

3.5.2 Air Flow Rate

As mandated in ASHRAE (2001), air flow rate is calculated by using an elliptical nozzle and a differential pressure nozzle. Sources of error include the uncertainty associated with the pressure transducer, error in the density calculation of the air and the error associated with area of the nozzle. Though the uncertainty in pressure measurement is highest, the other uncertainty sources also need to be considered. The equations required to calculate the air flow rate were given in equations (3.1). Combining all the sources of error (in fractional representation) the final uncertainty in the air flow rate calculation can be written as prescribed in ASHRAE (1999).

$$e_{\dot{V}_a} = \sqrt{e_c^2 + e_A^2 + e_{dp}^2 + e_{sp}^2 + e_\rho^2 + e_N^2} \tag{3.5}$$

where $e_{\dot{V}_a}$ = uncertainty in air flow measurement

e_c = uncertainty in discharge coefficient

e_A = uncertainty in nozzle area

e_{dp} = uncertainty in differential pressure measurement

e_{sp} = uncertainty in static pressure measurement

e_ρ = uncertainty in density

e_N = uncertainty in fan speed

ASHRAE (1999) requires the nozzle used for air flow rate measurements to have uncertainties associated with discharge coefficient and area not to exceed ±1.2% and ±0.5% respectively. The uncertainties associated with fan speed is determined to be less than ±1%. The pressure transducer has a published uncertainty of ±1% and the error in static pressure measurement is dependent on the air flow. Combining all the uncertainties we get the final uncertainty on air flow rate to be approximately ±2% for the whole range of operation.

3.5.3 Air Side Heat Transfer Rates

Coils operating under frosting conditions have both sensible and latent heat transfer rates. In such a coil, where both heat and mass transfer takes place, the total heat transfer taking place on the air side is calculated as

$$\dot{Q}_a = \dot{Q}_s + \dot{Q}_l \tag{3.6}$$

Error in air side total heat transfer is calculated as

$$e_{Q_a} = \sqrt{(e_{Q_s})^2 + (e_{Q_l})^2} \tag{3.7}$$

Sensible heat transfer across the coil is calculated based on the temperature difference and is expressed as

$$Q_s = \rho_a \dot{V}_a c_{p,a} \Delta T_a \tag{3.8}$$

Latent heat transfer across the coil is calculated based on the enthalpy difference and is expressed as

$$Q_l = \rho_a \dot{V}_a c_{p,a} \Delta h_a \tag{3.9}$$

Neglecting the uncertainty in air properties, the major sources of uncertainty are the air flow rate and the temperature difference. Following the uncertainty propagation formula and expressing in fractional form, we get the uncertainty in air sensible heat transfer as

$$e'_{Q_s} = \sqrt{\left(e'_{\dot{V}_a}\right)^2 + \left(\frac{e_{\Delta T_a}}{\Delta T_a}\right)^2} \tag{3.10}$$

In the above equation all quantities in the right side except the temperature difference is constant and calculated in preceding sections.

Following a similar method for latent heat transfer we get the uncertainty in latent heat transfer in fractional form as

$$e'_{Q_l} = \sqrt{\left(e'_{\dot{V}_a}\right)^2 + \left(e'_{\Delta h_a}\right)^2} \tag{3.11}$$

The uncertainty in enthalpy difference, Δh_a, is not as straight forward as that for temperature difference. This is because air side enthalpy is calculated using curve fit correlations using the dew point temperature as input. While the correlations are accurate for all practical purposes (ASHRAE, 2005), there are errors associated

with dew point measurement and this would propagate into enthalpy calculations. Uncertainties for sensible and latent heat transfer are calculated using EES (Klein and Alvarado, n.d.) for every measurement point.

3.5.4 Fluid Side Heat Transfer Rates

Since the glycol is in single phase, the total heat transfer can be calculated if the flow rate, inlet and outlet temperatures of glycol are measured. From the glycol side measurements we can calculate the total heat transfer as

$$\dot{Q}_r = \dot{m}_r C_{p,r}(T_{r,i} - T_{r,o}) \tag{3.12}$$

Ignoring the uncertainty in glycol property, the uncertainty in fluid side heat transfer is obtained along the same lines as air side sensible heat transfer.

$$e'_{Q_r} = \sqrt{\left(e'_{\dot{m}_r}\right)^2 + \left(\frac{e_{\Delta T_r}}{\Delta T_r}\right)^2} \tag{3.13}$$

3.5.5 Experiment Heat Balance

Due to the transient nature of the experiments it is very difficult to establish a heat balance with just air side and fluid side heat transfer rates. However, verification of the experimental facility requires a heat balance to be established. Such a verification confirms the accuracy of all the instrumentation in the facility. Such a heat balance is performed with a dry test where the air is not cooled below its dew point. Under dry conditions the heat balance is established as

$$HB = \frac{Q_a - Q_r}{(Q_a + Q_r)/2} \times 100(\%) \tag{3.14}$$

3.6 Experimental Procedure & Data Reduction

3.6.1 Procedure

Control of air flow is different for fin and tube and microchannel coil. For fin and tube coil, the flow rate was maintained constant through out the test. This was done by varying the frequency of the VFD drive. The motivation behind fixing the air flow rate through out the test was to develop data sets where significant air flow redistribution occurs and thus can be used to validate the model being presented in Chapter 4. For microchannel coil, the flow rate was allowed to drop by keeping the fan speed constant. In the case of microchannel coil, the initial pressure drop was high and thus the operating speed of the fan at the start is almost 60% of maximum. If the air flow were to be kept constant for microchannel coil, the time of test would have been very small and no meaningful result could be obtained. Thus for microchannel coils, it was decided that the fan speed be kept constant.

An omni- directional air speed probe is also attached to the traverse axis to measure the local air speed at different points. Measurements are acquired every 4 seconds by a FLUKE data acquisition system and transmitted to a central computer running LabVIEW 8.0. The program sends out analog (heaters, fan and pump) and digital (humidifier) control signals along with commands for camera movement and image capture. Measured parameters along with the instruments used and related uncertainties are shown in Table 3.1. The table also shows various test conditions and tolerances within which the parameters are controlled during tests.

To eliminate the effect of lift and drag on the coil, the weight measurements are taken by stopping the fan for a maximum of one minute after every 10 minutes. Results from this method are compared to those obtained from continuous fan operation and found to match within experimental uncertainty. All measured data

Table 3.1: Measured parameters, instrument uncertainties and test conditions

Measured Parameter	Instrument	Calibration method	Uncertainty	Tolerance
Air temp (DB) [C]	Thermo couple	In-situ[1]	0.15	±0.56
Glycol temp [C]	RTD	In-situ	0.1	±0.25
Dew point [C]	Chilled mirror	Manufacturer	±0.1	N/A
Air flow rate [m^3/s]	ASHRAE nozzle	In-situ	±2.3%	0.0014
Glycol flow rate [kg/s]	Coriolis flow meter	Manufacturer	±0.01%	0.0005
Pressure drop [Pa]	Differential pressure transducer	In-situ[2]	±0.25%	N/A
Frost weight [g]	Precision scale	Manufacturer & In-situ	±0.2	N/A
Frost thickness [mm]	Videoscope images	In-situ	±0.01	N/A

are verified using a secondary method when ever possible. For example, the weight reading by the scale is verified by comparing the scale reading at the end of cycle against the weight of melted water at the end of the cycle. Weight at intermediate points are checked against the mass of frost obtained from integrating instantaneous value of humidity difference. The final frost weight matched the weight obtained from both methods within 10%. The instantaneous values has an error of 20%. The high error in intermediate values is because of the lag introduced in the sampling lines used for humidity measurements.

Before the test started the air inside the tunnel is cooled down to test conditions and allowed to reach steady state. Once steady state is reached, glycol from cold tank is allowed through the coil and frosting period starts. Air flow rate through the coil is maintained constant throughout the test by varying the frequency of the VFD drive. Test is considered finished when the VFD drive reached maximum capacity and is not able to provide the required cfm through the coil.

3.6.2 Data Reduction

Air side and glycol heat transfer rates are calculated from measured temperatures and flow rates as shown in Eqs. (3.15) and (3.16).

$$\dot{Q}_{a,t} = \dot{Q}_s + \dot{Q}_l \tag{3.15}$$

$$\dot{Q}_r = \dot{m}_r C_{p,r}(T_{r,o} - T_{r,i}) \tag{3.16}$$

Total air side heat transfer rate can be split into sensible and latent parts which are obtained as follows

$$\dot{Q}_s = \dot{m}_a C_{p,a}(T_{a,i} - T_{a,o}) \quad \text{and} \quad \dot{Q}_l = \dot{m}_f h_{sg} \tag{3.17}$$

An energy balance can be established from measured heat transfer using Eq (3.18).

$$\Delta Q = \frac{|Q_r - Q_{a,t}|}{(Q_r + Q_{a,t})/2} \tag{3.18}$$

Uncertainty in the refrigerant side heat transfer calculations is calculated as 7%, while the uncertainty in air side sensible heat transfer varied between 4.8% during the start of test to 10% towards the end of the test. Due to transient nature during frosting an energy balance is established during a dry test in order to validate temperature and flow rate measurements. During the dry test an energy balance of $\pm 5\%$ is established. Once the temperature and flow rate measurements are validated, the air side latent heat transfer rate is obtained as shown in Eq (3.19).

$$\dot{Q}_l = \dot{m}_r C_{p,r}(T_{r,o} - T_{r,i}) - \dot{m}_a C_{p,a}(T_{a,i} - T_{a,o}) \tag{3.19}$$

Performance of heat exchanger is characterized by overall conductance (UA) and overall heat transfer coefficient (U) for dry coils. For wet coils two more parameters are defined viz., Overall energy conductance (HA) and overall energy transfer coefficient (H). Frosted coils have been analyzed previously using $HA - LMED$ method (Sanders, 1974; Kondepudi and O'Neal, 1989) and $UA - LMTD$ method (Stoecker, 1960; Barrow, 1985). Xia and Jacobi (2005) showed that $UA - LMTD$ approach gave better results than the $HA - LMED$ method when correctly used. Following the approach proposed by Xia and Jacobi (2005), air side sensible heat transfer rate is used to obtain the overall conductance of the heat exchanger as shown in Eq (3.20). Correction factor (F) for log mean temperature difference is

calculated for all data points and used in Eq (3.20).

$$\dot{Q}_s = UA\Delta T_{lm}F$$
$$UA = \frac{Q_s}{\Delta T_{lm}F} \tag{3.20}$$

Due to the non-uniformity of frost growth on the heat exchanger, the area that is used in heat transfer calculations must correctly account for such difference in frost thickness. Considering n segments across the length of the heat exchanger, the overall heat transfer coefficient is then obtained as shown in Eq (3.21).

$$U = \frac{UA}{\sum_{i=1}^{n} A_i} \tag{3.21}$$

3.7 Results and Discussions: Fin and Tube

The test coil under consideration is a one row fin and tube coil with louvered fins. The geometry and specifications of the test coil is provided in Table 3.2. Three different sets of experiments are conducted to study the effect of refrigerant temperature, air relative humidity and air flow rate. A base case for air side conditions is identified as the H2 conditions ARI (2008), which specifies the entering air conditions to the test coil as 1.67^0C/0.56^0C (DB/WB). Table 3.3 shows air and fluid conditions during different tests. In actual heat pump operating conditions the air flow across the coil will drop as frost grows due to increased pressure. Barrow (1985) argued that the drop in capacity in frosted coils is due to drop in air flow and the frost itself had negligible effect, which was contrary to accepted theory (Stoecker, 1957; Sanders, 1974; Tantakitti and Howell, 1986). The results of the fin and tube experiments discussed in this section does not support Barrow's assertion. Furthermore it is seen that for non uniformly frosted coils the redistribution of

Table 3.2: Geometry & Specifications for Fin-Tube Test Coil

Parameter	Value
No. of Rows	1
No. of Tubes	12
Coil Length [mm]	305
Coil Height [mm]	305
Fin Depth [mm]	22.1
Fin Density [fins/m]	630
Fin Thickness [mm]	0.1
Tube ID/ OD [mm]	10.06/ 10.67
Tube/ Fin Material	Copper/ Aluminum

Table 3.3: Test Conditions for Fin-Tube Coil

Parameter	T_{ref} [^{0}C]	$\dot{V}_{air}$ [m^3/s]	RH [%]
Refrigerant Temperature	-17.8 -22.8 -25.6	0.09	82
Air flow rate	-17.8	0.07 0.09 0.13	82
Air relative humidity	-17.8	0.09	72 82 92

airflow is an important performance parameter. In order to isolate the effect of frost growth alone, the flow across the coil is held constant throughout the test. Test is considered finished when the fan is not able to provide the desired flow rate.

3.7.1 Non-uniformity in frost growth

While the outdoor coil acts as both condenser (cooling mode) and evaporator (heating mode), its design is optimized for performance in cooling mode. Factors such as non-optimal circuiting, superheat in the evaporator coil (instead of suction line), non-optimal air flow can occur on the face of outdoor coils which will lead to

non-uniform frosting. Relatively small variations in fluid temperature will lead to large variations in surface temperature which will also cause non-uniform frost growth. For the test coil, a 1.5^0C temperature difference from inlet to outlet resulted in the non-uniform frost pattern shown in Figure 3.9. The figure shows the image of the coil obtained by videoscope at four different locations at four different times for an inlet refrigerant temperature of -17.8^{0}C. It can be seen that the rate of growth of frost is significantly different at each location. Near the refrigerant inlet (x/L = 0.125) the frost grows at a faster rate compared to the downstream locations. At time t = 20 mins, location 1 (x/L = 0.125) has a thick layer of frost, while frost has just started to grow at location 2 (x/L = 0.375). The last two segments still does not have any visible frost. At time t = 40 mins, images show how the frost properties are different. Frost that grows in first and second locations are more fluffy (low density), while the frost in the last two segments is more ice-like (high density). These images are consistent with the frost density theories that suggest density of frost is lower at lower temperatures.

Frost thickness is measured by processing the images obtained from the videoscope using image processing software. Figure 3.10 shows the frost thickness at various locations for different entering refrigerant temperatures. Frost thickness results are presented in dimensionless form based on half fin spacing. At any given refrigerant inlet temperature, the frost grows faster at upstream locations. For the low temperature cases ($T_{r,i} = -22.8^0C$ and $T_{r,i} = -25.6^0C$), frost can be seen at the leading edge almost at the start of the test, while for high temperature case ($T_{r,i} = -17.8^0C$), it takes almost 10 minutes for the frost to be visible at leading edge. This suggests that frost starts to grow at the tube surfaces and move towards the leading edge. The rate of frost growth in the first segment increases almost linearly from the time of frost initiation. For the downstream segments, on the other hand, the rate of frost growth is continuously changing. The continuous

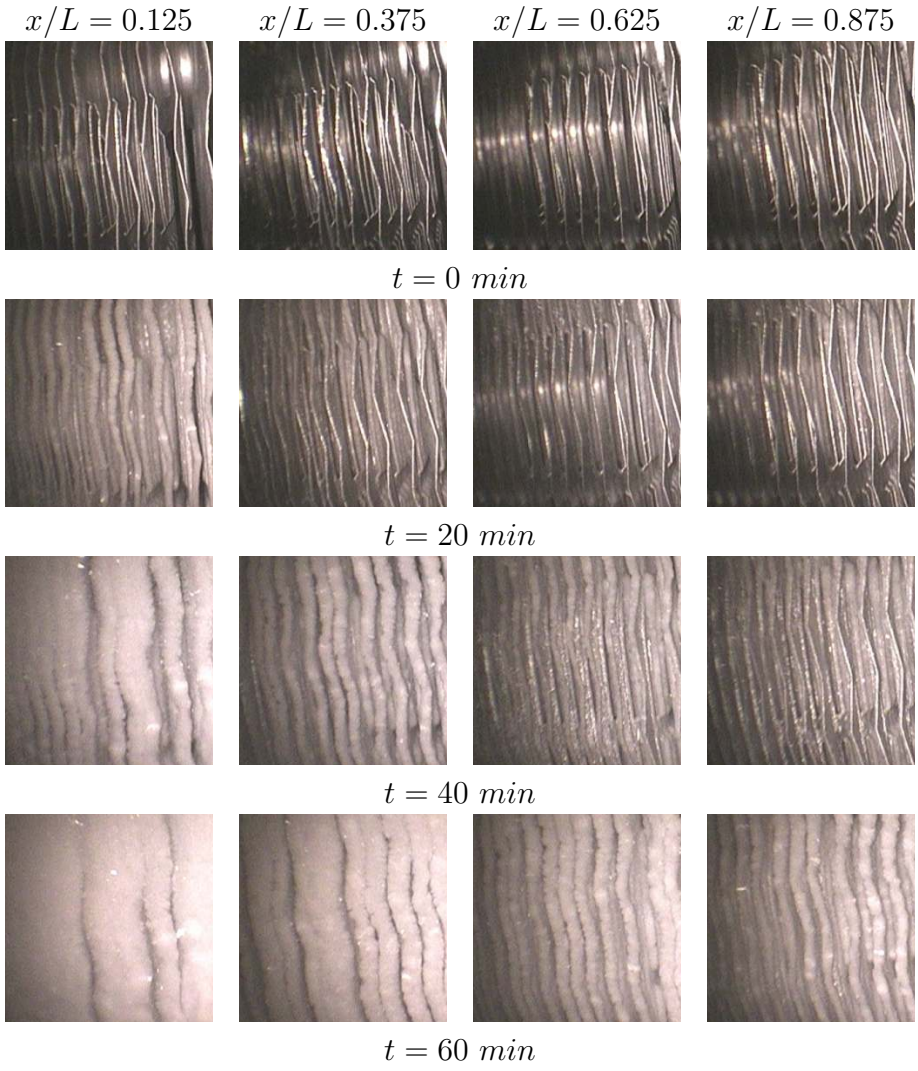

Figure 3.9: Frost images at different locations along the length of the coil ($T_{r,i}$=-17.8^{0}C, RH = 82%, $\dot{V}_{air}$=0.09 m^3/s)

variation in frost growth rate for downstream segments can be attributed to the air redistribution phenomenon that occurs due to non-uniform frost thickness. Since the segments are parallel flow paths, to satisfy equal pressure drop condition, the segments with thicker frost will have less air flow thereby reducing the segment heat transfer. This causes the temperature of fluid entering downstream segments to drop as time progresses. This reduction in refrigerant temperature as time progresses causes the frost growth rate to increase. It can also be seen from the figures that as the entering glycol temperature is reduced the frost growth curve for downstream segments move towards the first segment.

Since the total air flow rate is kept constant through out the test, as the flow drops in the initial segments the later segments will see an increase in flow of air. This causes the air velocity in initial segments to drop compared to initial velocity while in the later segments air velocity will increase compared to its initial value. Figure 3.11 shows the change in velocity at each segment during the test ($T_{r,i} = -17.8^0C$, $\dot{V}_a = 0.09\ m^3/s$, $RH = 82\%$). It can be seen from the figure that there is a drop in velocity at the first segment. Location 3 and Location 4 sees an increase in air velocity. Figure does not show the measured points beyond 40 minutes. As frost thickness became considerable in the first segment around t = 40 mins there was high degree of recirculation in air flow resulting in the uncertainty in air flow measurements to increase significantly.

3.7.2 Frost thickness

Experimental results on the effect of temperature and RH on frost growth agree with the observations made by previous researchers (Jones and Parker, 1974; Mao et al., 1992). There is no consensus in the literature on the effect of air flow on frost growth. Our experiments suggest that air flow does not have a significant effect on

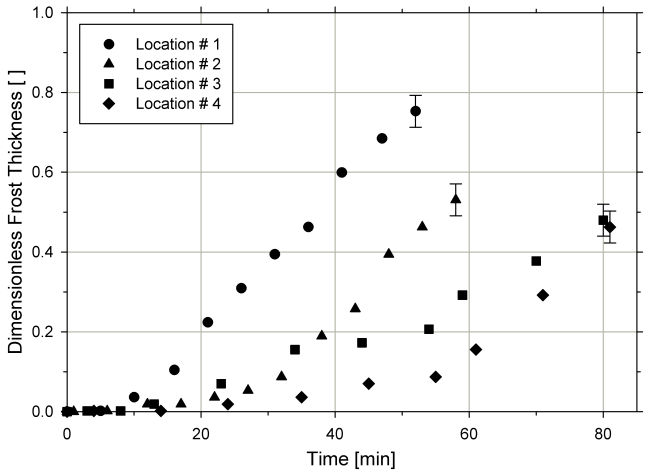

(a) Glycol Temperature = -17.8^{0}C

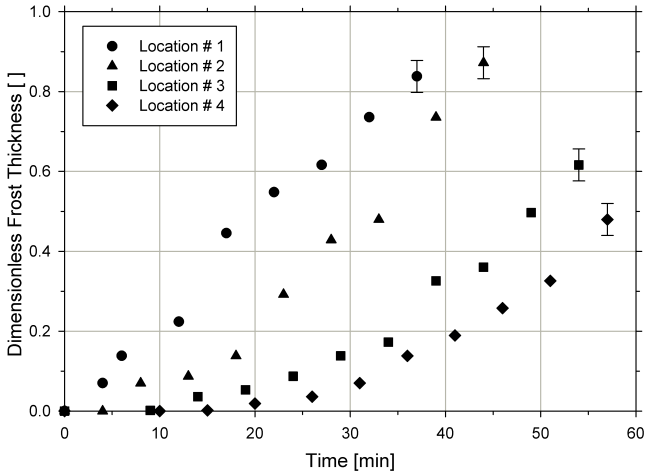

(b) Glycol Temperature = -22.8^{0}C

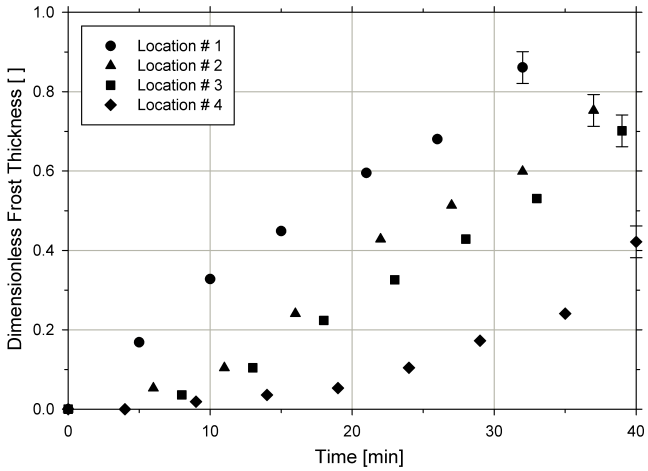

(c) Glycol Temperature = -25.6^{0}C

Figure 3.10: Variation in frost thickness at different locations for different inlet glycol temperatures

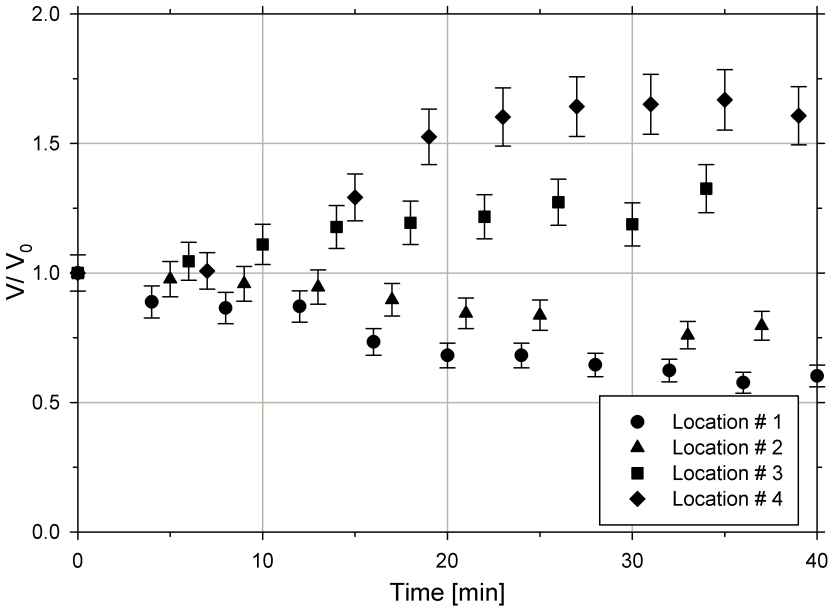

Figure 3.11: Local velocity variation at each segment

frost growth. Figure 3.12 shows the variation of frost thickness at first location (x/L = 0.125) for different test conditions. Lower glycol temperatures result in thicker frost growth as shown in Figure 3.12a. The lag in the frost growth at leading edge is clearly seen for the high temperature case. Figure 3.12b shows the frost thickness at first location for varying air relative humidity. It can be seen that higher RH causes faster frost growth. The lag in the development of frost growth at leading edge increases as RH is reduced. Effect of airflow on frost growth is shown in Figure 3.12c. It can be seen that air flow does not have a significant impact on the frost growth. Low air flow causes frost to accumulate at slightly faster rate. This can be explained from the fact that as air flow drops the air side heat transfer coefficient reduces resulting in lower surface temperature and causing frost to grow at a faster rate.

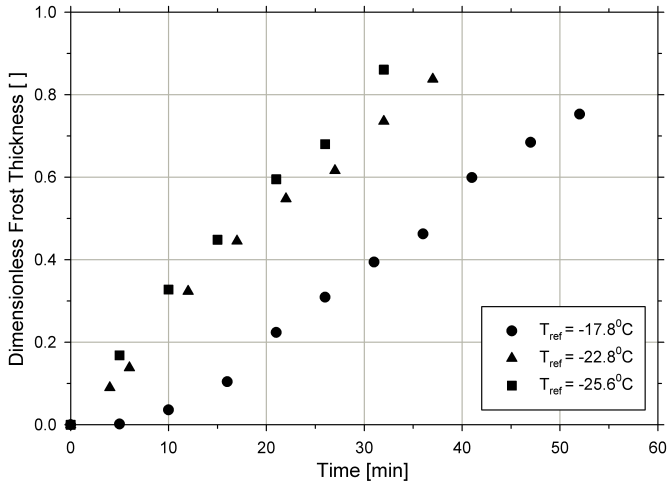

(a) Effect of temperature

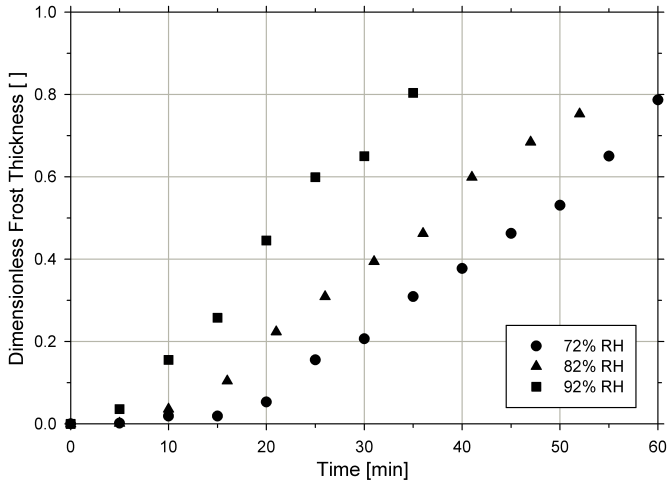

(b) Effect of RH

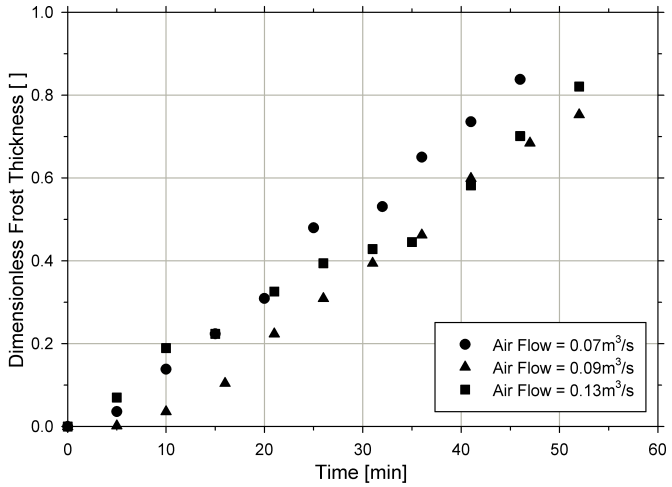

(c) Effect of air flow

Figure 3.12: Variation in frost thickness at location 1 for different test conditions

3.7.3 Frost weight

While the thickness results agree with previous research, a different phenomenon can be seen regarding the frost weight. Weight of accumulated frost on heat exchanger for different test conditions is shown in Figure 3.13. Figure 3.13a shows the accumulated frost weight for different entering glycol temperatures. It can be seen that the frost accumulation rate is higher for low temperature case. The total accumulated weight over the test period for low temperature case is less than that for high temperature case. Low surface temperature causes the frost that is deposited to be less dense (fluffy) and thus for a given thickness will have less mass. For high temperature frost accumulation the density is high (ice-like). This behavior is observed by many investigators studying the properties of frost (Biguria and Wenzel, 1970; Hayashi et al., 1977a). This density difference in accumulated frost explains the crossover of frost weight curve for low temperature case ($T_{r,i} = -25.6^0C$). It can be also seen that weight curve for the medium temperature case ($T_{r,i} = -22.8^0C$) is flattening out towards the end of the test and is likely to cross over the high temperature curve.

Effect of air relative humidity on weight of accumulated frost is shown in Figure 3.13b. As expected, high relative humidity causes the frost to grow faster. At 72% RH the frost growth is minimal and almost linear throughout the frosting period. The crossover that was seen in the weight curves for different temperatures is also seen for RH cases. The final weight of 92% RH case is lower than the weight for 82% RH case. As the air relative humidity increases, the latent heat capacity of the coil increases and thus the sensible heat ratio of the coil will drop. Since the sensible - latent split in the capacity takes place at the air side in the thermal network, a reduction in sensible heat transfer will result in the temperature of fin/tube surface to be near the refrigerant temperature. As a result the tube/fin

temperatures for 92% RH case will be lower than that of 82% case. The difference in frost growth pattern and weight accumulation is a consequence of this difference in surface temperature.

3.7.4 Heat exchanger performance

The overall conductance (UA) of the coil will drop as frost grows due to added resistance of the frost layer. Variation of UA for the heat exchanger under different operating conditions is shown in Figure 3.14. Figure 3.14a shows the variation of UA for three different entering glycol temperatures. For all the three cases the UA value increases initially and then starts to fall. For the case, $T_{r,i} = -17.8^0C$, the increase in UA is not significant until 18 minutes. The heat transfer coefficient is highest at the leading edge of the heat exchanger due to developing boundary layer. When the frost starts to grow at the leading edge, which is around 18 mins for high temperature case, the rough frost layer increases the heat transfer coefficient further, thereby increasing the overall conductance of the coil. At times before 18 mins, the frost is accumulated mostly on tubes, which does not affect air flow significantly (since the frost thickness is small compared to tube diameter) and thus not changing the heat transfer coefficient significantly. At low temperatures similar trends are observed for for overall conductance of the coil. As the temperature is lowered the time when the overall conductance starts to drop is also shorter. This is because for lower temperatures the frost starts to accumulate at leading edge earlier than for high temperature case.

The overall conductance at the end of the test is approximately 35% below the initial value. The drop in UA shown in this study is due to frost layer alone and is a combined effect of two different mechanisms involved. First the frost layer adds an extra resistance to heat transfer between air and tube/fin surface. Secondly, as frost

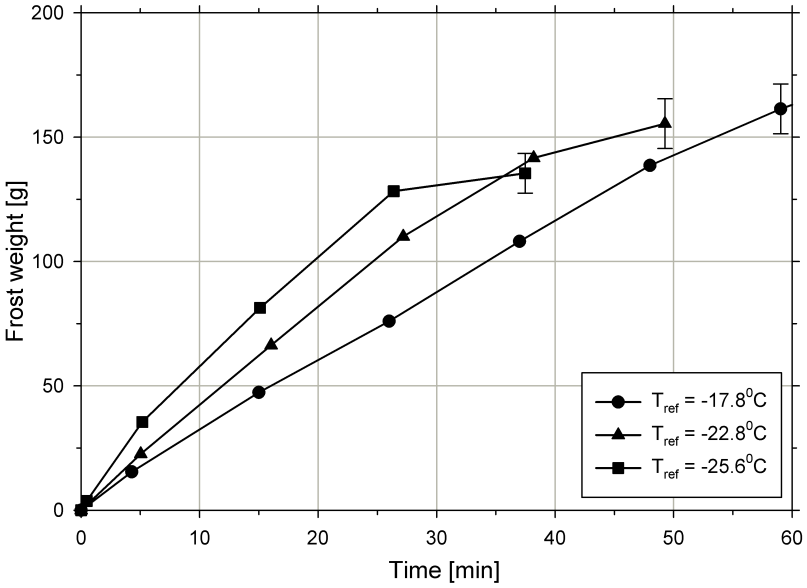

(a) Effect of Temperature

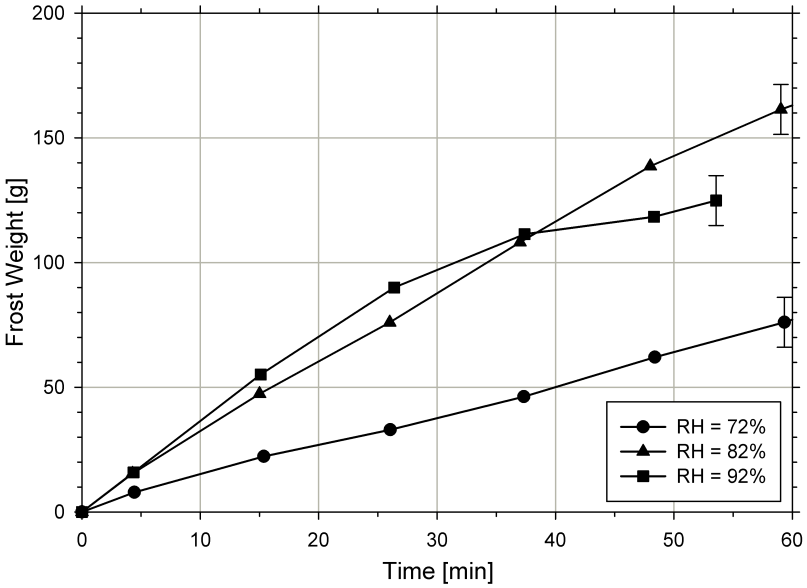

(b) Effect of RH

Figure 3.13: Accumulated frost weight for different test conditions

grows and covers some of the upstream segments the total area available for heat transfer is reduced considerably. It is important to note that the drop in capacity is not due to drop in total airflow, since the tests are carried out by maintaining a constant airflow across the test coil.

Figure 3.14b shows the change in UA for different air relative humidity. Trends in the change in UA is similar to those explained before for different temperatures. It can be seen that for low air relative humidity, the UA does not drop significantly. The initial UA value for high relative humidity case is lower because of the low sensible heat ratio of the coil discussed before.

While specifying a value or correlation for overall heat transfer coefficient or air side convective coefficient it is required to specify the area used for its calculation. To study the performance of heat exchangers under frosting conditions, where the heat transfer area changes with time, it is desirable to present the overall heat transfer coefficient instead of overall conductance of the coil. Previously researchers always used the frost thickness at one measured location to determine the heat transfer area. However, depending on the location of measured location this method will introduce error in the calculation of heat transfer area. Measuring frost thickness at colder locations will under estimate the heat transfer area while measurement taken at hotter parts of the coil will underestimate the area. In this study the heat transfer area is calculated as described in (3.21). Assuming a uniformly frosted coil when the coil in fact is frosting non-uniformly can lead to a significant error in the calculated overall heat transfer coefficient of the coil (U) of the coil as shown in Figure 3.15. The plot shows the error between the value of overall heat transfer coefficient calculated based on (3.21) and by assuming a uniform frost thickness across the coil (equal to the thickness at first measurement location). The figure shows the error for three different glycol temperatures. It can be seen that the error for all cases is

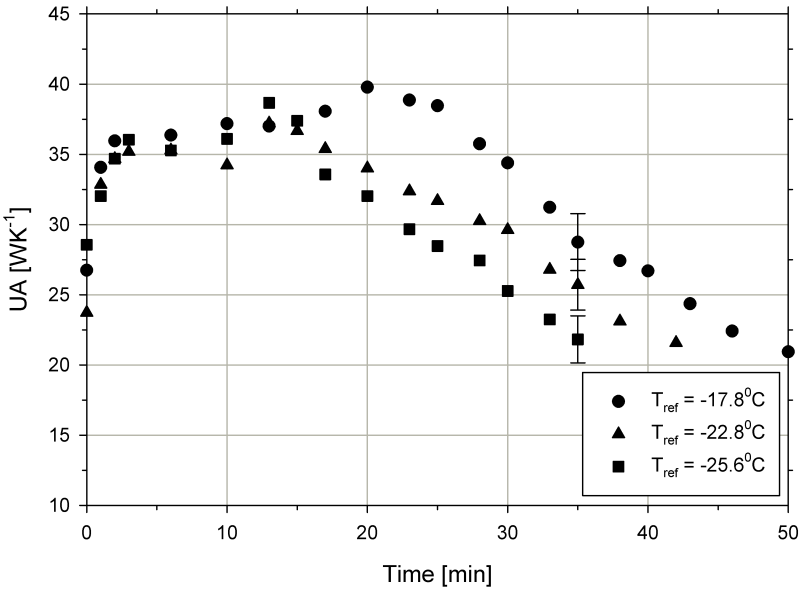

(a) Effect of Temperature

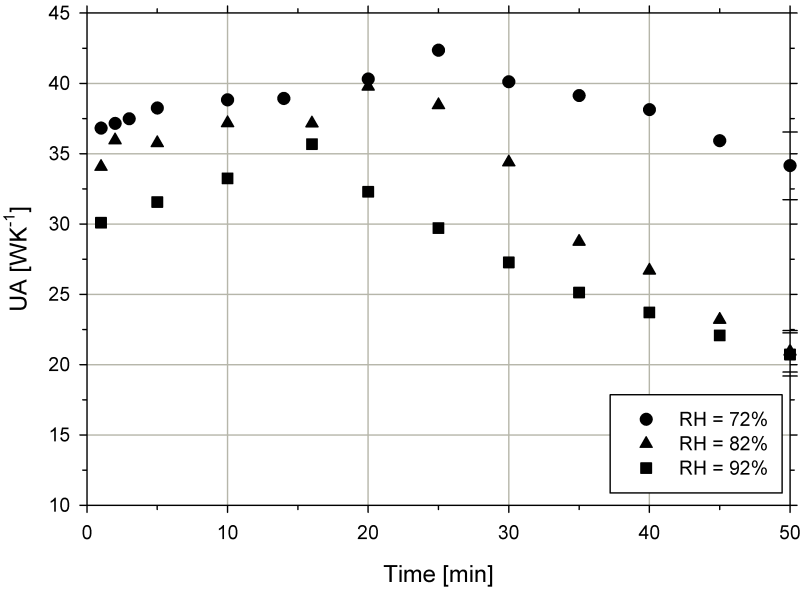

(b) Effect of RH

Figure 3.14: Variation in UA for different test conditions

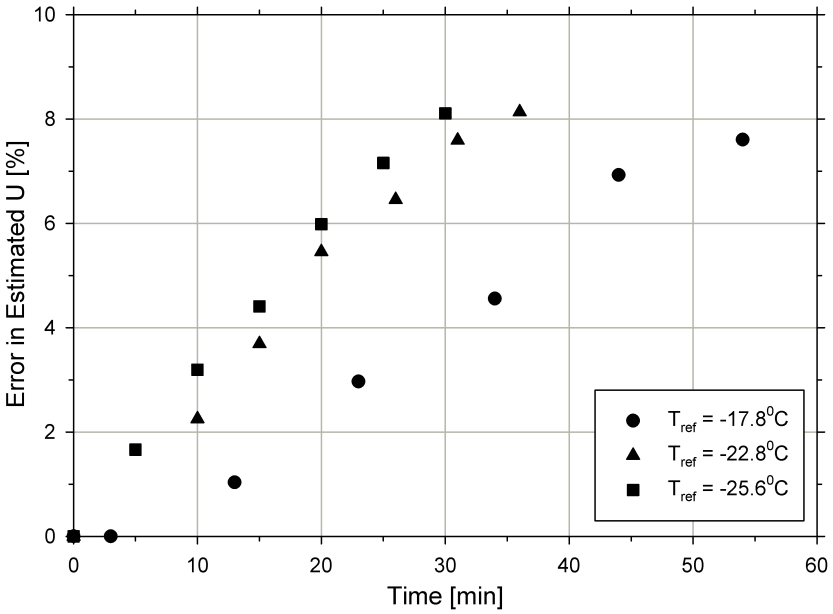

Figure 3.15: Error in U value calculated by current method and by assuming uniform frost thickness

small when the thickness is small and increases as high as 8% at the end of test.

Error in heat transfer area will lead to error in calculation of other significant parameters such as heat transfer coefficient (h_{air}) and fin efficiency (η). An improved method to calculate fin efficiency and air side heat transfer coefficient in a non-uniformly frosted coil thus needs to be developed for use with outdoor coils in heat pumps. Development of such a correlation is beyond the scope of the current study.

3.8 Results & Discussion: Microchannel

The test coil under consideration is a one row microchannel coil with louvered folded fins. The geometry and specifications of the coil is given in Table 3.4. The experimental matrix for microchannel is similar to the fin and tube case except for the tests varying the inlet glycol temperature. The temperatures used for fin and

tube are very low for microchannel coil and the resulting frost time would be too short to produce any meaningful results. The test matrix for microchannel tests is given in Table 3.5. Unlike the fin-tube tests the air flow is allowed to drop as frost grows for microchannel tests. Due to increased pressure drop across microchannel the fan operated near it's high frequency in dry conditions. If tested with same air flow, the fan would hit the maximum frequency within a short period of time. Thus to see a distinguishable trend in frosting patterns fan speed is fixed and flow allowed to drop.

Table 3.4: Geometry and Related Parameters for the Test Microchannel Coil

Microchannel Coil Parameter	Value
Coil Face Area (L x W) [m^2]	0.093 (0.3048 x 0.3048)
Tube Orientation	Vertical
Single Tube Length [mm]	304.8
Tube Depth [mm]	25.4
Tube Height [mm]	1.75
Tube Spacing [mm]	9.32
Fin Pitch [fins/m]	787
Fin Thickness [mm]	0.095
Tube/ Fin material	Aluminum/ Aluminum
Number of ports/Geometry	4/Rectangular

Except for the difference in the way the fan is controlled, the experimental

Table 3.5: Test Conditions for Microchannel Coil

Parameter	T_{ref} [^{0}C]	$\dot{V}_{air}$ [m^3/s]	RH [%]
Refrigerant Temperature	-6.7 -9.4 -12.2	0.09	82
Air flow rate	-9.4	0.07 0.09 0.13	82
Air relative humidity	-9.4	0.09	72 82 92

methodology for microchannel was similar to that of fin-tube. Before the actual tests were performed, trial tests were run to validate the weight measurements with and without stopping fan. It was observed that for the microchannel coils used in this study, the frost grew almost uniformly across the face of the coil. This is due to the fact that glycol flow in the microchannels was fully developed in a very very short distance ($\sim 10D_h$), resulting in more uniform surface temperatures. As a result, the thickness measurements presented is representative of the whole coil and is measured along the middle of the coil.

Figures 3.16 shows the variation of frost thickness for different glycol entering temperatures. As seen with fin and tube coil, the surface temperature has the largest effect on the frost thickness. For the test with the coldest fluid temperature ($T_{ref} = -12.2^0C$), the frost thickness grew very rapidly initially, but flattened towards the end of the test. Such a trend is not visible in the warmest temperature case. The behavior can be attributed to the fact that for colder temperatures the frost accumulates at a low density. As the frost grows and reaches a certain thickness, the vapor removed from air tends to diffuse into the frost layer instead of adding to the frost thickness. This shift in where the vapor ends up in the frost layer causes the flattening of frost thickness for the low temperature case. The experiments are stopped when the air flow drops to 75% of the initial flow. It is worthwhile to note that for all three temperature cases, the final frost thickness is around 70% of the half-fin spacing. This suggests that for microchannel coils, the porosity of the frost is not a factor which significantly affects the air flow. Since in microchannels the frost accumulates at the leading edge of the coil where the air is still in free-flow regime, it is reasonable to suggest that the pressure drop is more sensitive to large scale blockage effects than to small scale porosity effects. Results obtained for different air relative humidity is shown in Figure 3.17. The results are as expected with higher RH causing faster frost growth. For this case also it is seen

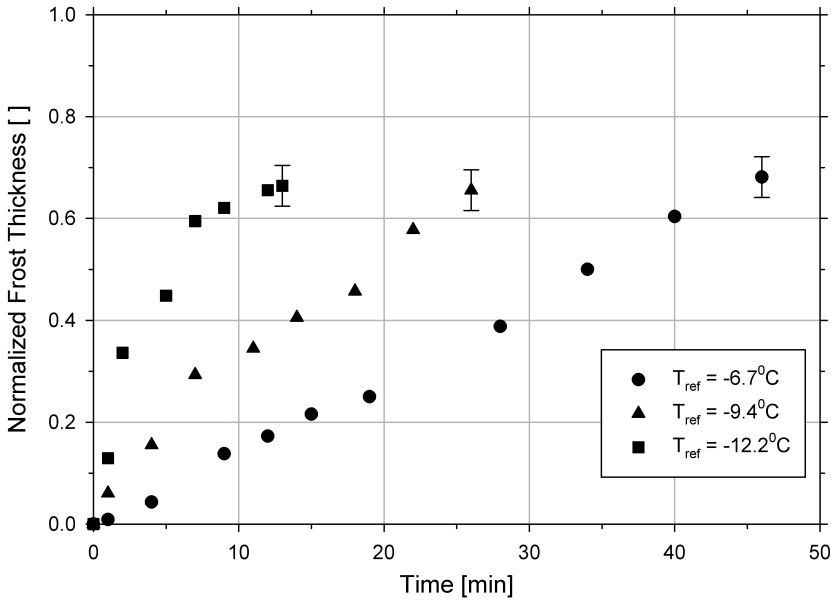

Figure 3.16: Normalized Frost Thickness for Microchannel Coil at Different Glycol Temperatures

that the final frost thickness is similar for all three air RH.

Figures 3.18 & 3.19 shows the frost weight accumulated for different glycol temperatures and air RH respectively. Results are as expected with lower temperatures and higher RH causing greater frost weight accumulation. In contrast to the fin and tube coil, the frost weight for low temperature cases did not flatten out. This is due to the fact that even at the end of the test for low temperature case, the normalized frost thickness was not unity and thus there was still free flow area available for air to flow. In fin and tube coils, for low temperatures the portions of the coil where refrigerant entered was completely covered by frost and thus was not available for any further frost accumulation.

The overall heat transfer coefficient of the heat exchanger drops as the frost grows on its surface. Figure 3.20 shows the drop in the UA value of the test coil for three different glycol entering temperatures. It can be seen that the UA value initially increases and then drops even when the air flow rate drops continuously through the

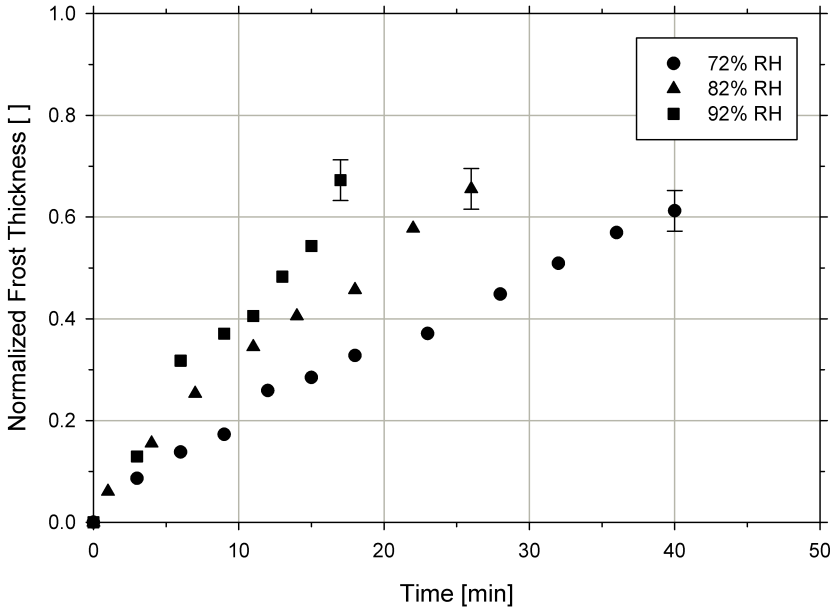

Figure 3.17: Normalized Frost Thickness for Microchannel Coil at Different Air RH

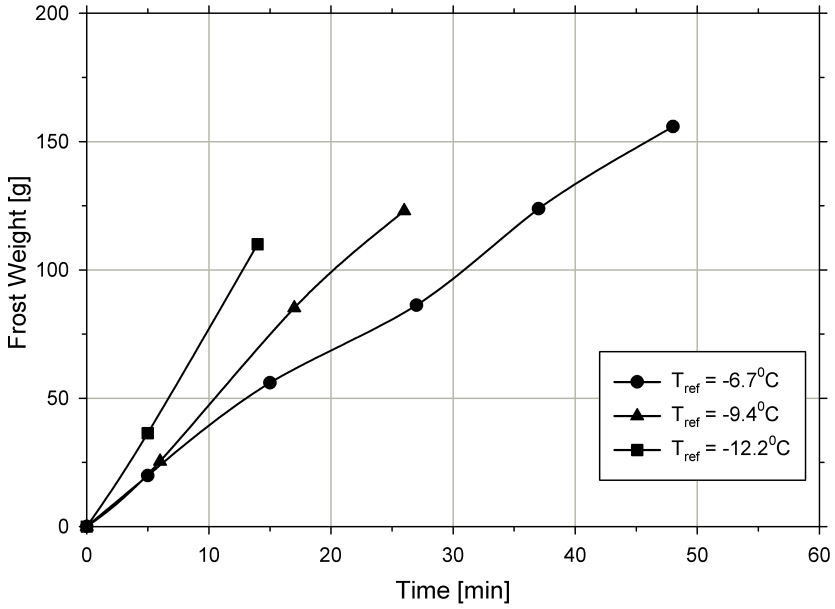

Figure 3.18: Frost Mass for Microchannel Coil at Different Glycol Temperatures

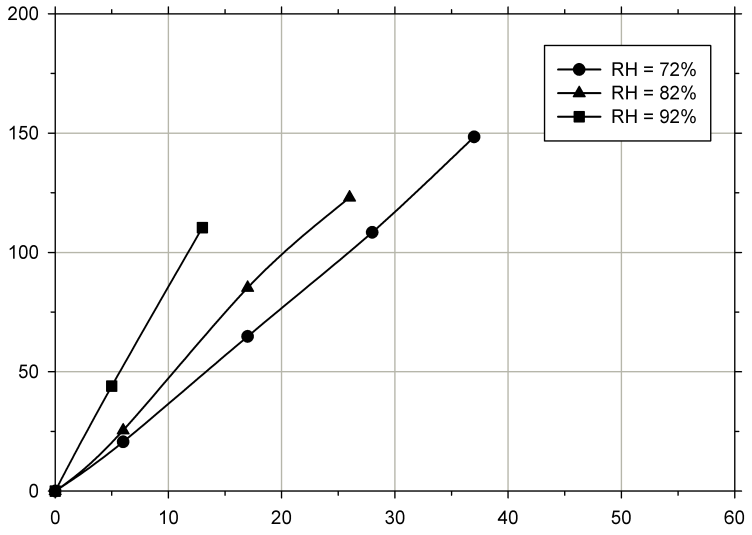

Figure 3.19: Frost Mass for Microchannel Coil at Different Air RH

frosting cycle. The initial increase in overall heat transfer coefficient is due to increased roughness and a subsequent increase in the heat transfer coefficient, which tends to compensate for the drop in air flow rate. As frost thickness increases, the drop in air flow rate is significant, dominating the increase in heat transfer coefficient. It is important to note that the final UA value for all three cases is nearly same, suggesting that the frost density (and subsequently frost conductivity) is not a major factor causing the deterioration of heat exchanger performance. The final UA value for all three cases is similar since the air flow rate begins and ends at same value for all three temperature cases.

As frost grows on the heat exchanger surface the fin characteristics changes due to an added resistance layer. Availability of a heat transfer correlation to be used under frosting conditions is not available in the literature. As a result the accepted approach to obtain the air side heat transfer coefficient is to use the dry coil correlation and use a correction factor to account for frost. Typically the correction factor is developed using a curve fit from the experimental data. In this study also

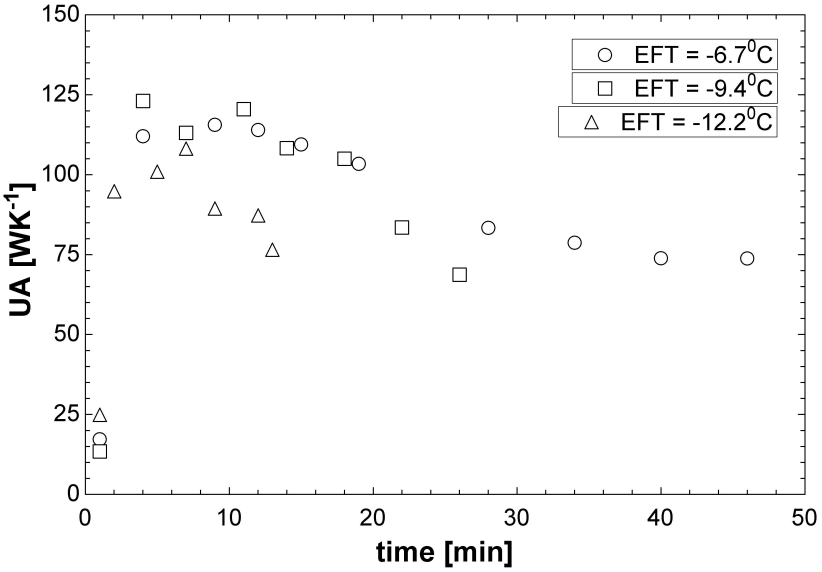

Figure 3.20: Variation of Overall Heat Transfer Coefficient under Different Glycol Temperatures

the dry coil correlation is used during frosting period. However, instead of using an empirically determined correction factor, the frost thickness is directly used in the heat transfer correlation by recalculating the air side hydraulic diameter and subsequently the Reynolds number to account for frost thickness at any time.

In order for this approach to work, the heat transfer correlation used and the experimentally estimated heat transfer correlation must match within accepted tolerance. In order to determine the heat transfer coefficient experimentally, an iterative approach is used. The iterative approach uses a known fin efficiency equation which contains heat transfer coefficient in its formulation. The fin efficiency for a non frosted fin cannot be used for a frosted fin during heat transfer calculations. Various formulations are available in the literature for frosted fin efficiency which are reviewed by Kondepudi and O'Neal (1987). Of all the formulations presented, fin efficiency presented by Sanders (1974) is selected as a better choice due to the applicability for various operating conditions. In addition to the formulations reviewed in the above mentioned article, another formulation

was presented by Xia and Jacobi (2004) by considering two-dimensional conduction through the frost layer.

Fin efficiency is formulated by Sanders as follows:

$$\eta_{fr} = \frac{\tanh m_{fr} L}{m_{fr} L} \tag{3.22}$$

$$m_{fr} = \sqrt{\left[\frac{1}{\frac{\delta_{fr}}{k_{fr}} + \frac{C_{p,a}}{b h_a}} . \frac{1}{\delta_f k_f}\right]} \tag{3.23}$$

Fin efficiency is formulated by Xia as follows:

$$\eta_{fr} = \frac{\lambda}{h_a L \delta_{fr}} \tanh\left(\frac{\lambda L}{\delta_{fr}}\right)(k_{fr}\delta_{fr} + k_f \delta_f) \tag{3.24}$$

$$\lambda = \delta_{fr} \sqrt{\frac{h_a}{k_f \delta_f + \delta_{fr}(h_a k_f \delta_f / k_{fr} + k_{fr})}} \tag{3.25}$$

Where $m_{fr}, \lambda =$ Frosted fin parameter

$b =$ Slope of linear function relating temperature to enthalpy of moist air

$h_a =$ air side heat transfer coefficient

Fin efficiency and heat transfer coefficient obtained from the experimental data points using the two fin efficiency formulations is presented in Figures 3.21, 3.22 & 3.23 for three different glycol entering temperatures.

It can be seen that for warmer temperature case, the heat transfer coefficient predicted by both formulations are very close, while the difference increases as the temperature is lowered. For the lowest temperature case the different in heat transfer coefficient is very significant for the mid portions of the frosting period. Due to the discrepancy it is important that the formulation used in the study match the results predicted by the correlation used in this study. Such a match ensures

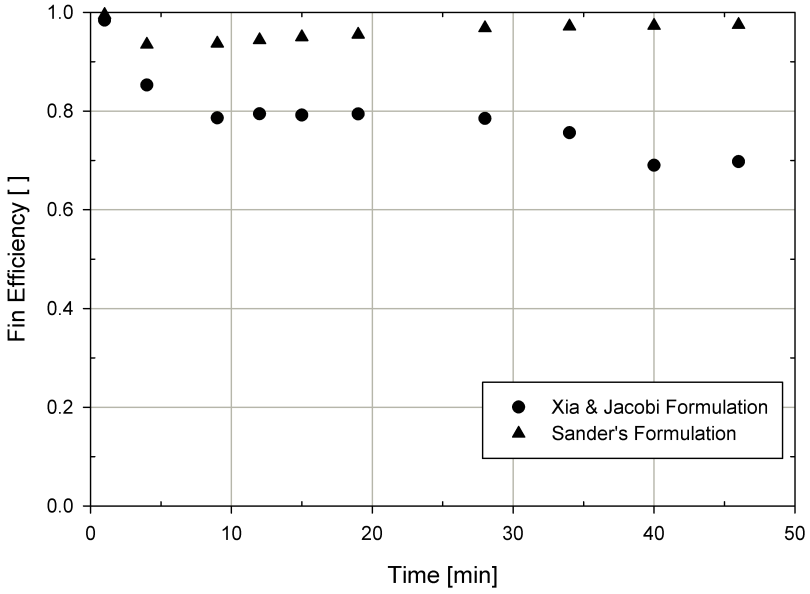

(a) Fin Efficiency

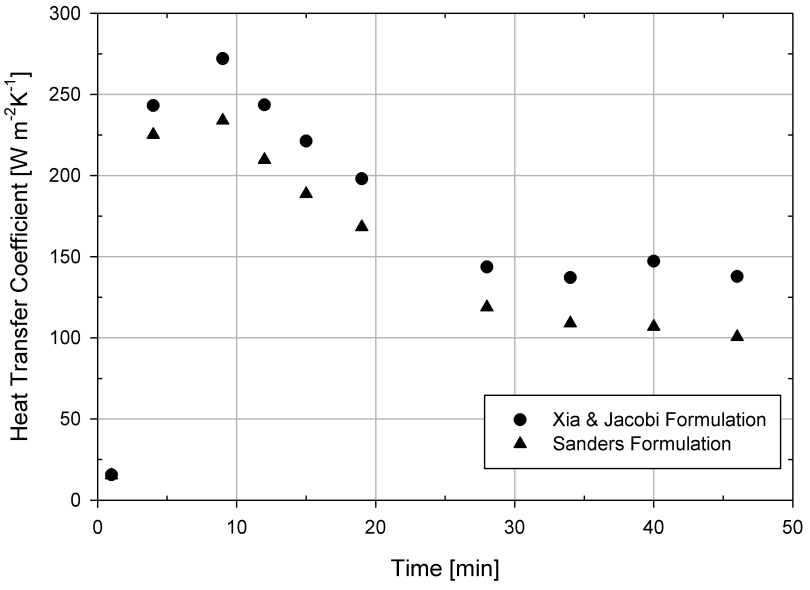

(b) Heat Transfer Coefficient

Figure 3.21: Comparison of Xia & Jacobi Formulation and Sander's Formulation for $T_{ref,in} = -6.7^0C$

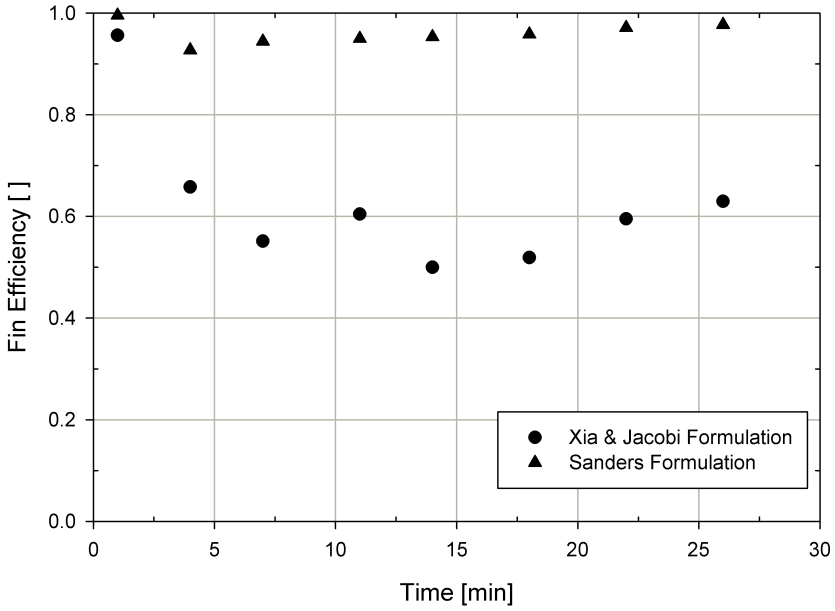

(a) Fin Efficiency

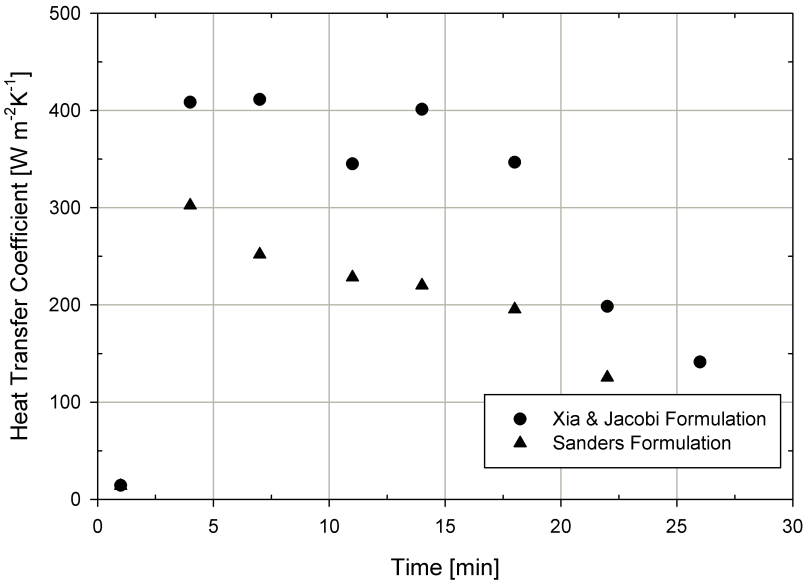

(b) Heat Transfer Coefficient

Figure 3.22: Comparison of Xia & Jacobi Formulation and Sander's Formulation for $T_{ref,in} = -9.4^0C$

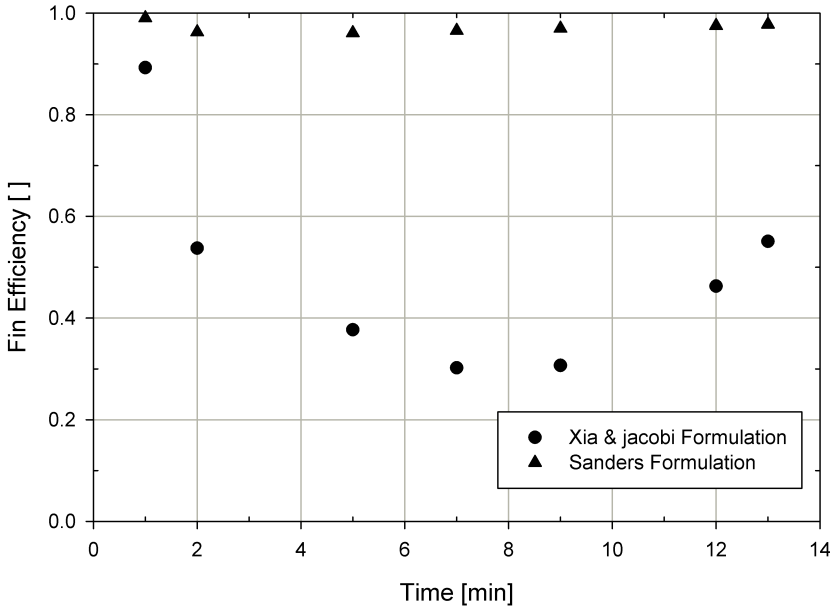

(a) Fin Efficiency

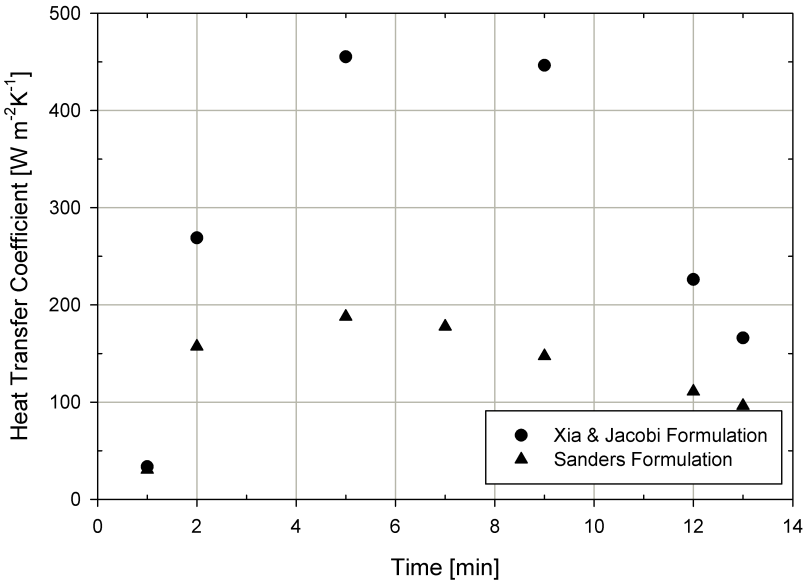

(b) Heat Transfer Coefficient

Figure 3.23: Comparison of Xia & Jacobi Formulation and Sander's Formulation for $T_{ref,in} = -12.2^0C$

that the fin efficiency calculated represents the heat transfer coefficient correctly. The heat transfer correlation used in this study is presented by Kim and Bullard (2002). The values obtained by this correlation by accounting for frost thickness matches both formulations closely for higher temperatures while for the lowest temperature case the predicted values match the Sander's formulation more closely. Sanders' formulation is adopted in this study to obtain the fin efficiency during frost growth due to its close match to the heat transfer correlation used over the entire range of operating temperatures.

3.9 Conclusions

An experimental facility capable of performing frost tests for a wide range of air and refrigerant conditions was designed. Various key parameters related to frost growth, viz., frost thickness, frost weight, air flow and inlet and outlet air temperature and humidities can be measured. Frost tests were performed for varying glycol entering temperatures, air humidity ratios and air flow rates. Frost growth was significantly affected by the glycol temperature (and consequently surface temperature) for both fin-tube and microchannel coils. The rate of frost growth for a microchannel for a given temperature is significantly greater than fin and tube. Type and density of frost formed was heavily influenced by the temperature of the heat exchanger surface. Low temperatures resulted in a less dense frost which covered the fins faster thereby reducing the air flow significantly. As a result the final frost weight accumulated for low temperature cases is approximately 16% lower than the high temperature case in fin and tube heat exchanger. Air humidity ratio also affected the frost growth rate on the heat exchanger surfaces. Higher humidity ratio caused faster and higher frost accumulation. The density of frost was not significantly influenced by the air humidity ratio. A change of 20% in air relative humidity

resulted in the rate of frost growth to vary by 80% (once the frost is initiated). Air flow rate (air face velocity) did not have a significant impact on the rate of frost accumulation. The frost growth rate and accumulation for range of air face velocities typically seen in outdoor coils of residential and light commercial heat pumps were found to be within experimental uncertainty. The variation in frost thickness observed for a high air flow and low air flow conditions was mostly within $\pm 5\%$ with the highest variation being $\pm 10\%$. The conventional method of heat transfer coefficient deduction is not suitable in the case of a non-uniformly frosted coil. The limiting range of non-uniformity on the face of the coil which can allow a uniform frost thickness assumption needs to be analyzed. For a near-uniformly frosted coil (as is the case for microchannel), the air side heat transfer coefficient can be deduced by accounting for frost layer thickness and resistance in hydraulic diameter fin efficiency calculations. For the range of conditions covered in this study for microchannel heat exchanger, it was found that a 1-D heat conduction through the frost layer is a good assumption.

CHAPTER 4

DEVELOPMENT AND VALIDATION OF A FROST GROWTH MODEL FOR USE IN HEAT EXCHANGER SIMULATION

4.1 Introduction

Frost growth is a complex heat and mass transfer phenomenon. Understanding the performance of heat exchangers working in frosting conditions is complicated by the fact that the rate of frost growth varies from inlet to outlet of the heat exchanger circuits. This results in a continuous redistribution of air flow over the face of the heat exchanger during the frosting process. In addition, as frost grows on the fin and tube surfaces, the heat transfer area changes along with the free flow area. The direct effect of frost is two fold; firstly an increase in air side resistance to heat transfer and secondly an increase in air side resistance to flow. thereby reducing performance. Previous models have either ignored the redistribution of air flow due to non-uniformity of frost thickness at various locations or assumed uniform frost thickness over the entire heat exchanger. Such a model introduces significant error if the fin/tube temperatures vary considerably over the heat exchanger. In order to effectively integrate the frost growth model in a heat exchanger simulation algorithm, all variables of interest needs to be solved within the boundary conditions (not the surface temperatures) on the air and refrigerant side, since the boundary conditions are the only known inputs. Usefulness of the model is also dependent on correctly adjusting different areas like fin area, tube area and minimum free flow area which inherently changes due to frost growth during the entire frosting period.

Kondepudi and O'Neal (1989, 1993) presented expressions for fin efficiency and overall heat transfer coefficients for heat exchangers, but they did not implement the correlations in a simulation model. Yang et al. (2006b) presented a time marching model for frost growth in heat exchangers which can be used with a segmentation model. This model, however, does not calculate the surface temperature, but requires it as an input to the model. A finite difference model was presented by Chen et al. (2000*a*). This model significantly increased the computation time of the overall heat pump simulation. A frost growth model for heat exchangers based on scaling was presented by Storey and Jacobi (1999). A significant shortcoming of this model was that it did not consider diffusion in the frost layer and assumed that heat and mass transfer coefficients remain constant throughout the frosting period. Models available in the literature generally lacked the ability to simulate the effect of time-delayed onset of frost nucleation due to effects of local fin temperature and the subsequent re-distribution of airflow across the heat exchanger during the frosting process.

4.2 Theoretical Development of Model

4.2.1 Validity of the Quasi-Steady Assumption

The problem of frost growth is a transient problem with combined heat and mass transfer. The situation is further complicated by the moving frost boundary. Previous researchers (Kondepudi and O'Neal, 1993; Lee et al., 1997; Yang et al., 2006) have modeled frost growth as a quasi steady state phenomenon. However the supporting basis for such an assumption is not available in the literature. A theoretical analysis of the governing equations is presented and a condition for validity of steady state assumption is derived in this section. The solution domain

that is considered is shown in Figure 4.1. A control volume covering the frost layer and fin surface is shown such that an energy balance can be applied to such that fin surface temperature can be calculated. The following assumptions are made in the development of the equations below:

1. Local density variations inside the frost layer can be neglected and the whole frost layer can be represented by average properties.

2. The frost layer thickness does not increase when the surface temperature reaches the triple point temperature of water.

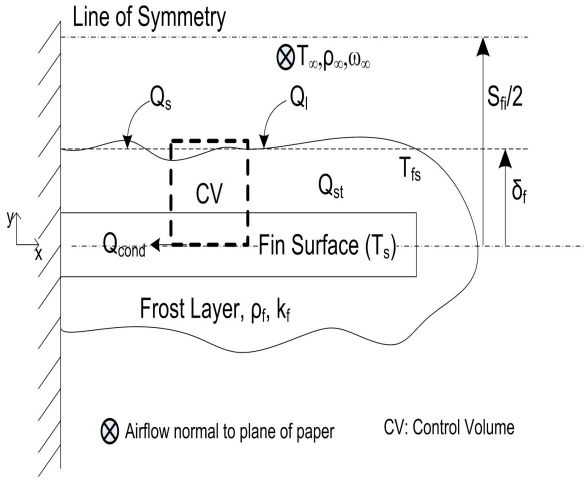

Figure 4.1: Solution Domain Showing a Control Volume around Fin Surface

Applying an energy balance per unit area of the frost layer and considering an energy storage term, we get:

$$k_f \left(\frac{\partial T_f}{\partial y} \right)_0 = \dot{Q}_s + \dot{Q}_l - \dot{Q}_{stored} \tag{4.1}$$

The rate of latent energy released due to freezing is equal to the rate of increase in the frost mass and can be represented as

$$\dot{Q}_l = h_{sg} \frac{d\dot{m}_f}{dt} \tag{4.2}$$

The mass of frost inside the frost layer is equal to the product of the frost density and the frost volume. From the previous assumption of equivalent average frost density and considering a unit area, the rate of latent energy is

$$\dot{Q}_l = h_{sg}\bar{\rho}_f \frac{d\delta_f}{dt} + h_{sg}\delta_f \frac{d\bar{\rho}_f}{dt} \tag{4.3}$$

Applying (4.3) in (4.1) and using standard definitions for sensible heat transfer and energy storage we can rewrite the energy balance at fin surface as

$$k_f \left(\frac{\partial T_f}{\partial y}\right)_0 = h(T_\infty - T_{fs}) + h_{sg}\bar{\rho}_f \frac{d\delta_f}{dt} + h_{sg}\delta_f \frac{d\bar{\rho}_f}{dt} - \bar{\rho}_f C_{p,f}\delta_f \frac{\partial T_f}{\partial t} \tag{4.4}$$

The energy balance equation can be non-dimensionalized using the dimensionless parameters as shown below. Selection of the triple point of water as the scaling parameter seems logical since the frost surface cannot go beyond that temperature without melting/ refreezing.

$$\theta = \frac{T_f - T_{tp}}{T_{surf} - T_{tp}} \quad \delta^* = \frac{\delta_f}{S_{fi}}$$
$$Y = \frac{y}{S_{fi}} \quad \rho^* = \frac{\bar{\rho}_f}{\rho_i}$$

Incorporating these dimensionless parameters into the energy balance and rearranging the terms we get the final equation as

$$\left(\frac{\partial \theta}{\partial Y}\right)_0 = \frac{\rho_i h_{sg} S_{fi}^2}{k_f \Delta T}\rho^* \frac{d\delta^*}{dt} + \frac{\rho_i h_{sg} S_{fi}^2}{k_f \Delta T}\delta^* \frac{d\rho^*}{dt} - \frac{\rho^* \rho_i C_{p,f} S_{fi}^2}{k_f}\delta^* \frac{d\theta}{dt} + \frac{h S_{fi}}{k_f}\left(\frac{T_\infty - T_{fs}}{\Delta T}\right) \tag{4.5}$$

Where the temperature difference $\Delta T = |T_s - T_{tp}|$

Equation (4.5) is the final scaled form of the energy balance in the frost layer, and it can be seen that there are two time constants in the equation. One time constant is related to the rate of change in frost thickness and density (t_{c1}) while the other time constant refers to the rate of change in temperature (t_{c2}). These two time constants

are obtained from the equation as follows

$$t_{c1} = \frac{\rho_i h_{sg} S_{fi}^2}{k_f \Delta T} \quad \text{and} \quad t_{c2} = \frac{\rho_f C_{p,f} S_{fi}^2}{k_f}$$

An order of magnitude approach is used to check for the condition when a quasi steady state assumption is valid. For the assumption of quasi-steady state to be valid we require $t_{c1} >> t_{c2}$. Physically, this condition means that the temperature field inside the frost layer stabilizes more quickly than the density and thickness of frost layer as a response to a change in boundary conditions. In other words, such a condition will allow us to decouple the heat exchanger solution and the frost growth solution, thereby reducing the simulation time considerably. With the values of the time constants evaluated above and rearranging we get, for a valid quasi steady state assumption

$$\frac{\rho_f C_{p,f} \Delta T}{\rho_i h_{sg}} << 1$$

The dimensionless quantity that arises in the left side of the equation above can be identified as the Jakob number. Thus for a valid quasi steady state assumption in problems similar to frost growth we require

$$Ja << 1 \tag{4.6}$$

For heat pump applications the frost growth on outdoor coils will always satisfy this condition. This is due to the fact that in heat pump applications the difference between the plate temperature and the triple point of water is not significant enough to compensate for a low ratio of specific heat to latent energy of sublimation. In some cryogenic applications, where surface temperature is well below sub-freezing temperature, the condition of Eq (4.6) does not hold and a quasi steady assumption becomes invalid. The condition derived here also suggests that

quasi-steady state assumption will break down at extremely low frost thickness such as in the matrix growth phase which is consistent with observation by Lock (1990).

4.3 Frost Growth Model

The frost growth model is developed for a segment-by-segment heat exchanger model based on the following assumptions:

1. Frost model is quasi-steady state. All variables are constant over an entire time step and no energy is stored in the frost layer during a timestep.

2. Frost thickness profile is the same for each fin in a given segment of the heat exchanger. Frost thickness is same along the fin in the direction of the air flow. This assumption will be relaxed in future.

3. Frost growth is one dimensional. Frost grows only in the direction perpendicular to the air flow.

4. Analogy between heat and mass transfer coefficients exist. This assumption allows us to represent mass transfer coefficient in terms of heat transfer coefficient.

5. Air inside the frost layer is saturated at the local frost temperature. This allows us to use the Clausius-Clapeyron relation to express vapor pressure in terms of frost temperature.

To develop the frost growth model we consider a control volume that is drawn around the frost surface. A sketch of the solution domain for the frost growth model described here is shown in Figure 4.2. Domain height ($S_{fi}/2$) is half the spacing of

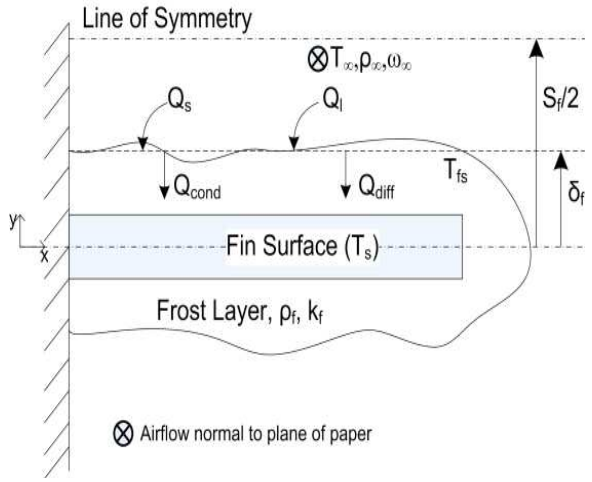

Figure 4.2: Solution Domain Showing a Control Volume around Frost Surface and Associated Energy Transfers

the fin. The approach described here can be used for the tube side also by correctly accounting for areas.

The amount of energy transferred from the air to the frost layer at the frost surface is divided into two parts, viz sensible and latent which are obtained as follows:

$$\dot{Q}_s = hA_{fs}(T_\infty - T_{fs}) \tag{4.7}$$

$$\dot{Q}_l = h_m A_{fs}(\rho_\infty - \rho_{fs}).h_{sg} \tag{4.8}$$

Total heat transferred from air leaves the control volume through conduction and mass diffusion. Water vapor mass transferred from the air to the frost layer is split into two parts; a fraction becomes frost at the surface and increases the thickness of the frost, while the remaining fraction diffuses into the frost layer due to the difference in vapor partial pressure of the air near frost surface and air near the fin/tube surface. The rate of water vapor frosting at the surface is obtained as:

$$\dot{m}_{f,\delta} = h_m A_{fs}(\rho_\infty - \rho_{fs}) - \dot{m}_{f,\rho} \tag{4.9}$$

where $\dot{m}_{f,\rho}$ is the rate of water vapor diffusion into the frost layer which is governed by Fick's law of diffusion.

$$\dot{m}_{f,\rho} = D_{eff} \frac{\partial \rho_v}{\partial y} \tag{4.10}$$

Effective diffusivity can be represented in terms of the ratio of the density of frost and ice as described by O'Neal (1982). The equation takes into account the increase in mean travel length (tortuosity, τ) due to porous nature of the frost. Taking into account the tortuosity of the frost layer, the binary diffusion coefficient (D_{AB}) is corrected as described by Brian et al. (1969) to give the effective diffusion coefficient.

$$D_{eff} = \frac{D_{AB}}{\tau} \left(1 - \frac{\rho_f}{\rho_{ice}} \right) \tag{4.11}$$

Since the frost layer is porous, the water vapor diffusing through the frost surface will not travel in a straight line. The mean free path follows the porosity of the layer; High porosity results in near straight mean free path and vice-versa (Shah, 1968). This change in mean free path is represented as tortuosity. The density of the frost will increase as it grows and ultimately reaches the density of ice. During this growth process porosity of the frost layer decreases until the frost becomes ice, at which point the frost layer is not porous any more. Thus it is natural to express the tortuosity (result of porosity) in terms of the ratio of density of frost (porous) and density of ice (ρ_i). Such an expression for tortuosity was provided by Sanders (1974)

$$\tau = 1 + \left(\frac{\rho_f}{\rho_i} \right)^{0.5} \tag{4.12}$$

The vapor pressure gradient in the frost layer in Eq (4.10) can be expressed in terms of the temperature gradient using the Clausius-Clapeyron equation as shown below

$$\frac{\partial \rho_v}{\partial y} = \left(\frac{h_{sg}}{v T_{sat}} - \frac{p_v}{T_{sat}} \right) \frac{1}{R T_{sat}} \left(\frac{dT_f}{dy} \right) \tag{4.13}$$

Incorporating these modifications to (4.10) and rearranging, the mass of water vapor that diffuses into the frost layer is represented as in (4.14)

$$\dot{m}_{f,\rho} = A_s D_{AB} \left[\frac{1 - (\rho_f/\rho_i)}{1 + (\rho_f/\rho_i)^{0.5}} \right] \frac{p_v}{RT_{sat}^2} \left(\frac{h_{sg}}{RT_{sat}} - 1 \right) \frac{dT_f}{dy} \tag{4.14}$$

Applying an energy balance at the frost surface shown in Figure 1, we conclude that the heat conducted through the frost layer must be equal to the sum of the sensible heat transfer from the air to the frost surface and the latent heat transfer due to sublimation of water vapor at the frost surface. Equation (4.15) shows the energy balance applied at the frost surface

$$k_f \frac{\partial T_f}{\partial y} = h(T_\infty - T_{fs}) + \left[h_m(\rho_\infty - \rho_{fs}) - M \frac{\partial T_f}{\partial y} \right] h_{sg} \tag{4.15}$$

Where $M = D_{AB} \left[\frac{1-(\rho_f/\rho_i)}{1+(\rho_f/\rho_i)^{0.5}} \right] \frac{p_v}{RT_{sat}^2} \left(\frac{h_{sg}}{RT_{sat}} - 1 \right)$

Storey and Jacobi (1999) had earlier presented a scaled model for determining frost growth in parallel plates. Their approach can be used at this point by introducing two significant modifications that capture the following phenomenon:

1. *Water vapor diffusion into the frost layer.* Neglecting water vapor diffusion tends to over predict the frost thickness and under predict the frost density.

2. *Change in heat and mass transfer coefficient during frosting period.* Assuming a constant heat and mass transfer coefficient in heat exchangers with closely spaced fins does not account for the change in heat exchanger frontal area due to frost growth. Change in frontal area causes the Reynolds number to change and subsequently the heat transfer coefficient also changes. A change in heat transfer coefficient leads to a change in mass transfer coefficient.

Following the scaling approach the final form of the frost surface energy balance equation in terms of discretized temperature and density differences is obtained as:

$$k_f(\rho_f)\frac{\Delta T_f}{\delta_f} = h\Delta T_\infty + \left[h_m\Delta\rho_\infty - M\frac{\Delta T_f}{\delta_f}\right]h_{sg} \tag{4.16}$$

Average frost density can also be calculated as the total frost mass per unit volume of frost. It is thus expressed as

$$\bar{\rho}_f = \frac{\int_0^t h_m\Delta\rho_v dt}{\delta_f} \tag{4.17}$$

Applying the heat and mass transfer analogy, the mass transfer coefficient is expressed in terms of the heat transfer coefficient as

$$h_m = \frac{h}{\rho_a c_{p,a}} \tag{4.18}$$

An appropriate heat transfer correlation is used to relate the heat transfer coefficient to frost thickness by varying Reynolds number and related area. An empirical correlation that connects frost density to frost surface temperature proposed by Hayashi et al. (1977a) is used to close the system of equations.

$$\rho_f = 670e^{0.277T_{fs}} \tag{4.19}$$

Equations (4.16), (4.17), (4.19) along with the applicable heat transfer correlation represent a system of four equations for the frost layer. Since in a heat exchanger simulation program the surface temperature is not a known quantity, we need one more equation which introduces refrigerant temperature to the system of equations. Neglecting the resistance of the tube, an energy balance on the tube surface is

shown as follows

$$h_i A_i (T_s - T_r) = h A_o (T_\infty - T_{fs}) + h_m A_o (\rho_\infty - \rho_{fs}) h_{sg} \tag{4.20}$$

The system of equations is thus closed and can be solved with a non-linear system solver for any time step with air and refrigerant temperature.

4.4 Model Implementation

The frost model described in the previous section is implemented in a segment-by-segment heat exchanger program. Iu (2007) developed a heat exchanger simulation algorithm with capability to simulate complex circuitry in heat exchangers. Each tube in the heat exchanger is divided into multiple segments in the direction of refrigerant flow and each segment is simulated using a epsilon-NTU method. Refrigerant flow rate in each circuit is calculated such that pressure drop across parallel circuits are equal. Steady state is achieved when refrigerant flow rates and air conditions (for multiple rows) converge.

The heat exchanger is divided into a number of segments in the direction of refrigerant flow as shown in Figure 4.3 and each segment is treated as an elemental heat exchanger. A single heat exchanger element is shown in Figure 4.4. The figure showing a segment for a fin and tube coil is for illustrative purposes. The model is applicable to a microchannel heat exchanger as well which is discretized in the direction of refrigerant flow. Each element is simulated successively using the outlet conditions of upstream segment as inlet conditions to the next segment. Each segment is assumed to behave as a counter-cross flow heat exchanger and simulated using the $\epsilon - NTU$ approach (Incropera et al., 2006). A brief explanation on the heat exchanger solution algorithm is provided here to aid the understanding of the

model implementation. The equations are presented for dry coils along with applicable modifications required to handle wet coils.

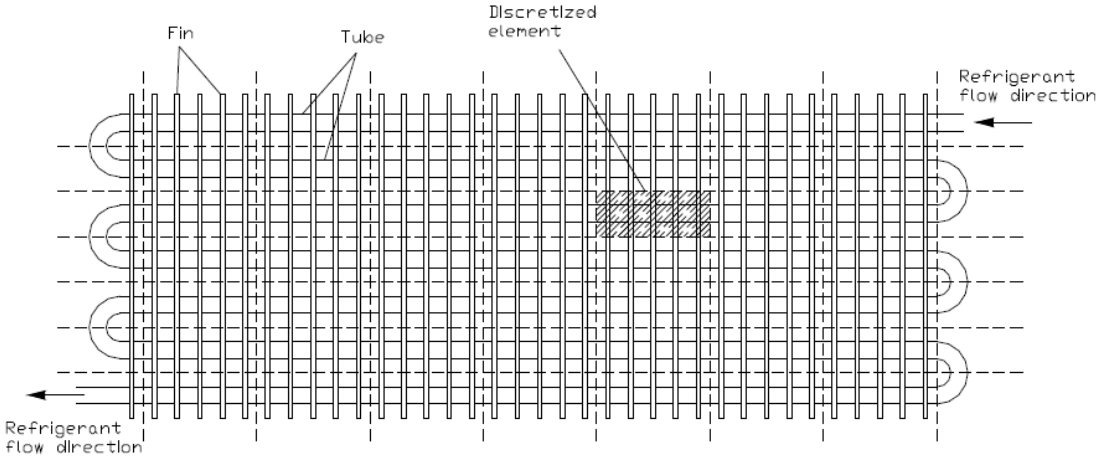

Figure 4.3: Schematic showing Heat Exchanger Discretization

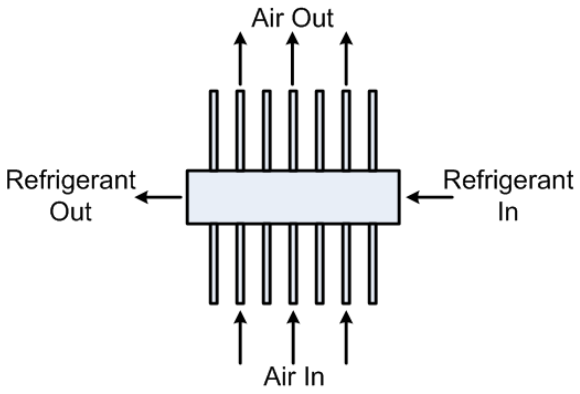

Figure 4.4: Single Heat Exchanger Segment

For a given heat exchanger under air cooling applications the maximum possible heat transfer is given by

$$\dot{Q}_{max} = C_{min}(T_{a,i} - T_{r,i}) \tag{4.21}$$

Where $C_{min} =$ Minimum heat capacity

$T_{a,i} =$ Air inlet temperature

$T_{r,i} =$ Refrigerant inlet temperature

Actual heat transfer for the heat exchanger is equal to

$$\dot{Q} = \epsilon C_{min}(T_{a,i} - T_{r,i}) \tag{4.22}$$

Where $\epsilon =$ Effectiveness of heat exchanger

In order to calculate the effectiveness of the heat exchanger we first need to calculate the overall conductance (UA). Heat exchanger overall conductance is a function of internal and external heat transfer coefficients, internal and external heat transfer areas and surface effectiveness due to fin. Under frosting conditions the operation is transient and the air side heat transfer coefficient, heat transfer area and fin efficiency does not stay constant. Accounting for variation in heat transfer coefficient and area due to frost growth is straight forward while fin efficiency calculation are not.

Fin efficiency for both fin-tube and microchannel heat exchangers are is calculated using the approach presented by Schmidt (1949) as

$$\eta_{fin,ft} = \frac{\tanh\left(m_{fr} d_{collar}/2\phi\right)}{m_{fr} d_{collar}/2\phi} \qquad \eta_{fin,mc} = \frac{\tanh\left(m_{fr} L_{fi}\right)}{m_{fr} L_{fi}} \tag{4.23}$$

Where $m_{fr} =$ Fin efficiency parameter during frosting

$\phi =$ $(R_r - 1)\left[1 + 0.35 \ln R_r\right]$

$R_r =$ Radius ratio as defined in Schmidt (1949)

One approach to calculate fin efficiency during frost growth is to consider the fin along with frost as a single unit (Barrow, 1985; Kondepudi and O'Neal, 1993;

Sanders, 1974). The fin efficiency parameter (m_{fr}) used in efficiency calculation needs to account for the frost layer, since it affects the effective thermal conductivity between air and the fin surface. Expression proposed by Barrow (1985) is very simplistic and did not follow from the underlying heat transfer mechanism. Expression proposed by Kondepudi and O'Neal (1993) was for pin fins and is not valid for radial fins or straight fins. Sanders (1974) proposed an expression for fin efficiency parameter that can be used widely and also derived from basic energy balance equations in the fin. The expression also accounted for latent energy transfer through the frost layer which is not accounted in other formulations. Another approach is a more detailed one in which fin efficiency is presented as a series solution (for fin-tube heat exchangers Bessel functions are involved) obtained by considering a 2-D conduction through the frost layer. Sommers and Jacobi (2006) presented such a solution for fin-tube and Xia and Jacobi (2004) presented a solution for microchannel heat exchangers.

Fin-efficiency expression presented by Sommers and Jacobi (2006) is mathematically intensive and does not offer any distinct advantages compared to formulation presented by Sanders (1974). Formulations presented by Xia and Jacobi (2004) and Sanders (1974) for microchannel heat exchanger are compared in 3.8. It was concluded that formulation by Sanders (1974) better matches with the heat transfer correlation over the range of temperatures used in this study for microchannel heat exchangers. Once a fin efficiency value is obtained the total surface effectiveness for the heat exchanger (both fin-tube and microchannel) is calculated as

$$\eta_{surf} = 1 - \frac{A_{fin}}{A_{out}} \left(1 - \eta_{fin}\right) \tag{4.24}$$

With all required parameters calculated we can proceed to determine the UA of the

heat exchanger. Neglecting the tube resistance, UA can be written as

$$\frac{1}{UA} = \frac{1}{h_r A_r} + \frac{\ln\left(\frac{d_{tube,o} + \delta_f}{d_{tube,o}}\right)}{2\pi k_f L} + \frac{1}{\eta_{surf} h_{air} A_o} \tag{4.25}$$

Number of transfer units (NTU) for the heat exchanger is found using

$$NTU = \frac{UA}{C_{min}} \tag{4.26}$$

For single phase refrigerant, depending on whether refrigerant or air side has minimum capacity, the effectiveness is calculated using Eq (4.27)-(4.28) respectively.

$$\epsilon = \frac{1}{C_R}\left(1 - \exp -C_R[1 - \exp(-NTU)]\right) \tag{4.27}$$

$$\epsilon = 1 - \exp -C_R[1 - \exp(-C_R NTU)] \tag{4.28}$$

where C_R is the capacitance ratio

For refrigerant in two phase the effectiveness is calculated as

$$\epsilon = 1 - \exp(-NTU) \tag{4.29}$$

A flowchart describing the heat exchanger simulation procedure is shown in Figure 4.5. The algorithm shows all the details in the simulation procedure.

Equations developed as part of the frost model in the previous section are solved simultaneously for each segment in a given time step. A Newton-Raphson solver for non-linear system of equations is implemented in FORTRAN for this purpose. As explained in the previous section, a heat transfer correlation is required to solve the frost equations. Frost growth results in reduced free flow area thereby affecting the heat transfer coefficient. Though the value of the heat transfer coefficient changes as

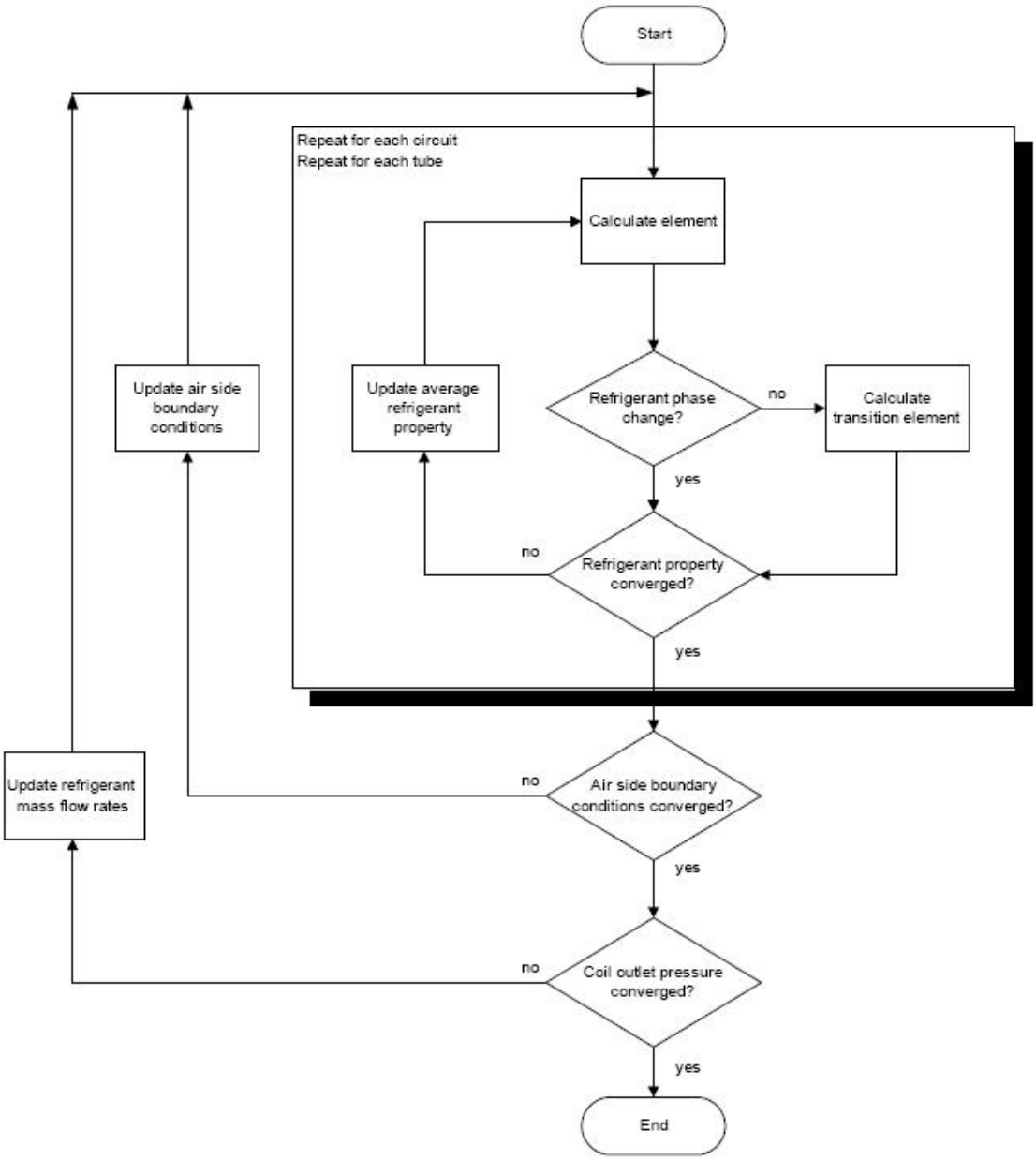

Figure 4.5: Flow Chart Showing Segment-by-Segment Heat Exchanger Algorithm (Iu, 2007)

a result of frost, it is assumed that the form of the equation remains constant throughout the frosting period. This assumption allows us to calculate the heat transfer coefficient by just adjusting the hydraulic diameter (subsequently the Reynolds number) to account for frost thickness. The model is implemented for both a fin-tube and a microchannel coils as will be discussed here.

4.5 Airflow Redistribution Algorithm

When frost grows non-uniformly on a coil, it results in an unequal air flow resistance across the face of the coil. Air at the face of the coil will subsequently redistribute such that the pressure drop across each segment in the heat exchanger is equal. As air redistributes across the face of the coil, the frost growth rate is also expected to vary due to tight coupling between the two phenomena.

Friction factor correlation shown in Eq (4.30) presented by Wang et al. (1999) is used for the fin and tube coil while for microchannel the friction factor is obtained using Eq (4.31) proposed by Kim and Bullard (2002).

$$f = 0.00317 Re_{D_c}^{f_1} \left(\frac{(1/F_p)}{P_r}\right)^{f_2} \left(\frac{D_h}{D_c}\right)^{f_3} \left(\frac{L_h}{L_p}\right)^{f_4} \left(\ln\left(\frac{A_{o,coil}}{A_{br,coil}}\right)\right)^{-6.0483} \tag{4.30}$$

$$f = Re_{Lp}^{-0.781} \left(\frac{L_\alpha}{90}\right)^{0.444} \left(\frac{F_p}{L_p}\right)^{-1.682} \left(\frac{H}{L_p}\right)^{-1.22} \left(\frac{F_d}{L_p}\right)^{-0.818} \left(\frac{L_l}{L_p}\right)^{1.97} \tag{4.31}$$

The form of the friction factor correlation is assumed to remain constant throughout the frosting period. The air side pressure drop across the across any segment of the heat exchanger (both fin-tube and microchannel) is then calculated using Eq (4.32) as given by Kays and London (1984).

$$\Delta P = \frac{G_a}{2\rho_{in}} \left[\left(K_i + 1 - \sigma^2\right) + 2\left(\frac{\rho_{in}}{\rho_{out}} - 1\right) + f\left(\frac{A_o}{A_m}\right)\left(\frac{\rho_{in}}{\rho_{out}}\right) - \left(1 - \sigma^2 - K_e\right)\frac{\rho_{in}}{\rho_{out}} \right] \tag{4.32}$$

Since the frost model assumes a quasi-steady state operation, coil model and frost model is decoupled. By lagging the refrigerant inlet and outlet temperatures, an energy balance on tube surface yields tube temperature with out any iteration. A flow chart describing the implementation of the frost model for a stand alone coil is shown in Figure 4.6.

For the first time step, the coil is simulated under no-frost conditions to give the refrigerant temperatures. The simulation then proceeds to solve the frost model along with the air redistribution algorithm. In the frost model for first timestep, the inlet air mass flow rate is assumed to be uniformly distributed across the coil. Frost equations are solved for each segment to give frost thickness, frost mass, frost surface temperature and frost density. With the calculated frost thickness, air side pressure drop for that particular segment is also calculated using (4.32). As shown in Figure 4.6, once the frost model is solved for each segment the simulation checks if the air side pressure drops across each segment is equal. If the pressure drop is not uniform, the air flow rate through each segment is adjusted and the solution of frost equations is repeated. The process is repeated until the pressure drop across each segment is equal at which point the simulation proceeds to the next timestep. For subsequent time steps the updated frost thickness and redistributed air flow information is used by the coil model in the next timestep to calculate new heat transfer rate for each segment. The previous timestep air flow map is used as an initial guess for the air redistribution algorithm in current timestep.

4.6 Sensitivity Study

Frost growth model presented earlier in the chapter is based on three empirical correlations, viz. frost density, frost conductivity and heat transfer coefficient. In addition another important assumption is that the Lewis number for frost growth conditions is unity. While the heat transfer correlation used in the study is specifically developed for the coil used, the correlations for density and conductivity of frost are not specific to this study. Density of frost is very important in the frost mass balance calculations which yield the frost thickness and weight. Conductivity of frost is important in calculating the heat transfer through frost which affects the

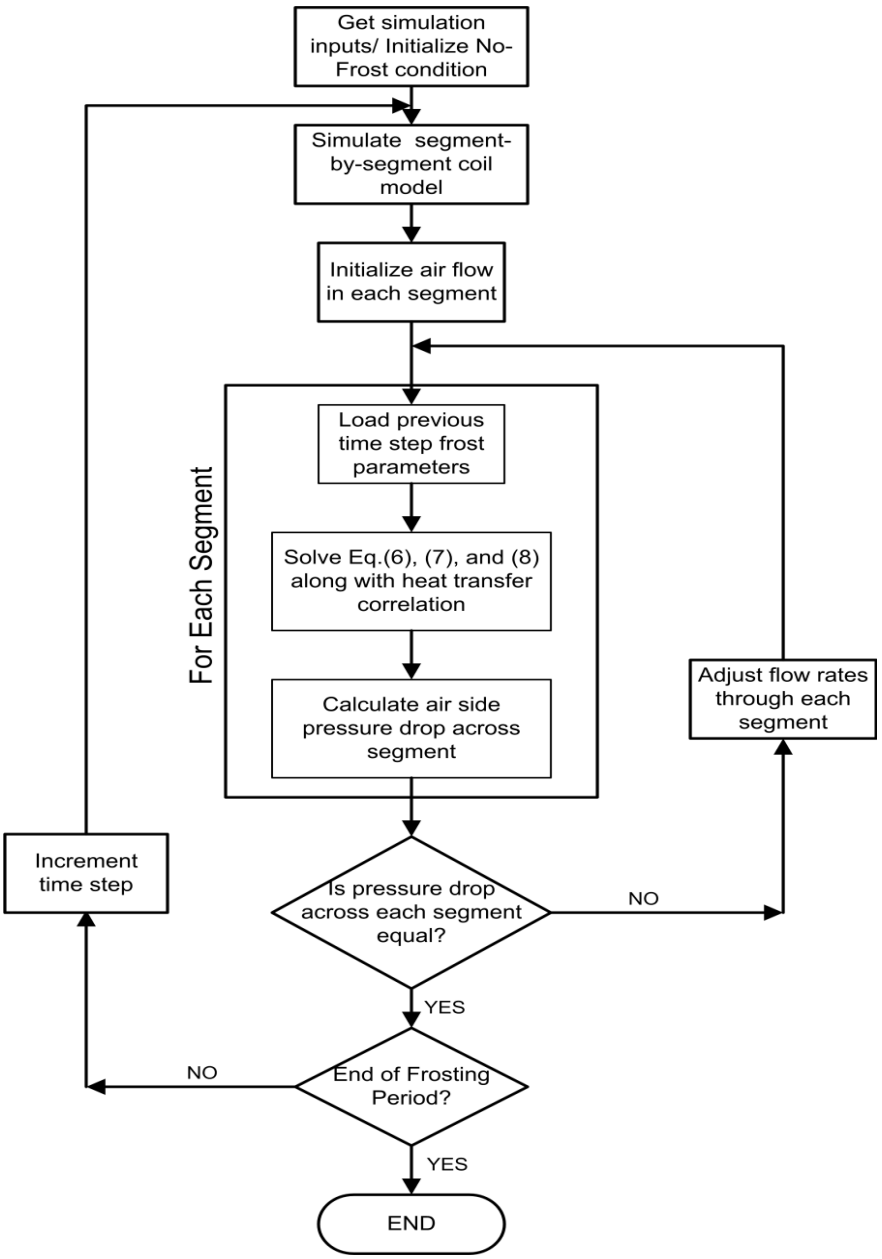

Figure 4.6: Algorithm for Airflow Redistribution during Frosting

fin surface heat balance. Various correlations are developed in the literature for frost density and frost conductivity (Hayashi et al., 1977a,b; Şahin, 2000). All correlations present frost density as a function of frost surface temperature and frost conductivity as function of density.

Since the frost model is highly dependent on the three correlations mentioned above, it would be worthwhile to understand how the error in the correlation will affect the results of frost model. The sensitivity analysis is carried out by perturbing four quantities individually to replicate the possible error in correlation. The four quantities viz., Frost density, heat transfer coefficient, frost conductivity and Lewis number are each perturbed by $\pm 10\%$ from the base line calculated value. While one quantity is perturbed, other quantities are kept at base line calculated values. This allows us to isolate the effect of each quantity individually. Since the frost model simulation is not a steady state one point calculation, the results are presented as a root mean square error over the base line value. Though the approach might not give an exact picture of the model at each time, it is quite representative of the error over the entire frost growth period.

Table 4.1 shows the results of sensitivity study for the fin-tube heat exchanger for the entering glycol temperature of -17.8^0C. It can be seen that the frost thickness is sensitive to both frost density and heat transfer coefficient. Frost mass is relatively insensitive to frost density, but is quite sensitive to heat transfer coefficient. This can be explained by the fact that the frost mass is basically determined by the vapor pressure difference between air and heat exchanger surface. This vapor pressure difference is not significantly affected by the frost density. On the other hand depending on the heat transfer coefficient, the surface temperature will be hotter or colder thereby affecting the driving potential for mass transfer. Frost thickness, however is significantly affected by frost density because for a given frost

mass (removed from air), a higher frost density gives lower frost thickness and vice versa. The model is not sensitive to variation in Lewis number or frost conductivity. It has been suggested in the literature that the Lewis number varies from 0.95 to 1.1 and the sensitivity study shows that the results of the model are not significantly affected by that variation. Thus we can safely assume that during frost growth, the Lewis number remains unity.

Table 4.1: Results (RMSE) of Sensitivity Study for $T_{ref} = -17.8^0C$

Variable	% Pertubation	Frost Thickness	Frost Mass
h	+10%	6.5%	5.3%
	−10%	7.5%	6.1%
ρ_f	+10%	7.0%	1.6%
	−10%	7.1%	1.7%
Le	+10%	2.5%	2.0%
	−10%	2.8%	1.8%
k_f	+10%	0.85%	0.6%
	−10%	0.82%	0.8%

4.7 Model Validation - Fin and Tube

The fin and tube coil used to test the implementation of the model is a 0.9 m^2 (0.3 m × 0.3 m) coil with louvered fins. Table 4.2 lists the important geometrical parameters of the coil. Ethylene glycol solution (50% by vol.) is used as refrigerant in this study. Iu (2007) presented the heat transfer correlation for the type of fin used in this work in the following dimensionless form

$$Nu = n_1 \left(x^+\right)^{n_2} \left(\frac{P_f}{P_{f,ref}}\right)^{n_3} \tag{4.33}$$

Where the pseudo-entrance length x^+ is given by

$$x^+ = \frac{N_r P_r / D_h}{Re_{D_h} Pr} \tag{4.34}$$

Table 4.2: Geometry and Related Parameters for the Test Fin-Tube Coil

Coil Parameter	*Value*
Finned Length	304.8 mm
Coil Height	304.8 mm
Coil Depth	21.9 mm
Fin Density	631 fins/m
Tube Pitch	25.4 mm
Number of Tubes/circuits	12/12
Number of Tube rows	1

The model presented here is driven by entering air and refrigerant conditions. While a full scale study involves many parameters, only three variables are analyzed in this study, viz. refrigerant inlet temperature (-17.8^{0}C, -22.8^{0}C, -25.6^{0}C), air mass flow rate (0.07 m^3/s, 0.09 m^3/s, 0.13 m^3/s) and air relative humidity (72%, 82%, 92%). Inlet air dry bulb temperature is held constant for all cases at 1.70C. The range of variables is selected such that it covers the normal operating conditions present in the outdoor coil of a residential heat pump in winter conditions. Frost thickness results are validated using measurements obtained from experiments discussed in 3. While the simulation was found to capture the phenomenon fairly well, it was not unconditionally stable. The pressure equalization algorithm introduced instability in the solution when the flow channel becomes narrow. This is because of the high Reynolds number situation occurring at narrow flow pathways thereby introducing instability in friction factor correlation. The instabilities occurring in the simulation are damped by constraining the variables appropriately, and the results shown in the following sections include constrained values.

4.7.1 Effect of Air Redistribution

The heat exchanger is simulated with four segments per tube in order to understand the effect of air redistribution due to frosting. The coil considered in this study is a 12-tube coil with each tube having its own inlet and outlet. The entering refrigerant conditions are assumed to be identical for each tube. The air entering temperature and relative humidity are also identical for each tube; however, the flow rate through each segment is allowed to vary. Corresponding segments in different tubes frost at the same rate due to identical boundary conditions.

Simulated and measured frost thickness for each consecutive segment of a tube is shown in Figure 4.7 for the 0.09 m^3/s air flow case with a refrigerant inlet temperature of -17.8^{0}C and air relative humidity of 82%. The volumetric flow rate is held constant for both the measured and predicted results. Frost thickness is presented in dimensionless form using fin spacing as the non-dimensionalizing parameter.

It can be seen from the figure that at any time during the frost growth the thickness of the frost layer varies considerably from tube inlet to outlet. Measured frost thickness at each segment matches the simulated results well. As the first segment in the tube is completely frosted (dimensionless frost thickness equal to 1), the rate of frost growth in the remaining segments increases sharply. As the first segment frosts over, the heat transfer predicted by the model for that segment drops to zero. As a result, the entering refrigerant temperature to the remaining segments is lower. This results in a sharp increase in the frost growth rate for the remaining segments as shown in the Figure 4.7. It can be readily understood from the figure that non-uniform frost thickness results in a significant difference in airflow through each segment. Both measured and predicted velocities showed that air redistribution resulted in a 20% increase in air flow rate through the fourth segment. Using a

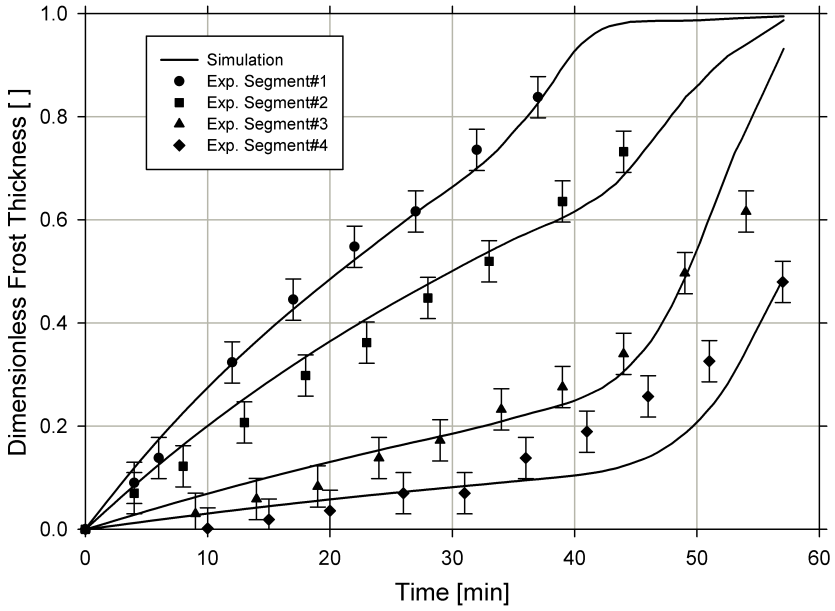

Figure 4.7: Comparison of Measured and Simulated Frost Thickness at Different Segments (0.09 m^3/s, -22.8^{0}C, 82%RH)

smaller air flow rate through the segment will result in under predicting the segment capacity. Similar results are obtained for other test cases.

Predicted frost growth in different segments of the coil with and without the air redistribution algorithm is shown in Figure 4.8. Initially, both models predict similar results. Frost thickness calculated in the first two segments without considering air redistribution is higher initially compared to the values obtained by considering redistribution. As frost grows, the air flow rate drops in the (refrigerant side) upstream segments causing a drop in surface temperature and an increase in the rate of frost growth in the downstream segments. The error between the measured values and the 'no air redistribution' simulation results illustrates the importance of modeling air redistribution for cases where the frost grows non-uniformly over the face of the coil due to either a high refrigerant side temperature difference or non-uniform air flow through the coil.

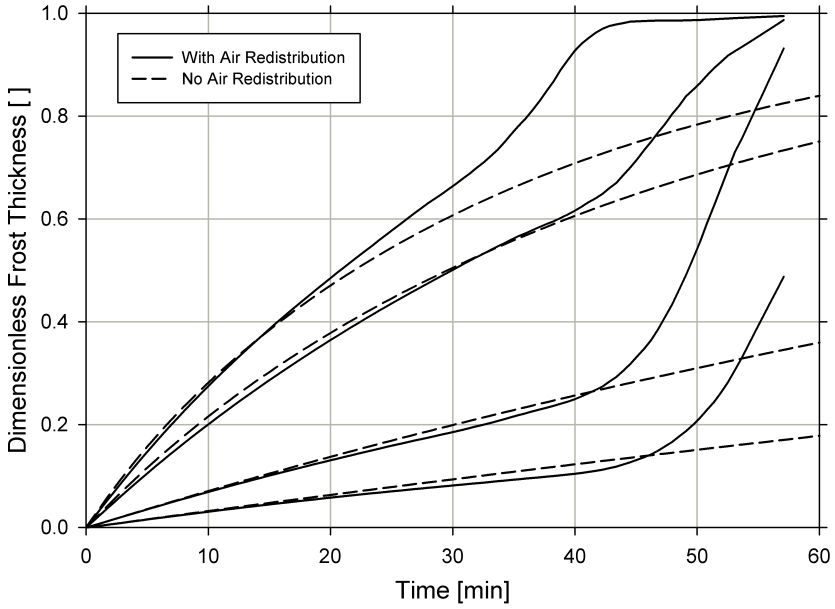

Figure 4.8: Calculated Frost Thickness with and without Airflow Redistribution (0.09 m^3/s, -22.8^{0}C, 82%RH)

4.7.2 Effect of Air Flow Rate

Air flow rates selected for the study are such that the approaching velocity to the coil falls within the typical range of heat pump outdoor coils. Figure 4.9 shows the simulated and measured frost thickness at three different air flow rates. The experimental results show that the rate of frost growth is not significantly affected by the air flow rate. Lower flow rates (lower face velocity) result in lower surface temperatures. As a result the rate of frost growth is slightly higher when the flow rates are low.

The experimental results also show a delay in the initiation of frosting at lower flow rates. The model does not predict this delay. The delay phenomena, is also seen in experimental measurements for varying relative humidity and entering refrigerant temperatures as discussed in the following sections.

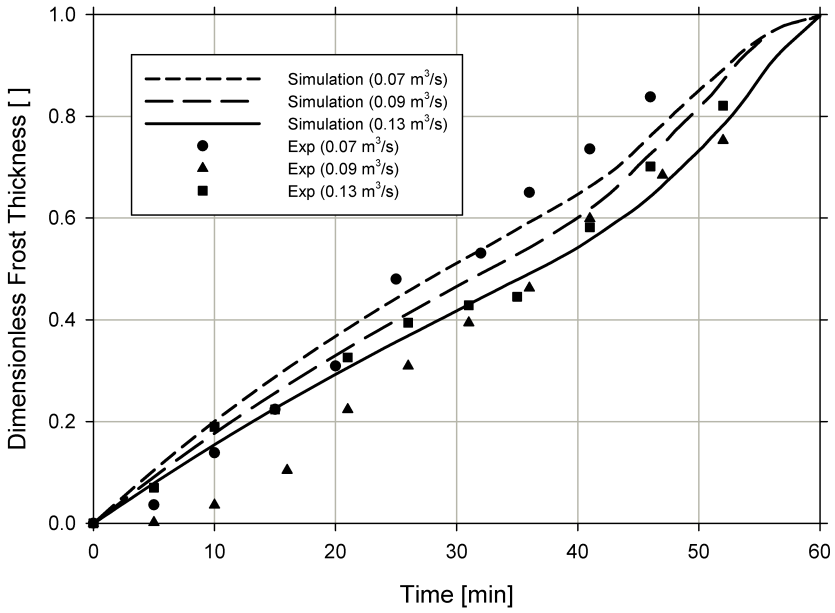

Figure 4.9: Frost Thickness at First Segment for Different Air Flow Rates (-17.8^{0}C Ref in, 82% RH)

4.8 Effect of Air Relative Humidity

A difference in vapor partial pressure between the air stream and the air inside the frost layer is the driving force for the mass transfer phenomenon in frost growth. A low humidity of 72%, a baseline humidity of 82% (ARI, 2008) and a high humidity of 92% are considered in this study. Measured and simulated frost thickness values are presented in Figure 4.10.

Both simulation and measurements show an increase in frost growth rate with humidity ratio. However, the simulation over predicts the frost thickness for all three cases as shown in the figure. This is primarily due to the delay in the onset of frosting shown in the experimental results. As shown, the slopes of the simulation curves approximate the slopes of the measured data curves reasonably well. Thus the experimental results match the rate of frost growth predicted by the model once the frost has initiated. The delay in frost initiation seen in experimental

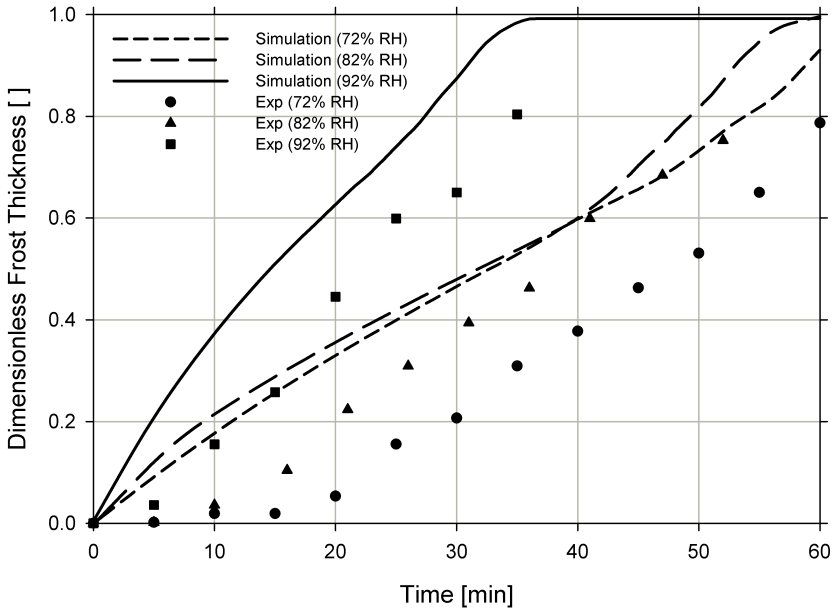

Figure 4.10: Frost Thickness at First Segment for Different Air Entering Relative Humidity (0.09 m^3/s, -17.8^{0}C Ref in)

measurements is due to the fact that in fin-tube coils, frost starts at the tube and moves towards leading edge of fin. Thickness measurements however can be done only when the frost is visible at the leading edge. Model on the other hand in it's current version assumes a uniform temperature across the depth of the coil and thus predicts frost initiation as soon as the frosting period starts. In order to effectively capture this delay in the initial stages a discretization scheme is required in the depth of fin. The effect of a discretized fin model on initial frost growth is discussed in 4.11.

4.9 Effect of Refrigerant Inlet Temperature

To study the effect of entering refrigerant temperature, three different cases are considered. Since the refrigerant used in the experiments (Ethylene glycol solution) is a high viscosity fluid, the model predicts that the flow will not be thermally

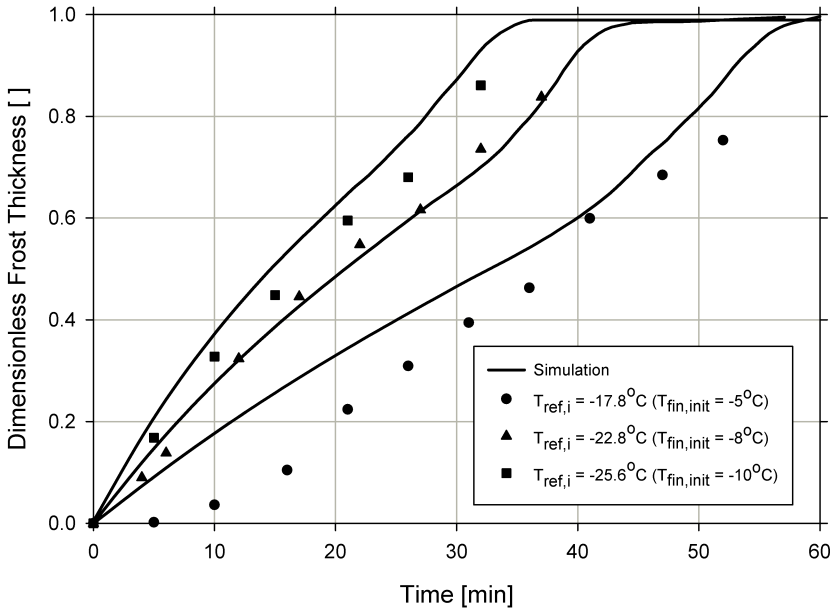

Figure 4.11: Frost Thickness at First Segment for different Entering Glycol Temperature (0.09 m^3/s, 82% RH)

developed anywhere in the tubes of the coil. As a result, the model predicts that the internal heat transfer coefficient will vary significantly resulting in different surface temperatures for each segment. Figure 4.11 shows the variation in the first segment frost thickness for different glycol entering temperature (different initial fin temperature).

It can be seen from the figure that lower refrigerant temperatures result in higher frost growth rates. Model results match experimental measurements for the higher frost growth cases. The model assumes that the nucleation period is negligible compared to the overall frosting period. However, the disagreement between the measured and simulated values for the high temperature case indicates that at higher temperatures the onset of nucleation is delayed. When temperatures are lower, the frost reaches the leading edge of fin rapidly and thus enables measurement of thickness. For high temperature case it takes more time for the

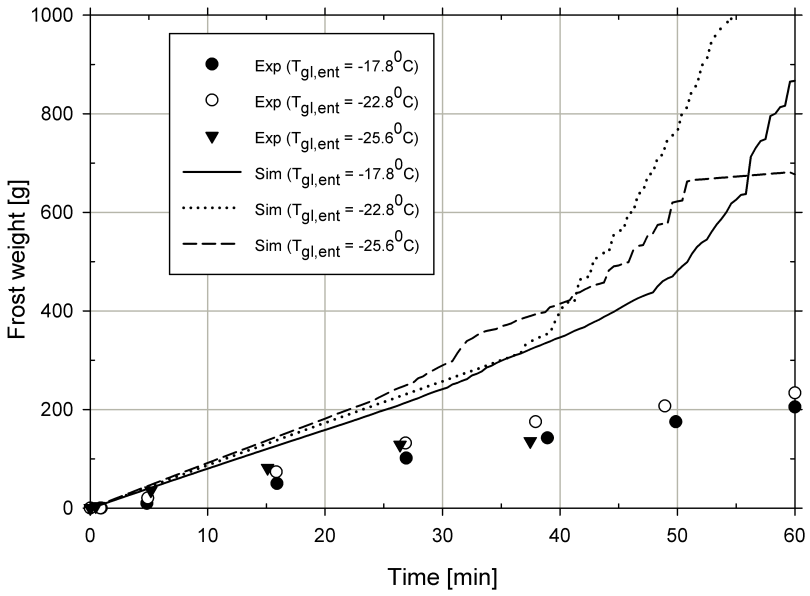

Figure 4.12: Total Mass Accumulation on the Coil for different Entering Glycol Temperatures (0.09 m^3/s, 82% RH)

frost to reach leading edge and thus the discrepancy between experimental and simulated frost thickness in the initial stages.

Total frost mass accumulated on the coil for different inlet temperature cases is shown in Figure 4.12.

In its present form the model also assumes a uniform frost thickness over the entire depth of the fin. Experimental observation showed that frost deposition was primarily on the face of the coil with practically no frost deposition on the back portion of the coil. Although the model clearly requires a thickness profile or discretized fin depth in order to accurately predict frost mass near the end of the frosting period, the simulation results do show an interesting but counter-intuitive trend in the frost mass accumulation. While the lowest temperature case is expected to produce highest frost mass, it is seen that the total mass accumulated for -25.6^{0}C case is lower than the other two cases. The low temperature curve crosses over the

other two curves. The experimental data also shows the low temperature curve 'cross over', though the effect is much less pronounced in the experimental data. The 'cross-over' effect is explained by the fact that the frost accumulated at lower temperatures is less dense [Eq (4.19)]. A fluffy frost is produced at low temperatures resulting in a thicker frost layer. Thicker fluffy frost covers the face of the coil faster which results in a shorter frosting cycle causing low mass of frost accumulation.

4.10 Model Validation - Microchannel

The work related to modeling the frost growth on microchannel heat exchangers has been very limited. In microchannel heat exchangers used as outdoor coils, the frost growth can be highly non-uniform (Kim and Groll, 2003; Padhmanabhan et al., 2008) due to the variations of the local surface temperature caused mainly due to maldistribution of refrigerant and higher temperature differences from tube inlet to tube outlet. The microchannel coil used to test the implementation and validate the model is a 0.9 m^2 (0.3 m $\times$ 0.3 m) coil with louvered folded fins. Table 4.3 lists the important geometrical parameters of the coil. Ethylene glycol solution (50% by vol.) is used as refrigerant in this study. The segment by segment heat exchanger simulation uses five segments per tube in the direction of glycol flow i.e. from the bottom to the top of the heat exchanger. Heat transfer correlation [Eq (4.35)] suggested by Kim and Bullard (2002) is used to determine the air side heat transfer coefficient. For the case of microchannel the total air flow rate on the face of the coil is allowed to drop as the frost grows. The air flow rate on the face of the coil is imposed as a time dependent boundary condition in the form of a correlation

empirically generated from experiments.

$$j = Re_{Lp}^{-0.487} \left(\frac{L_\alpha}{90}\right)^{0.257} \left(\frac{F_p}{L_p}\right)^{-0.13} \left(\frac{H}{L_p}\right)^{-0.29} \left(\frac{F_d}{L_p}\right)^{-0.235} \left(\frac{L_l}{L_p}\right)^{0.68} \left(\frac{T_p}{L_p}\right)^{-0.279} \left(\frac{\delta_{fi}}{L_p}\right)^{-0.05} \tag{4.35}$$

Table 4.3: Geometry and Related Parameters for the Test Microchannel Coil

Microchannel Coil Parameter	Value
Coil Face Area (L x W) [m^2]	0.093 (0.3048 x 0.3048)
Tube Orientation	Vertical
Single Tube Length [mm]	304.8
Tube Depth [mm]	25.4
Tube Height [mm]	1.75
Tube Spacing [mm]	9.32
Fin Pitch [fins/m]	787
Fin Thickness [mm]	0.095
Tube/ Fin material	Aluminum/ Aluminum
Number of ports/Geometry	4/Rectangular

The frost model developed are validated for three different temperatures (-12.2^{o}C, -9.4^{o}C, -6.7^{o}C). Various parameters such as frost thickness, frost surface temperature and coil capacity are investigated. The boundary conditions for the simulation are the temperatures and flow rates of air and glycol. While the air and fluid temperatures and ethylene glycol flow rate remain constant, the total air flow rate across the coil varies. The air flow boundary condition is obtained from the experiments discussed in 3.8. Air Flow rate for all cases at the start of the frosting cycle is 0.09 m^3/s and the frosting period is considered to be finished when the total air flow rate drops below 0.07m^3/s. It is well established that the frost growth is not related to the fluid temperature but is dependent on the surface temperature. The surface temperatures change as frost grows. On the other hand, the fluid entering temperatures (refrigerant and air) are constant and well defined throughout the

frosting process. Thus, for clarity in plots and for consistency during the comparison with the actual operating parameters of the outdoor coils, the glycol entering temperature and air approaching temperature are chosen as parameters. Fin surface temperature is a derived variable from the heat and mass balance equations. The results are presented in non-dimensional form whenever such a presentation is reasonable.

Frost thickness at different times for different fluid entering temperatures is shown in Figure 4.13. The values are normalized based on the half fin spacing. Thickness values obtained from experiments are also plotted in the figure. During microchannel experiments, the frost thickness measurements are taken at a fixed location. The location where the videoscope was placed corresponded to segment 2 of the simulations. The simulation results shown are thus for segment 2. Measured thickness matched simulated results very well. The frost thickness on the microchannel for all the three cases was similar at the end of the test. This is as expected since the frost growth is terminated when the air flow rate drops to a 25% of initial value (dry coil). Since the fan curve is constant for all the three cases the final frost thickness is expected to be approximately same. The model currently assumes uniform frost distribution through the depth of the coil which is not the case in real life applications. It needs to be understood that in real conditions lower temperatures cause the frost to be deposited at a significantly higher rate on the front face of the coil thereby resulting in an orifice like condition which causes higher pressure drop. The effect of such a geometry change is not known. The model does not currently take into account this variation in geometry.

The effect of relative humidity on the frost thickness is shown in Figure 4.14. The figure shows the simulated and experimental values of frost thickness. It can be seen that the model predicts the frost thickness within 1% for the medium RH (82%)

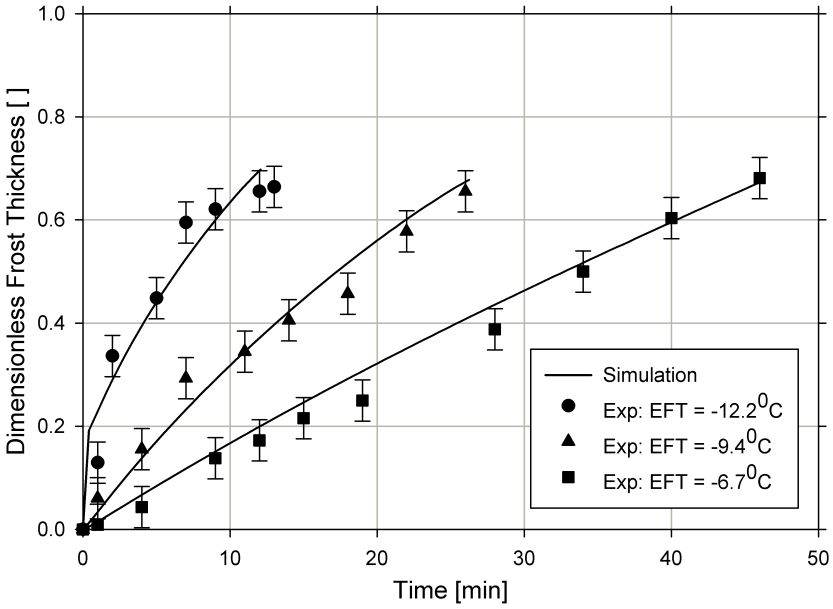

Figure 4.13: Experimental and Simulated Frost Thickness in Microchannel Coil for Different Entering Glycol Temperatures

case and within 3% for high RH (92%) case. However for the low RH (72%) case the error between simulated and experimental value for frost thickness varied from 2% at initial stages to 30% towards the end of the test. Similar error was observed in fin-tube heat exchanger also for low humidity case. This discrepancy in simulated and measured values suggests that at low humidities, the assumption that moisture is instantly moved from air to the heat exchanger surface may not be valid. Further investigation is required to understand the actual mechanism operational at low humidity cases.

The mass of frost accumulated on the heat exchanger surface for different entering fluid temperatures is shown in Figure 4.15. As seen in a fin and tube heat exchanger the frost growth model over-predicts the total accumulated frost mass for a microchannel heat exchanger also. For all temperature cases the accumulated frost mass predicted by the model is more than 2 times that of experimentally measured values. Consistent over-prediction in frost mass warrants an improved model in

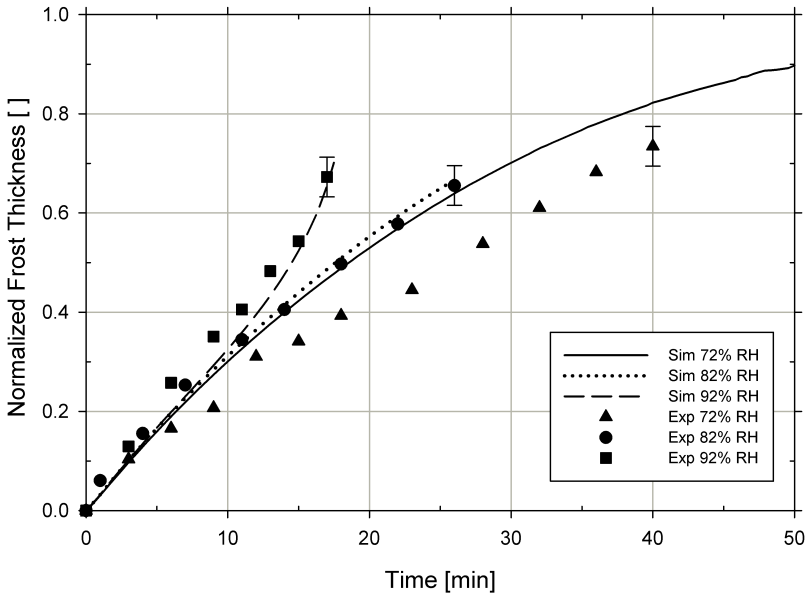

Figure 4.14: Experimental and Simulated Frost Thickness in Microchannel Coil for Different Entering Air RH

which the frost thickness varies in the direction of air flow.

Figure 4.16 shows the frost surface temperature obtained from the simulations for the three different entering temperature cases. The sharp increase in frost surface temperature and frost thickness for the low temperature case suggests that in such conditions the fin spacing is quickly covered by low density (fluffy) frost which blocks the airflow. At the end of cycle, the weight of frost deposited on low temperature surfaces will be less than the weight of frost deposited on high temperature surfaces. The variation of frost surface temperature is significantly less for the highest temperature case.

Air redistribution that occurs on the face of the heat exchanger is one of the most important aspects of this study. Figure 4.17 shows the frost thickness for 5 different segments for -9.4^{o}C inlet fluid temperature case. The frost grows faster in segments near the inlet header (upstream) compared to later segments (downstream). Figure 4.18 shows the variation of air flow through each segment presented as a

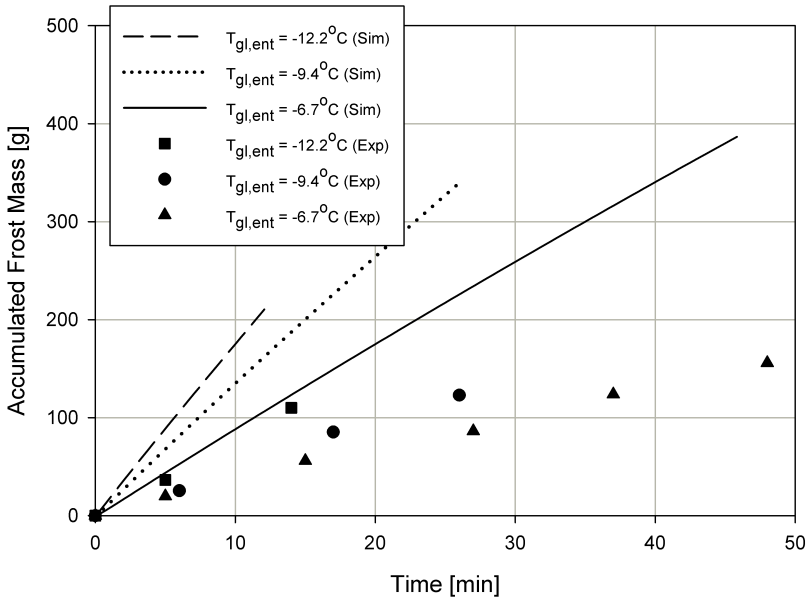

Figure 4.15: Experimental and Simulated Frost Mass for Different Entering Glycol Temperatures

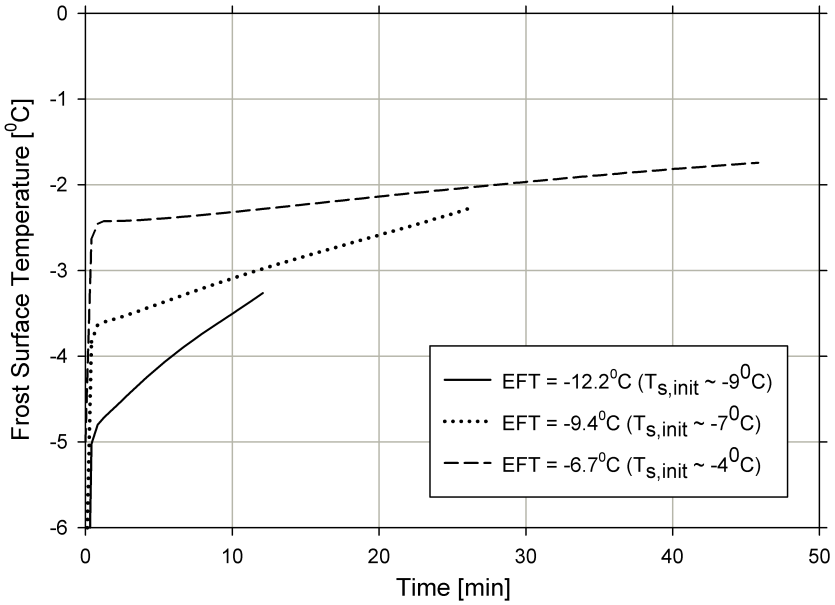

Figure 4.16: Frost Surface Temperature at First Segment for Different Entering Glycol Temperatures (Approx. Initial Fin Temperatures shown in parenthesis)

normalized mass flux. Mass flux through each segment at any time is divided by the initial mass flux through that segment to obtain the normalized parameter. It can be seen from the figure that the mass flux through the segments varies continuously throughout the frosting period. While the mass flux decreases for segments with thicker frost (segments 1 & 2), the flow redistributes itself to less thick (low resistance) segments (segments 4 & 5). It is important to capture this redistribution of the air flow because in actual heat pump units microchannels are sized as condensers and will be oversized when used as evaporators in winter. The non-uniformity in frost growth in microchannels used as out door coils in heat pumps is confirmed in literature (Kim and Groll, 2003; Padhmanabhan et al., 2008). Ignoring the air redistribution phenomenon and non-uniformity in frost growth will result in under predicting the coil capacity.

As the frost grows the coil capacity drops due to decreased air flow rate across the coil and increased resistance to heat transfer due to the low conductivity of the frost layer. Figure 4.19 shows this drop in capacity for the coil as frost grows. The capacity is presented in dimensionless form using the initial capacity in each case as the normalizing parameter. Capacity degradation in microchannel heat exchangers is fast and almost linear through out the frosting period. This drop in capacity is shown in Figure 4.19 and it is in agreement with the findings of Shao et al. (2010). If the refrigerant temperature is at -12^{o}C, it takes only 10 minutes to drop the heat transfer rate by 30%. If the glycol temperature is warmer at about -6.7^{o}C, similar heat transfer degradation takes approximately 45 minutes.

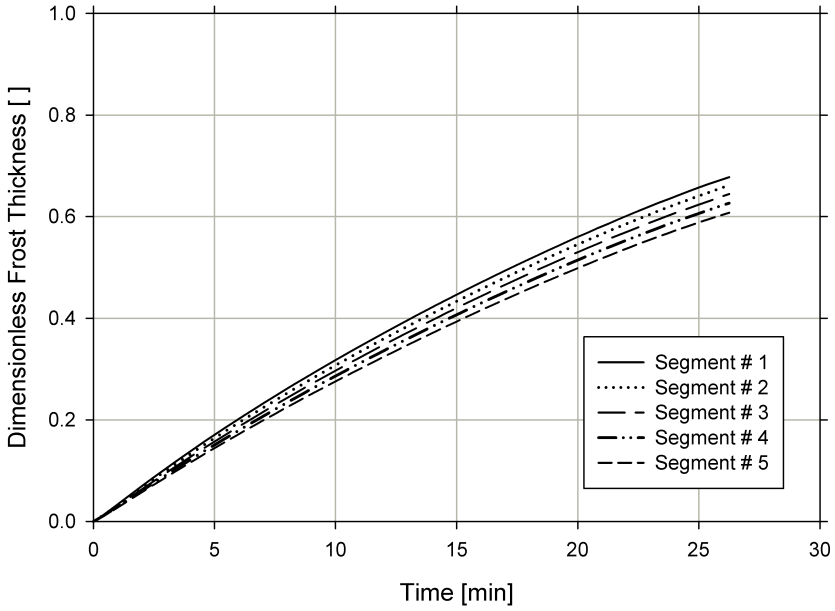

Figure 4.17: Rate of Frost Growth at Different Segments (-9.4^{0}C EFT, 82% RH and Initial Air Flow Rate of 0.09 m^3/s)

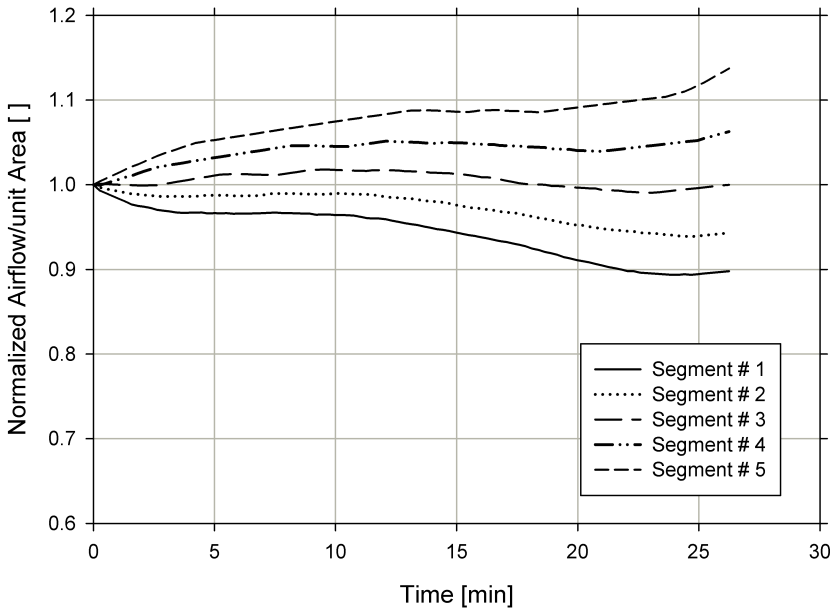

Figure 4.18: Normalized Mass Flux through various Segments

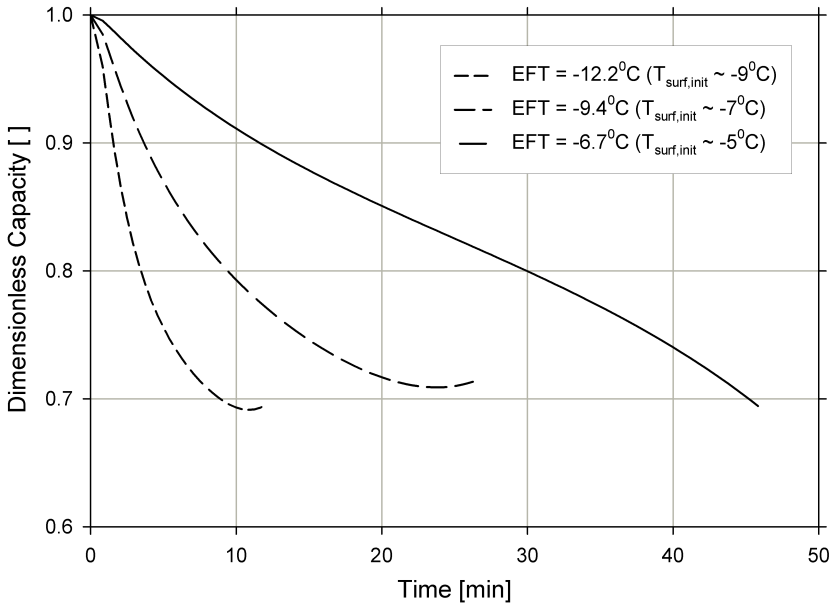

Figure 4.19: Normalized capacity of the Heat Exchanger during Frosting for Different Entering Glycol Temperatures (Approximate Initial Fin Temperatures shown in parenthesis)

4.11 Improvements to the Frost Model - Application to Fin and Tube Coil

The frost growth model discussed in previous sections assumes a single representative surface temperature for the whole fin and tube for any given segment. Assuming a uniform surface temperature will result in uniform frost thickness all over the segment thereby resulting in over predicting frost thickness at initial stages. For a fin-tube coil in frosting conditions, the coldest part is the tube surface and thus frost starts at tube surface. As time progresses, the frost layer moves outward towards the fin tip. Under some conditions this time lag can be significant which when neglected will grossly overestimate the effect of frost growth on the heat exchanger performance. The time taken for the frost to start growing at the fin tip depends on various factors such as the temperature differential between air and refrigerant, internal heat transfer coefficient and fin geometry and fin tube contact

resistance. Depending on the fin base temperature, it is possible that the fin near the tip is above the temperature for the frost to form. In such cases accounting for the frost initiation delay at the leading edge is an important factor to consider especially for an air side pressure drop calculations. The discrepancy in frost thickness for fin-tube is more pronounced at higher temperatures. This is due to the fact that at colder temperatures, the time difference between when the frost starts at the tube surface and at the leading edge is small.

The humidity ratio of the air drops as it passes through a part of heat exchanger where frost grows. Thus the thickness of frost varies in the direction of airflow. This variation in frost thickness results in over prediction of frost weight during the entire frosting period. This error in predicting frost weight occurs for both fin-tube and microchannel heat exchangers. Discrepancy in predicting frost weight by assuming a uniform frost thickness is seen in results presented in the previous section (Fig.4.12). Frost weight showed significant difference from experimental results for all test cases.

Discretizing the fin/tube into multiple node points in the direction of air flow will allow the current frost model to predict a varying frost thickness profile in the direction of air flow. With this improvement, the frost model along with the heat exchanger model allows us to determine the varying frost thickness profile in both refrigerant direction and air flow direction. In order to improve the model to account for varying frost thickness in the air flow direction a finite volume discretization based on actual heat balance approach (Patankar, 1980) is employed. Such a formulation enforces conservation of energy in each control volume.

Consider a segment of heat exchanger with depth P_l and a tube diameter of D_{tube}. In order to study the variation in frost profile through the depth of the coil, we divide the fin sections upstream and downstream of the tube into n grid points with front and back of the tube having separate grid points. Thus the number of grid

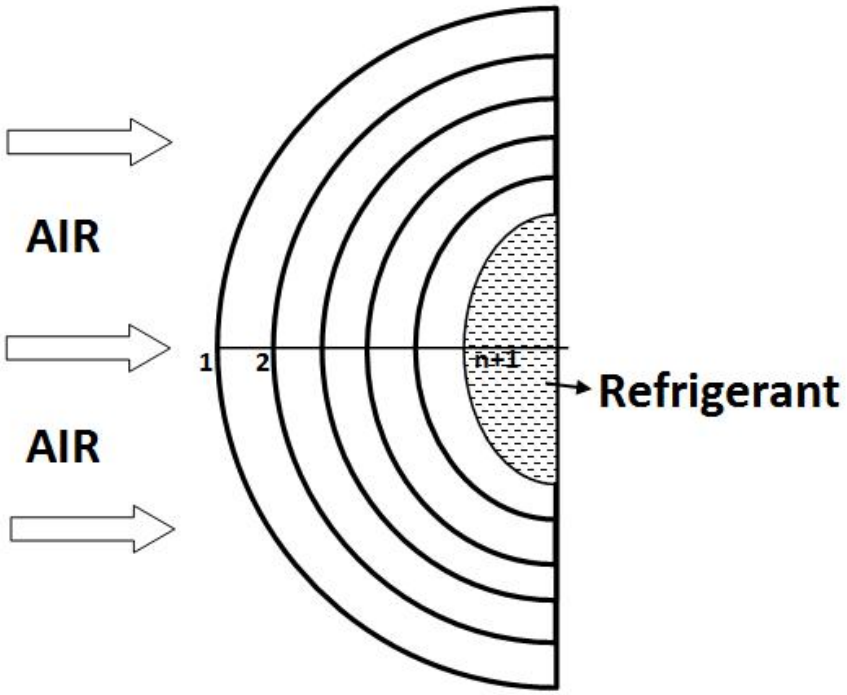

Figure 4.20: Schematic of upstream half of heat exchanger showing control volume and locations of node points.

points in each half of the heat exchanger in the direction of air flow is given as

$$N = n + 1$$

A node is placed at the center of each internal grid and one node each is placed at the tube surface and at the fin leading edge. Figure 4.20 shows the upstream half of the heat exchanger (fin leading edge to tube) with the control volume and placement of node points. Control volumes are drawn around each node point, with the first and last node surrounded by half-grid spacing.

The frost model as described in previous section, utilizes an energy balance at the fin/tube surface as the final equation to close the system of equations. In its simple form the fin/tube surface energy balance is formulated to equalize the total heat transferred from air (sensible and latent) to frost layer and the total heat removed

by refrigerant in that segment. Thus the simple energy balance can be written as in Eq (4.36). Solution of the equation along with the frost model provides one surface temperature for the entire segment.

$$[h(T_\infty - T_{fs}) + h_m(\rho_\infty - \rho_{fs})h_{sg}]A_o = h_i(T_{surf} - T_r)A_i \tag{4.36}$$

In the improved version of the model, an energy balance is established in each control volume (shown in Fig 4.20) of the fin by equalizing heat transferred from the air to the net heat conduction through the control volume interfaces. Conduction heat transfer occurring through the fin to the tube is radial, while the heat transferred from air to the frost/fin layer is treated as an internal heat generation term. In order to account for variation in frost thickness profile, the frost model needs to be solved for each control volume separately with varying fin surface temperature in the direction of airflow. No iteration was required on the fin surface temperature in the simple frost growth model since the whole segment was assumed to be at one temperature. With the introduction of discretization the temperature of the fin surface at any node is dependent on the neighboring node points. Thus an iterative scheme is required in order to obtain converged temperatures for each node. For any given time step, solution is initiated by assuming the fin temperature profile from the previous time step. To make the whole solution scheme computationally efficient, the frost growth equations and the fin discretization equations are decoupled. At each time step, the frost thickness and frost surface temperature from the last time step is used in the fin discretization equations. The temperatures at each fin node are then calculated and are used in solving the frost layer equations.

In formulating the discretization equations, it is assumed that no heat is transferred through the fin tip. The formulation shown here is for the upstream half of the heat exchanger; similar equations are developed for the downstream half also. The heat

balance equation for a control volume in the fin surface depends where it is located. For the tube node the total heat absorbed by the refrigerant is equal to the sum of the heat transferred from the air to the bare tube (through the frost layer on the tube) and the heat conducted from the fin. The control volumes can be divided into four distinct cases

- Control volume # 1 (CV_1) consists of the node located at the leading edge of the fin - This is the first control volume that comes in contact to air flow. We assume no heat is transferred through the fin tip. The energy balance for this control volume contains two terms, viz., Heat conducted through the fin to adjacent node downstream and heat transferred from air to the control volume through frost layer (treated as internal heat generation). The Heat balance formulation for this control volume can be written as:

$$[h(T_\infty - T_{fs}) + h_m(\rho_\infty - \rho_{fs})h_{sg}]A_g = \frac{\pi k_{fi}\delta_{fi}(T_i - T_{i+1})}{\ln(D_1/D_2)}$$

- Control volume # 2 (CV_2) consists of one half of the tube - Whole of tube is represented as a single node. This control volume needs a little explanation for clarity. The control volume consists of two parallel heat transfer paths, viz., A first path of conduction through the finned region of the tube and subsequent convection to the refrigerant and a second path consisting of convection alone through the non-finned region of the tube to the refrigerant. The convective heat transfer to the refrigerant through the finned and non-finned portions can be grouped as total refrigerant heat transfer. The heat balance of this control volume is a little complicated and is written as follows (note the node number for tube node is $n+1$):

$$[h(T_\infty - T_{fs}) + h_m(\rho_\infty - \rho_{fs})h_{sg}]A_g + \frac{\pi k_{fi}\delta_{fi}(T_n - T_{n+1})}{\ln(D_n/D_{n+1})} = h_i A_i(T_{n+1} - T_{r,avg})$$

- Control volume # 3 (CV_3) consists of the node on adjacent to the tube node but located on the fin. This control volume has three terms in the energy balance, viz., Heat transferred to the control volume through the upstream node, heat transferred to the tube node through the fin and heat transferred to the control volume from the air (treated as internal heat generation). The heat balance for this control volume is written as follows:

$$[h(T_\infty - T_{fs}) + h_m(\rho_\infty - \rho_{fs})h_{sg}]A_g + \frac{\pi k_{fi}\delta_{fi}(T_{n-1} - T_n)}{\ln(D_{n-1}/D_n)} = \frac{\pi k_{fi}\delta_{fi}(T_n - T_{n+1})}{\ln(D_n/D_{n+1})}$$

- All other control volumes located in the fin not accounted by above cases (CV_4). Energy balance for this control volume is similar to the CV_3, except that the node numbers now will be internal node points. The heat balance is written as follows:

$$[h(T_\infty - T_{fs}) + h_m(\rho_\infty - \rho_{fs})h_{sg}]A_g + \frac{\pi k_{fi}\delta_{fi}(T_{i-1} - T_i)}{\ln(D_{i-1}/D_i)} = \frac{\pi k_{fi}\delta_{fi}(T_i - T_{i+1})}{\ln(D_i/D_{i+1})}$$

Where $k_{fi} =$ Fin conductivity [W/m-K]

$\delta_{fi} =$ Fin thickness [m]

$A_g =$ Grid air side area [m^2]

$T_{r,avg} =$ Average refrigerant temperature in the segment [^{0}C]

$T =$ Surface temperature [^{0}C]

$D =$ Node diameter [m]

$i =$ Node index

The above equations can be rearranged to form prescribed by Patankar (1980). The equations are then solved using a TDMA solution scheme to give the surface temperature for each node point. The boundary condition for the leading edge node is adiabatic condition. For the node at tube surface the boundary condition is

convective boundary at the refrigerant tube interface. Once the fin temperatures are known the outlet air conditions are updated for each control volume. The conditions of air leaving a control volume (entering a downstream control volume) are given by Eq (4.37).

$$T_{a,i+1} = T_{a,i} - \frac{h\Delta T_{i,\infty} A_g}{\dot{m}_a c_{p,a}} \tag{4.37a}$$

$$\omega_{a,i+1} = \omega_{a,i} - \frac{h_m \Delta \rho_{i,\infty} A_g}{\dot{m}_a} \tag{4.37b}$$

Where $T_a =$ Air temperature [^{0}C]

$\omega_a =$ Air humidity ratio []

$i =$ Grid index

Once entering conditions for all nodes are solved, outlet air conditions of the segment are determined. With the newly updated air conditions at each node new surface temperature are calculated and the process repeated. Newly determined air outlet conditions are compared to previous values to determine convergence. The solution scheme is demonstrated in Algorithm 1.

With the proposed improvement to the model, the entire frost model will consist of 3 nested loops. The three loops in the order of inner loop to outer loop are

1. Simulate frost model for each node in any given segment.
    - Estimate the surface temperatures for each node point
    - Solve the frost equations with estimated surface temperature as boundary condition
2. Simulate the frost model for each heat exchanger segment in the direction of refrigerant flow.
3. Redistribute the air flow across the face of the coil to equalize the pressure.

```
for iter = 1 to maxiter do
    for Grid = 1 to N do
        Update entering air conditions
        Initialize Frost variables for current time step
        Solve Frost Equations with applicable fin energy balance
        Update Frost Variables
        Update exiting air conditions
    end
    Calculate difference in outlet conditions from previous iteration
    if ΔT_{a,o} < T_conv & Δω_{a,o} < ω_conv then
        Exit Iteration
    end
end
```

Algorithm 1: Algorithm for Detailed Frost Model Solution with Fin Depth Discretization

The heat exchanger model and frost model is decoupled with quasi steady state assumption. At any time step, the heat exchanger model is run to get refrigerant temperatures at each segments and an approximate fin temperature distribution. Refrigerant temperatures thus calculated are kept constant for the frost model calculation. After the frost model calculations are performed, the values of frost thickness, and frost conductivity for each segment are passed back to the heat exchanger calculations in the next time step. Along with the heat exchanger model, the whole simulation consists of four nested loops. In addition to the three loops mentioned before, the fourth loop is a time step loop. The time step loop allows the model to determine the defrost initiation based on a particular defrost criterion. Overall quasi-steady state solution algorithm for a heat exchanger with frost growth is shown in Algorithm 2.

Improved frost growth model is run for the three different temperature cases. It is expected that the improved model will improve the prediction for the warm temperature case and also the weight predictions for all the cases. Another benefit of the improved frost model is the ability to predict the air stream wise variation in frost thickness. This information can be used in later studies to study to develop

```
repeat
    Solve heat exchanger model
    Obtain refrigerant temperatures in each segment
    repeat
        for n_seg = 1 to Total Num Segments do
            for iter = 1 to maxiter do
                for Grid = 1 to N do
                    Update entering air conditions
                    Initialize Frost variables for current time step
                    Solve Frost Equations with applicable fin energy balance
                    Update Frost Variables
                    Update exiting air conditions
                end
                Calculate difference in outlet conditions from previous iteration
                if ΔT_a,o < T_conv & Δω_a,o < ω_conv then
                    Exit Iteration
                end
            end
        end
        Calculate segment pressure drop
        if Pressure not equalized then
            Redistribute air flow
        end
    until Air pressure drop across segments are equal
until Defrost initiation
```

Algorithm 2: Overall Quasi-Steady Solution Algorithm for Heat Exchanger with Frost Growth

pressure drop correlations during frosting. The model is tested with 10 nodes in the direction of air flow with 4 nodes each in the upstream half and downstream half of the coil. In addition to these nodes on the fin, two additional nodes are placed one on the upstream half of the tube and one on the downstream half of the tube.

Figure 4.21 shows the stream wise frost thickness for entering glycol temperature of -17.8^0C. The figure shows the frost thickness at various node locations at different times. It can be seen that initially, as we reach closer to the tube the frost thickness increases and as we move away from tubes, frost thickness decreases. This is due to the fact that initially the farthest nodes are comparatively warmer than the nodes near the tube. As the frost grows on the inner nodes, corresponding fin surface temperature drops, thereby causing the outer node fin surface temperature also to drop. At some point, the leading edge node (Node 1) becomes cold enough to remove a significant amount of moisture. After this point the leading edge accumulates frost faster resulting in less moisture reaching inner nodes. As dry air enters the inner nodes the growth of frost at inner nodes tends to slow down. For the warm temperature case, as frost grows the air path changes from no frost finned flow to flow path with restricted throat during initial stages of the cycle and finally ending in a configuration similar to orifice flow.

Figure 4.22 and Figure 4.23 shows the frost thickness at different nodes for entering glycol temperatures of -22.8^0C and -25.6^0C respectively. Results for $T_{ref} = -22.8^0C$ case shows results similar to the warm temperature case, but the leading edge phenomenon is less visible. For the lowest temperature case the leading edge effect seen in the warm temperature case is almost non-existent. For the lowest temperature case the frost accumulates at leading edge from the start of the test itself and the inner nodes always accumulates less frost compared to leading edge.

Figure 4.24 shows the results obtained from simple and improved model along with

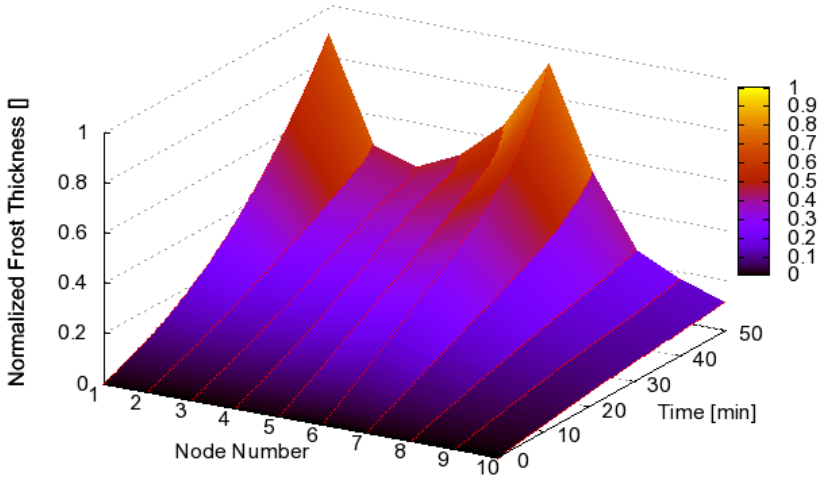

Figure 4.21: Frost Profile in the Direction of Air flow for $T_{ref} = -17.8^0C$

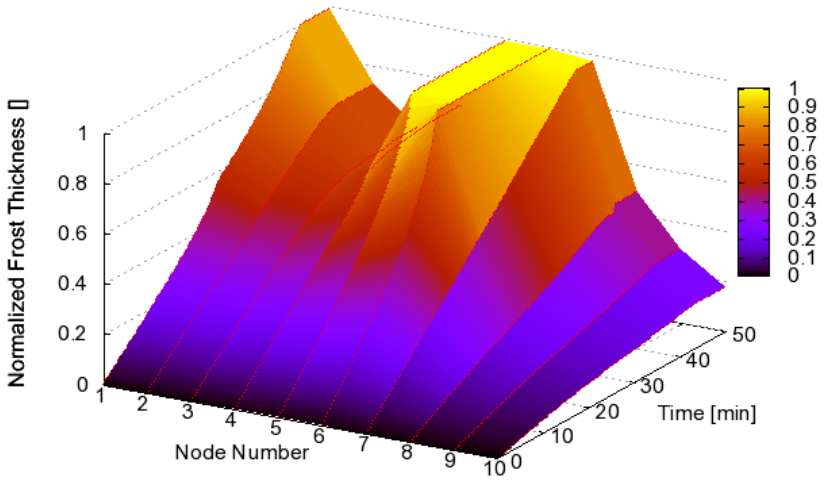

Figure 4.22: Frost Profile in the Direction of Air flow for $T_{ref} = -22.8^0C$

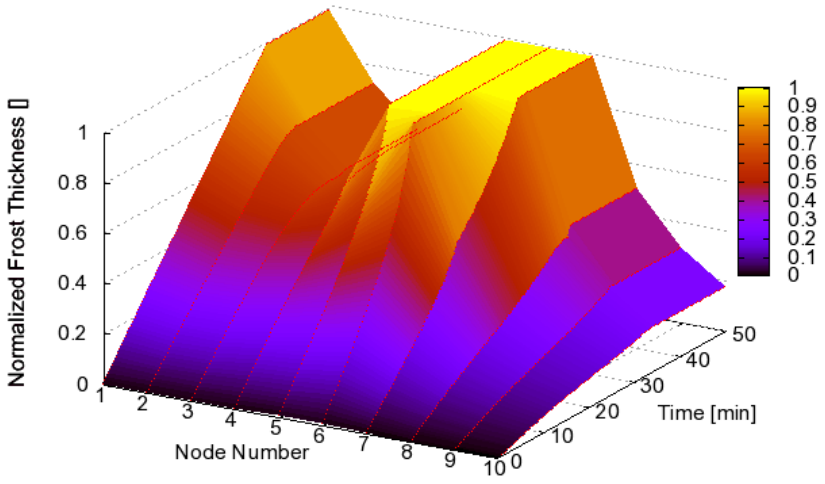

Figure 4.23: Frost Profile in the Direction of Air flow for $T_{ref} = -25.6^0C$

the experimental for all the three temperature cases. It can be seen that for warm temperature case, the improved model helped by reducing the initial frost accumulation at leading edge. Even though the improved model was not able to predict the non-initiation of frost seen in experiments, the results obtained from the improved model are within uncertainty of the measured values during initial stages. The improved model did not affect the low temperature cases significantly, though improved model predicted slightly lower frost thickness. However this was expected since the simple model used a representative surface temperature which is lower than the actual leading edge temperature.

Figure 4.25 shows the comparison of total frost accumulation obtained from experiments to the results predicted by the simple (Fig 4.25a)and the improved model (Fig 4.25b). It can be seen that the improved model predicts the frost weight better than the simple model. The varying frost thickness through the depth of the coil is a significant factor in weight calculations for the improved model which the simple model lacked. The model also captures the flattening of the weight curve for

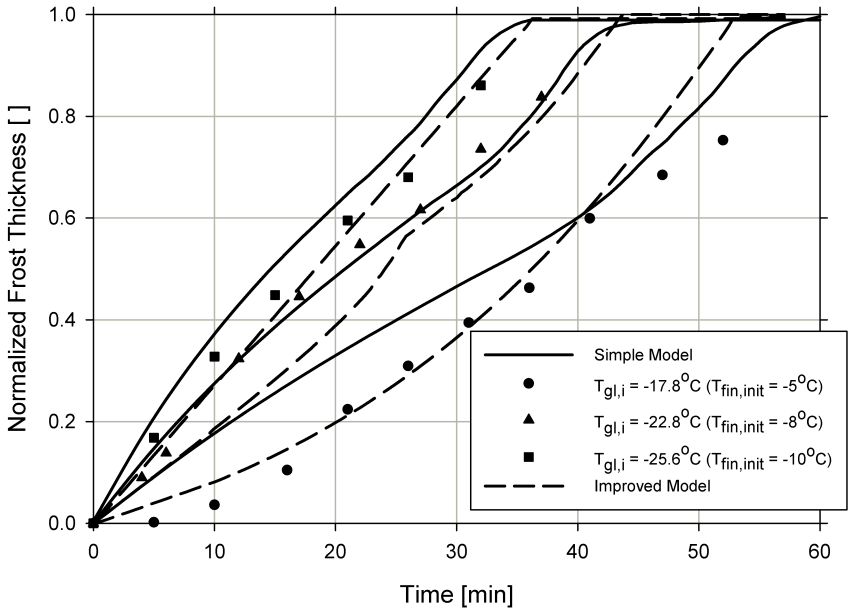

Figure 4.24: Frost Thickness from the Simple and Improved Frost Model

low temperature case. This is true due to the fact that as any segment in the coil is blocked (normalized frost thickness equals unity), the model ignores that segment for further frost calculations. This causes no further frost accumulation for such segments. For low temperature case most of the segments is blocked towards the end of the cycle and thus there is no significant real estate for the frost to grow, thereby causing the weight to remain steady.

4.12 Conclusions - Fin and Tube

A mathematical model based on a scaling approach for predicting the frost growth is presented. The frost model is implemented in a segment-by-segment heat exchanger routine along with a pressure equalization algorithm to account for air redistribution effects. The effect of non-uniform frost growth on the face of the coil is studied. It was observed that in conditions where the surface temperature of the coil varies significantly at different parts of the coil, air redistributes itself causing

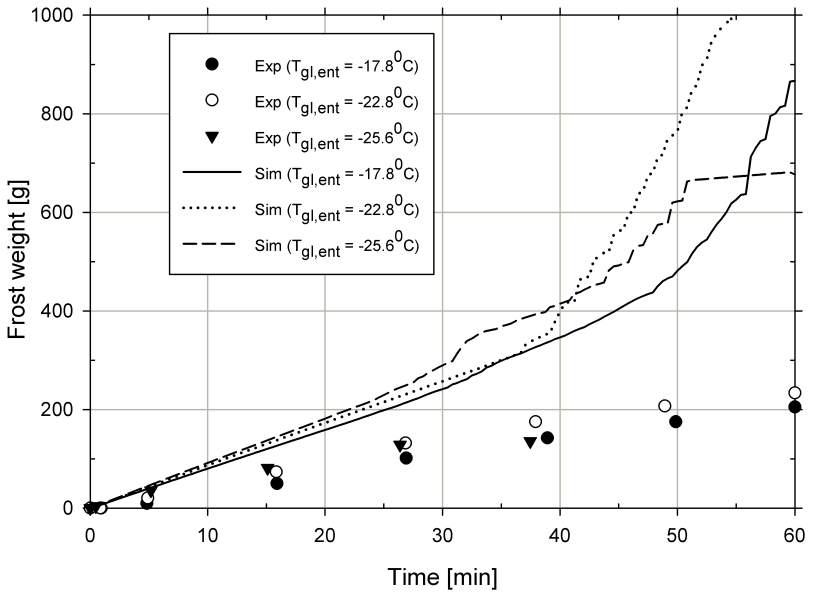

(a) Simple Frost Model

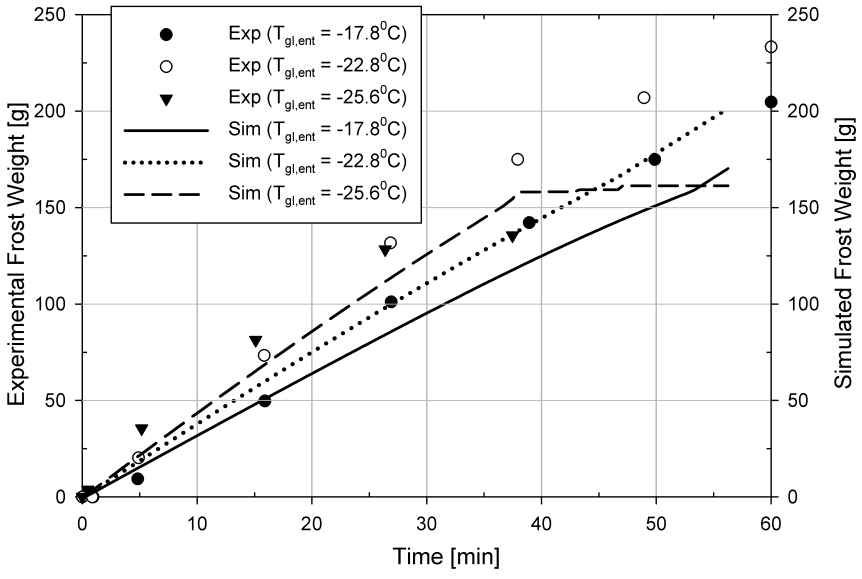

(b) Improved Frost Model

Figure 4.25: Comparison of Total Frost Accumulation on the Coil from Experiments to Simple and Improved Frost Model

the frost growth rate to change. Measured values for frost thickness are compared with simulated results for different parameters affecting frost growth. The model predicted well the thickness at lower temperatures but was inaccurate for high surface temperature case. The discrepancy in the high temperature case was due to the observed delay in the onset of nucleation. The model assumes that frost growth initiates instantaneously. Improvements in the model need to be made to account for the delay in frost initiation on the heat exchanger. The effect of assuming that frosting initiates instantaneously when frosting conditions exist is clearly visible in various relative humidity tests. The predicted mass was also found to be higher than the measured values. The difference in the values suggest that discretization in the air flow direction (depth of fin) is required to capture the no-frost condition observed on the back face of the coil.

An improved frost model is developed which accounts for variation of frost thickness in air flow direction. The improved model addresses party the frost initiation problem observed at warm temperature conditions. The difference introduced by the model for low temperature cases is not very significant. The discretized model also improved the frost mass prediction significantly. With the improved model the difference in predicted frost mass and experimentally measured frost mass was reduced to 13%.

4.13 Conclusions - Microchannel

A quasi-steady simulation model based on scaled parameters is presented for analyzing frost growth in microchannel heat exchangers. Condition required for a valid quasi steady state assumption is derived and it is shown that frost growth problem satisfies that condition. The model is incorporated in a segment-by-segment heat exchanger algorithm. Air redistribution due to

non-uniform frost growth on the heat exchanger is handled by forcing the pressure drop across each segment to be equal. The simulation results show that the frost growth rate is significantly higher for low temperature case. Frost thickness predicted by simulation for different glycol entering temperatures matched experimental values very well. For varying air relative humidities, the frost thickness predicted by simulation matched the experimental values for medium and high RH. For low RH case the model over predicted the measured thickness by 30% towards the end of the test. Model also demonstrated the air redistribution taking place across the segments due to non-uniform frost thickness even when the non-uniformity is comparatively less than that in fin-tube coil. Segments with thicker frost see a reduction in mass flux of air, while the redistributed air increases the mass flux in segments with less frost. Microchannel heat exchanger loses capacity faster and almost linearly through out the frosting period. The results of the model are encouraging and suggest that similar models can be used for both conventional fin-tube and microchannel heat exchangers by correctly accounting for heat transfer correlations and air redistribution calculations. The usefulness of the model can be improved by incorporating the ability to predict the variation in frost density along the direction of flow.

CHAPTER 5

EXPERIMENTAL STUDY OF HEAT PUMP SYSTEMS UNDER FROSTING CONDITIONS

5.1 Introduction

Adoption of microchannel heat exchangers in heat pump systems is a challenge due to faster frost growth. A comparative study of heat pump system with fin and tube and microchannel heat exchanger as outdoor coils is presented in this chapter. Experiments are performed in psychrometric chamber at Johnson Control Inc. facility at Norman, OK. The results obtained from the experiments will also be used to validate the system simulation proposed in Chapter 6.

A detailed review of work done on frost growth for heat pump systems is presented in Chapter 2. A brief summary of the literature as relevant to heat pump systems is provided here. One of the early studies on the effect of frosting on the heat pump system adopting fin-and-tube heat exchanger is by Martinez-Frias and Aceves (1999). The authors developed a model for heat exchanger with frost build up and integrated it with a heat pump system simulation model. Characteristics of the heat pump, such as COP, pressure drop, frost thickness and frosting time were studied. Kim and Groll (2003) reported a comparison between microchannel and a fin-and-tube heat exchangers when used as an outdoor coil in a heat pump system. The study included both cooling and heating tests. The authors reported frosting/defrosting time and the heating capacity of the heat pump with both coils.

Effect of other variables such as heat exchanger inclination, and fins per inch (FPI) were also studied. The authors concluded that microchannel heat exchangers have a shorter frosting time compared to fin-and-tube heat exchangers, and the time decreased even further with each cycle due to residual water retained at the end of each defrost cycle. Kim and Groll (2003) investigated the effect of the orientation of the microchannel tubes and they concluded that slightly inclined tubes in the direction of the air flow was beneficial with respect to a straight vertical configuration. The work by Kim and Groll (2003) focused on the comparison of frosting times and heating performance but their study did not provide sufficient information on frost growth rate and frost build up on microchannel heat exchangers. Xia et al. (2006) studied the performance of a flat-tube heat exchanger with louvered fins in frosting conditions, which resembles a microchannel heat exchanger. An overall heat transfer coefficient was obtained for the heat exchanger using the experimental temperatures and flow rate. Frost thickness was measured using images by a CCD camera, and frost weight was obtained by using a high precision scale. Xia et al. (2006) developed a numerical model, which was also experimentally validated, to predict the frost thickness and blockage ratio.

Several researchers in the field have concluded that water retention is the main cause that penalizes the cycling time of microchannel heat exchangers. However, there is not a clear experimental study that supports this theory and isolates this effect. This is due to the complexity of measuring the frost mass build up on the coil during actual operating conditions. It is also difficult to vary one parameter at a time while maintaining temperatures and pressures constant along the vapor compression cycle because frost growth is a transient phenomenon. Local temperature of fins and wall tubes at various locations in the coil is the key parameter to understand the heat and mass transfer occurring during frost growth and frost melt. A relative comparison between a fin-and-tube coil and a

microchannel coil would provide a better understanding of the behavior of microchannel heat exchanger during frost conditions.

The present work investigates the characteristics of a microchannel heat exchanger with louvered folded fins and a fin-and-tube heat exchanger with straight fins under frosting conditions. The study also aims to identify the possible root causes that penalize microchannel heat exchangers operating as the outdoor coil in heat pump systems. A commercially available 4-ton heat pump system was used in the experimental set up and the outdoor unit was placed in an environmental chamber, which was maintained at ARI (2008) conditions of $35/33^oF[1.7/0.6^oC]$ (DB/WB). Frost build up on the heat exchangers was measured by weighing the entire unit. Quantities such as air temperatures at the coil inlet and outlet (for indoor coil only), refrigerant temperatures at different locations, and fin and tube surface temperatures at different locations of the heat exchanger were measured. The experimental setup and methodology undertaken is explained in later sections. Results obtained from experiments are also presented in this chapter.

5.2 Description of the Facility

Experiments were performed in a psychrometric chamber located at the Norman facility of Johnson Control Inc. A 4-ton R22 unitary heat pump was used in the test set up. The unit was placed between two environmental chambers, which were controlled closely to replicate the outdoor and indoor conditions. Indoor and outdoor chambers are conditioned using glycol circuits and electric reheat coils to achieve required temperatures.

5.3 Measurement & Instrumentation

The outdoor unit was placed on three load cells, each with a maximum capacity of 250 lb[113.3 kg] and precision of 1% of full scale. The load cells were calibrated in-situ with standardized weights and the accuracy on the load cells was determined to be ± 0.6 lb[28.3 g]. The refrigerant flow rate was measured using a Coriolis type flow meter, which was mounted on the unit, and it had a full scale reading of 2400 lb/hr[0.302 kg/s]. Voltage and current readings in the supply lines to the indoor fan, outdoor fan and compressor were measured in order to calculate the power drawn. Pressure transducers and thermocouples were connected at different locations in the refrigerant pipelines and their range and accuracy is given in Table 5.1. In addition to the refrigerant and air temperatures, fin and tube surface temperatures were also measured using 16 fine gage T-type thermocouples. The thermocouples were attached evenly across the heat exchanger face. All the thermocouples were calibrated in-situ. The in-situ calibration resulted in improving the accuracy on the thermocouples to within $\pm 0.4^oF[0.2^oC]$. A video scope is used to record the frost growth on the outdoor coil. Figure 5.1 shows the experimental set up, while Figure 5.2 the close view of the microchannel heat exchanger section that shows the placement of thermocouples. Inlet air conditions were sampled using air samplers to obtain the drybulb and wetbulb temperatures. Conditions leaving the indoor coil were also monitored to calculate the capacity of the unit from the air side. The wet bulb measurement was obtained by using the 'wet sock'method.

Table 5.1: Range and Accuracy of Refrigerant Line Instruments

Instrument	Range	Accuracy (Calibrated)
Pressure Transducer	1000 $psig$(6.89 MPa)	1%
Thermocouple	$-50^oF - 200^oF(-45.5^oC - 93^oC)$	$\pm 1^oF(\pm 0.56^oC)$
Mass flow meter	2400 lbm/hr(0.302 kg/s)	$\pm 0.1\%$

5.4 Experimental Procedure & Data Reduction

5.4.1 Procedure

During frosting tests the outdoor chamber was maintained at ARI test conditions of $35/33^oF[1.67/0.56^oC]$ (DB/WB). The indoor chamber was maintained at $70^oFDB[21.1^oC]$ and air flow rate across the indoor coil was about 1800 $cfm[0.85\ m^3/s]$. The defrost cycle was initiated by a demand defrost control which measures the difference between the coil surface temperature and air inlet temperature to the coil. If the temperature difference is higher than a certain threshold, which depends on the compressor specification for its safe operation, and if it stays above the limit for about 4.5 minutes, then the defrost cycle is initiated. The condenser fan was turned off during the defrost cycle while the indoor fan was allowed to run. The unit was tested under frosting conditions with a fin-tube heat exchanger as baseline outdoor coil. Then, the fin-and-tube was replaced with a microchannel coil heat exchangers, which was designed for similar capacity. Geometry details of both coils are given in Table 5.2. The microchannel coil had about 6% less face area compared to the fin-tube coil for a similar capacity of 4 tons.

Table 5.2: Parameters for Fin-Tube and Microchannel Coils

	Fin-Tube HX	Microchannel HX
Coil height	38 in (0.965 m)	36.38 in (0.924 m)
Coil width	61.3 in (1.557 m)	60.3 in (1.532 m)
Coil depth	0.866 in (22 mm)	0.708 in (18 mm)
Tube material	Copper	Aluminum
Fin material	Aluminum	Aluminum
FPI	16	17
Circuits/Passes	6	1
Number of Rows	36	N/A
Number of Ports	N/A	23

Several tests were conducted in this study; they are summarized in the test matrix of Table 5.3. Fin-and-tube frosting data obtained from test 1 are for dry-coil conditions (Dry), that is, for the first frost/defrost cycle of the unit. The entire outdoor unit was left in the room at ambient temperature overnight and slowly brought to ARI conditions without turning on the compressor or the fans. Test 2 measures the performance of the fin and-tube after the heat pump system reaches steady periodic (Cyclic) conditions, that is, after several frost/defrost cycles in which the behavior of the heat pump becomes periodic. During periodic cycles, the time between defrosts is quite constant. Microchannel heat exchangers are studied in test 3 to 5. Dry and steady periodic conditions are test 3 and 4. Finally, in test 5, the unit was turned off manually at the end of the defrost period and high pressure nitrogen gas was blown through the coil to remove residual water. The unit was turned back on and allowed to run one entire cycle.

Table 5.3: Test Matrix showing different tests performed and Indoor coil flow rate

Test #	Fin-Tube Heat Exchanger		Microchannel Heat Exchanger		
	Dry	Cyclic	Dry	Cyclic	N2
1	X				
2		X			
3			X		
4				X	
5					X

5.4.2 Data Reduction

After periodic cyclic conditions were achieved, the unit runs continuously between heating and defrost modes. The heating capacity of the unit was calculated from the indoor air side measurements as follows:

$$\dot{q}_a = \dot{m}_{a,id} C_{p,a} (T_{ao,id} - T_{ai,id}) \tag{5.1}$$

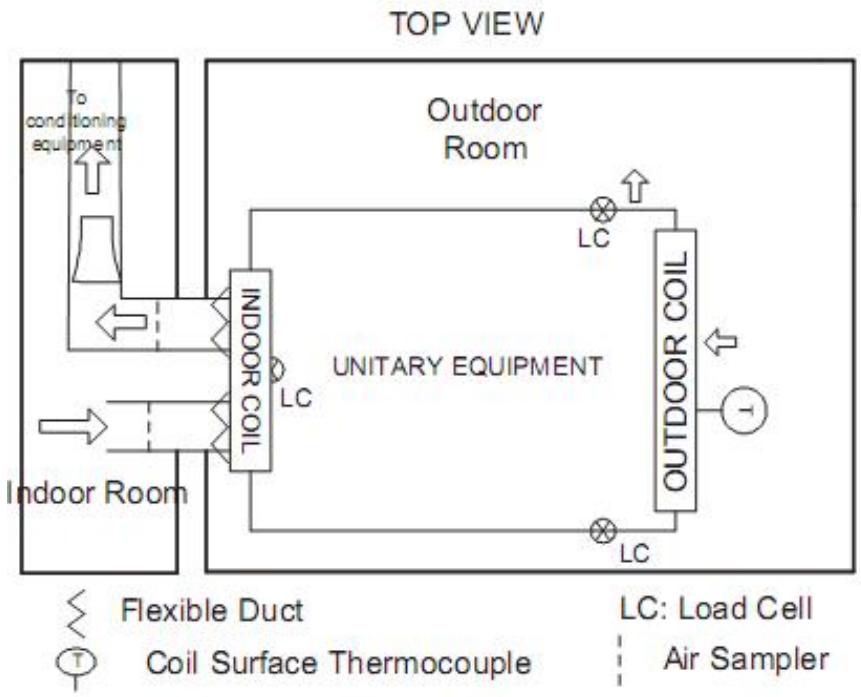

Figure 5.1: Schematic of the Experimental Setup

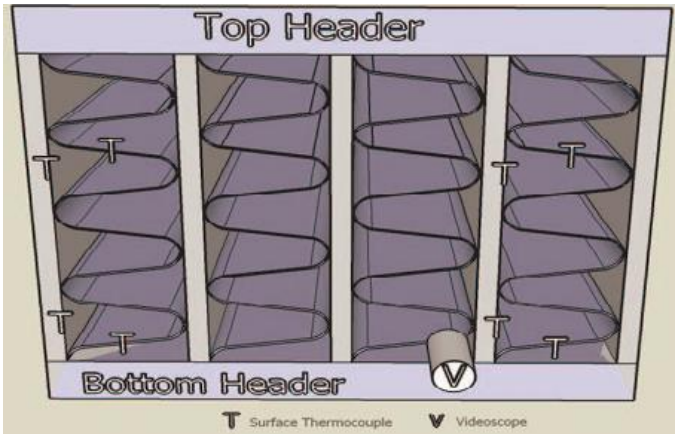

Figure 5.2: Close view of Microchannel with Thermocouples and Videoscope

The average capacity and power input are calculated as given by equation (5.2).

$$\bar{\dot{q}}_a = \frac{\int_0^t \dot{q} dt}{t} \qquad \bar{P} = \frac{\int_0^t P dt}{t} \tag{5.2}$$

The unit's coefficient of performance (COP) was calculated as the ratio of the air side capacity and the total power input to the compressor and outdoor fan. Indoor

fan power was not accounted for in the COP because only the outdoor coil was replaced with between tests while the indoor coil was the same for all tests. The COP was calculated using equation (5.3)

$$COP = \frac{\bar{\dot{q}_a}}{\bar{P}_{comp} + \bar{P}_{od,fan}} \tag{5.3}$$

The EER of the unit is then calculated with the standard conversion formula given in equation (5.4)

$$EER = 3.412COP \tag{5.4}$$

5.5 Results and Discussions

Experimental results are presented in dimensionless form using constants to normalize the plots. Dimensionless quantities preserve the same trend and characteristics of the original data and they protect the proprietary nature of the tests. In this paper, the data are analyzed under four sections; cycle time (frost/defrost), frost weight, coil temperatures, and system performance. The experimental results are also grouped under two different conditions of the coil; dry coil and steady periodic (referred as cyclic). Dry coil was obtained by leaving the unit at the ambient temperature overnight at about 77 F. The outdoor chamber was then cooled by the auxiliary conditioning equipment of the psychometric facility and the ARI H2 test standard conditions were achieved inside the room. Dry coil test refers to the first cycle of the heat pump system after the unit was off overnight. Cyclic test refers to the behavior of the heat pump systems after a few cycles from the first one when near steady-periodic performance had been achieved.

5.5.1 Frost Cycle Time

Frosting time and defrost time for each test are given in Table 5.4. The microchannel coil starting dry, that is, test #3 in Table 5.3, had a frost cycle time of 39m 43 s and a defrost time of about 2m 50s. The cyclic, steady periodic behavior of the same unit during test #4 had a frost cycle time of 23m 13s while the defrost time was 3m 30s. It is clear that the microchannel coil operating at steady state in frosting conditions switches to defrost mode quicker than the same coil starting dry. The cycling time of the microchannel starting dry was about 60% longer than the same coil starting wet after a defrost cycle.

The frost time of microchannel heat exchanger does not increase significantly when the retained water is blown off of coil using pressurized nitrogen gas (test #6). Nitrogen gas was blown through the coil at the end of the defrost cycle and cleared the coil of all visible water. Then, when the unit was turned on, the microchannel heat exchanger accumulated frost at a growth rate similar to the cyclic case (without nitrogen blowing) as described later in section 4.2 of this paper. With Nitrogen blowing about 95% of the water was removed from the coil while in cyclic operations without Nitrogen blowing about 85% of the water drains from the coil. This suggests that water retention is not the primary factor that impacts the frosting cycle time.

In conventional fin-and-tube coils contact between fin and tube is achieved by mechanical expansion of tube. Thus the manufacturing process does not introduce any change in the properties of metals. Unlike conventional fin-and-tube heat exchangers, microchannel manufacturing process relies on oven-brazing. In such a process heat exchanger is completely coated by a flux and is heated in an controlled oven until the metals are brazed together to achieve the thermal contact. In such a process flux would migrate deeper into fin and thus vary the physical characteristics

of the surface. Flux, which is hygroscopic in nature contributes in making the fins more hygroscopic than they normally would be. Thus in a wet cycle (just after defrost), the surface might be saturated with water. The thin layer of water or small water droplets is believed to act as preferential nucleation sites for the frost formation. The significant amount of water that is visibly retained in the coil during normal operation does not practically contribute to shortening the heating period.

Fin-tube coil starting dry on the other hand had a frost cycle time of 49m 13s and a defrost time of 2m 02s. Thus a microchannel heat exchanger with dry starting conditions had a frost cycle time which is 25% less than a fin-tube coil starting dry. Microchannel heat exchanger operating under steady periodic conditions (test #4) performed even worse with about 50% less frost cycle time compared to the fin-and-tube heat exchanger operating under steady periodic conditions (test #2).

Table 5.4: Frost and Defrost Times for Different Cases

	Fin-Tube Dry (Test #1)	Fin-Tube Cyclic (Test #2)	Microchannel Dry (Test #3)	Microchannel Cyclic (Test #4)	Microchannel N_2 Blow (Test #5)
Frost time	49m 13s	41m 07s	39m 43s	23m 13s	24m 25s
Defrost time	2m 02s	2m 32s	2m 50s	3m 30s	3m 02s

It must be noted that the frost times shown in Table 5.4 may a combination of the effect of water retention in the heat exchangers, lower saturation pressure inside microchannel tubes, and refrigerant distribution. The comparison between test #5 (microchannel cyclic) and test #6 (microchannel N_2 blow) aims to isolate the effect of excess water retention at the end of the defrost cycle.

In addition, the capacity degradation of fin-and-tube and microchannel coils at the end of the heating (frosting) period is not the same. The capacity reduction for the fin-tube heat exchanger at the end of heating period is around 16% for the dry coil and 19% for the wet coil. For the microchannel heat exchanger, the heating capacity

degradation was about 25%. The defrost controller of the unit measured the coil surface temperature at outlet to initiate the defrost cycle, regardless of whether the heat exchanger is a fin-and-tube or a microchannel type. This suggests that a different defrost control should be adopted in case of microchannel heat exchangers.

5.5.2 Frost Weight

Weight of frost growing on the heat exchanger surfaces was measured using load cells. The load cells were sensitive to several system related factors in addition to the weight of the frost. These factors included the refrigerant shift when switching between heating and defrost modes, the absence of downward fan force when turned off during defrost periods and dynamic stress caused by the transient loading of the flexible duct that connected the unit to the indoor coil. A calibration procedure was carried out before the experiments to estimate the influence of these factors on the readings from the load cells. Several calibrated weights were placed on the unit to simulate the frost growth. Air conditions were well above freezing point at about 43 F and the unit was manually controlled to switch from heating to defrost modes without having real frost build up on the coil. From the calibration data, a curve fit approach was used to estimate the hysteresis of the load cell and the load induced by the flexible duct. These were found to be within 0.6 lb.

The frost mass that is accumulated on the fin-and-tube and microchannel heat exchanger is shown in Figure 5.3 and 5.4. Figure 5.3 shows the frost build up of fin-and-tube and microchannel heat exchangers starting dry. Frost build up on fin-and-tube and microchannel heat exchangers starting under wet coil conditions is shown in Figure 5.4. The data are presented in form dimensionless frost weight per unit area of the face of coil. Fin-and-tube heat exchanger under both dry and steady periodic conditions accumulated approximately same amount of frost before

going into defrost. However, the steeper slope of the microchannel curve shows that the rate of frost growth of the microchannel was significantly higher than the rate of frost growth of the fin-and-tube. During the first 5 minutes of the heating cycle, the rate of frost growth of fin-and-tube is about 0.006 $lb/(lb - ft^2 - min)$ while the rate is about 0.0086 $lb/(lb - ft^2 - min)$ for microchannel. This suggests that initially frost grows about 43% faster in microchannel than in fin-and-tube heat exchangers. In both fin-and-tube and microchannel heat exchangers the frost growth under dry starting conditions flattened before going into defrost. Fin-and-tube has the lowest frost growth rate and it builds up about 0.06 lb/(lb-ft2) in about 40 minutes (50m for dry starting condition). Microchannel heat exchanger accumulated about 0.065 lb/(lb-ft2) of frost in approximately 24 minutes (40m for dry starting condition). Both tests #4 and #5 gave similar results. The frost weight measurements of Figure 3 also indicate that the frost accumulates during the first part of the heating cycle, that is, approximately during the first 10 minutes.

The frost accumulation was recorded by using a videoscope positioned at less than 1 foot from the lower header of the microchannel heat exchanger, as shown in Figure 5.2. The camera was kept still for the entire cycle and the frost appeared as shown in Figure 5.5. The images were captured at different time during frost growth. The growth of frost layer begins from the microchannel tubes and progress irregularly toward the fins.

5.5.3 Coil Surface Temperatures

Frost formation on the heat exchanger depends on the heat exchanger surface temperature. Lower surface temperature initiates frost growth early [Tao, Besant and Mao (1993)]. Early initiation of frost growth will lead to a reduction in time between defrost cycles. Coil surface temperature measurements for both fin-tube

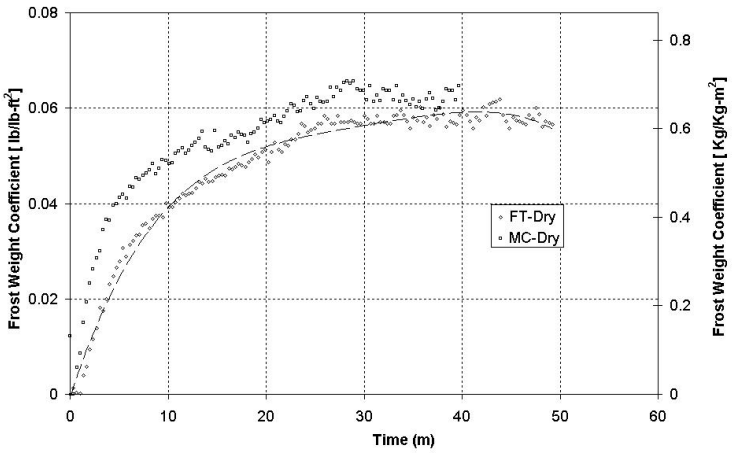

Figure 5.3: Dimensionless Frost Weight - Dry startup conditions

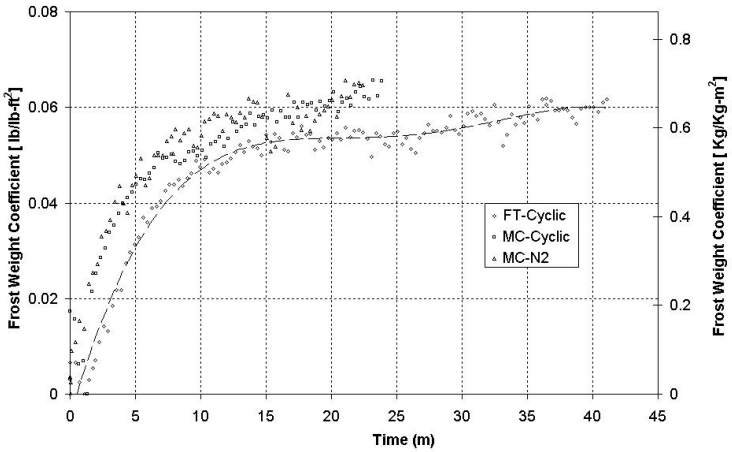

Figure 5.4: Dimensionless Frost Weight - Wet starting conditions

and microchannel coils are made using fine gage (40-gage) thermocouples. Figure 5.6 and 5.7 shows the fin and tube temperatures at two different locations (near the inlet and the outlet) for both fin-tube and microchannel cyclic tests. Thermocouples were located about one foot from the inlet header and outlet headers of the microchannel heat exchanger. The inlet header thermocouple is close to the location of the video scope used to take the pictures shown in Figure 5.2. The local microchannel tube wall and corresponding fin surface temperatures are significantly lower at the inlet of the coil. The temperature difference between inlet air and the surface of the coil is higher for the microchannel coil than for the

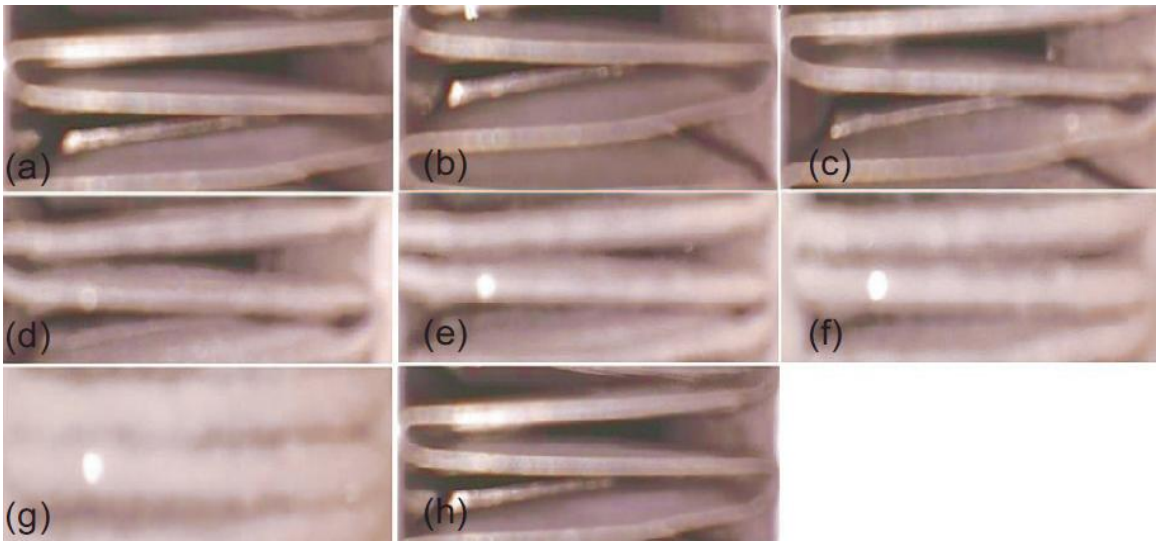

Figure 5.5: Stages of Frost Growth in a Microchannel HX (Defrost to Defrost). [Images taken at following times: (a) start of frost cycle; (b) 3 mins; (c) 7 mins; (d) 11 mins; (e) 15 mins; (f) 20 mins; (g) 23 mins; and (h) just after defrost completion]

fin-and-tube coil. This high temperature difference impacts the frost growth rate but further investigation is necessary to quantify this effect.

Tube and fin thermocouples are located near the circuit inlet and outlet for the fin-tube heat exchanger. Similar temperature profiles at the inlet and the outlet (as shown in Figure 5.6) suggests that frost grows uniformly on the entire face area of the fin tube coil. On the other hand, for the microchannel heat exchanger, the local temperatures near the inlet and outlet are significantly different, as shown in Figure 5.7. This suggests that the frosting on the microchannel coil is not uniform. Near the inlet header frost begins immediately, but onset of frosting is delayed near the outlet. Visual observation of the microchannel coil during frosting confirms these conclusions. The weight measurements and local temperature curves together suggest that the frost growth pattern in fin-tube and microchannel heat exchangers are quite different. Controlled wind tunnel experiments are proposed in 3 in order to investigate the frost mechanism in microchannel coils.

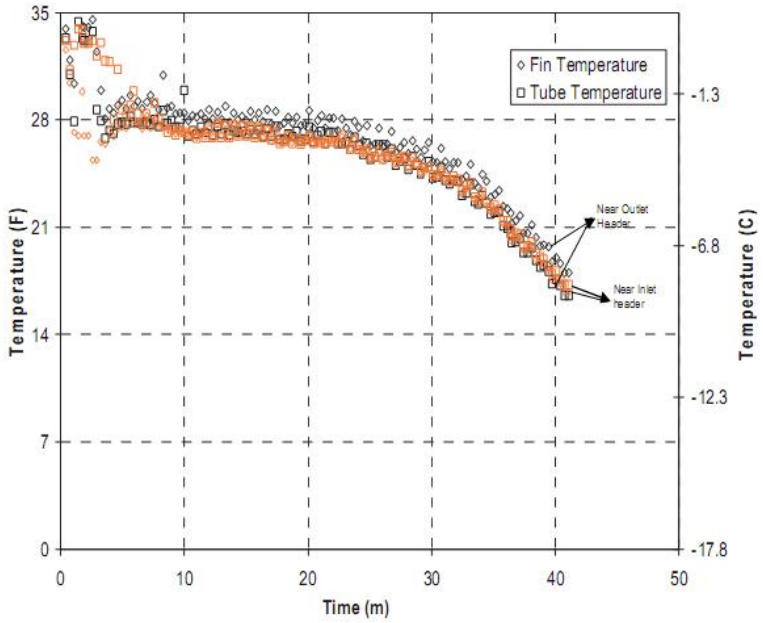

Figure 5.6: Temperatures of Fin and Tube Surface - Fin-Tube HX

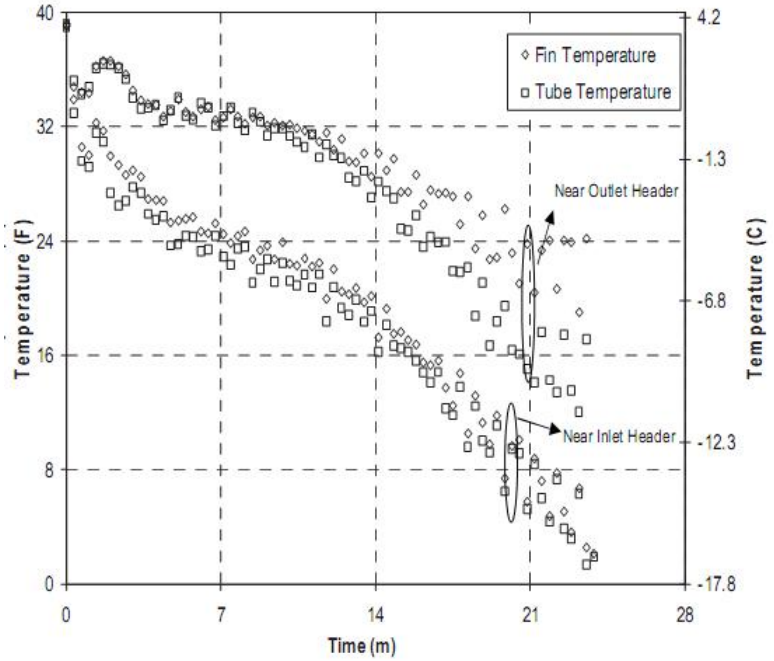

Figure 5.7: Temperatures of Fin and Tube Surface - Microchannel HX

5.5.4 Performance Evaluation

The heating capacity and the EER for the unit were calculated using the equations (1) through (4) discussed in section 5.4.2. The quantities were normalized by using

the maximum capacity and maximum EER for the fin-tube dry run, which was chosen as the baseline case. Figure 5.8 and 5.9 shows the variation of capacity and EER respectively for the unit over the entire frosting cycle, defined as time from termination to termination of the defrost cycle. The data presented are for fin-and-tube dry test, fin-and-tube cyclic test, and microchannel cyclic test. For all the three cases the average capacity increases initially and flattens out in the final stages of frost growth period. The drops of the capacity is due to the defrost stage, at which point the heating capacity of the unit becomes zero. The microchannel heat exchanger also has less capacity and EER compared to fin-tube coil. The average capacity of the microchannel coil over its entire cycle is about 27% less than the dry fin-tube coil and 22% less than the cyclic fin-tube case. The EER of the heat pump system with microchannel coil is also about 13% lower than the same unit with fin-and-tube coil.

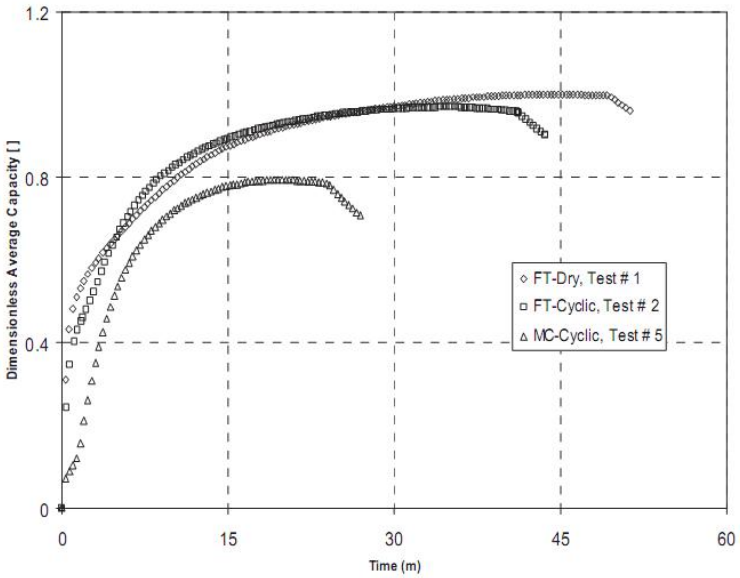

Figure 5.8: Comparison of Average Capacity

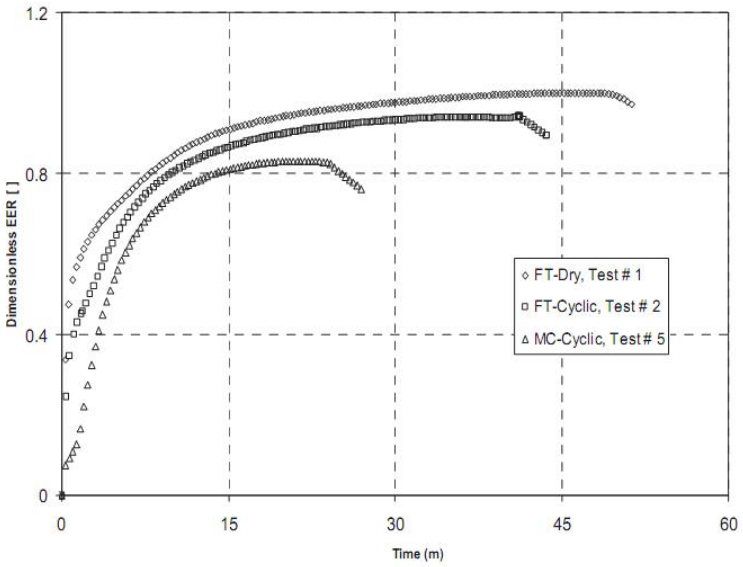

Figure 5.9: Comparison of Average EER

5.6 Conclusions

A 4-ton heat pump system using a fin-tube outdoor coil was compared with the same unit using a microchannel coil. Tests were conducted at the ARI 210 H2 test conditions and local surface temperatures and weight of the coil were taken in real time during the experiments. The fin and tube heat exchanger had considerably longer time between defrost cycles, and about double than the microchannel coil used in our experiments. Blowing nitrogen on the microchannel coil removed all visible water retained in the coil after the defrost cycle but the time between defrost cycles increased only by 4% with respect to wet and frost conditions. The cycle time of the same microchannel starting with dry condition was about 60% longer than the same coil starting wet. It was also observed that the frost growth rate in the microchannel heat exchanger is higher compared to the fin-tube coil. The surface temperatures are lower, promoting high heat transfer rate but also high frost growth rate. The frost growth patterns were also found to be quite different for fin-tube and microchannel coils. The average capacity of the microchannel coil over its entire cycle was lower by about 22% with respect to the fin-tube coil. The EER of the

heat pump system with microchannel coil is also about 13% lower than the same unit with fin-and-tube coil.

This work showed that the significance of parameters contributing to frost growth are not well understood. Water retention, which was generally assumed to be a major contributing factor to frost growth appears to have only a small effect.

The data sets developed from the experiments will be suitable for validating the heat pump system simulation that is developed as apart of this research.

CHAPTER 6

SIMULATION OF HEAT PUMP SYSTEMS UNDER FROSTING CONDITIONS

6.1 Description of the System Simulation

A steady state program to design vapor compression refrigeration system was developed and described by Iu (2007). A successive substitution solution scheme was utilized to perform calculations pertaining to a vapor compression cycle. The program can also simulate the off-design performance of vapor compression systems. In both design and simulation modes, the heat exchanger data (construction and geometry) and compressor performance data [ARI (1999a)] need to be supplied by the user. In 'design mode' calculation the objective is to calculate the required charge and dimensions of expansion device for a given capacity, while in 'simulation mode' the objective is to find out the actual operating points of the cycle. Design engineers use simulation mode to study the operation of the system at various off-design conditions. Simulation mode is also used by engineers to reduce the physical testing of units in psychrometric chambers.

Depending on which mode of operation (design or simulation), the program has two or three iteration loops. In design mode the two iteration loops are related to pressure and energy balance, while in simulation mode the three iteration loops relate to pressure, energy and mass balance. All four components of a vapor compression system along with additional components such as liquid line and

suction line, filter drier (also reversing valve, accumulator in the case of heat pump) are simulated successively. Since the solution is achieved by means of successive substitution, the loop needs to be broken at one point. Typically it is done at the compressor inlet since many controls associated with operation of the system is dependent on this state. Components are divided into high pressures side (Compressor, condenser, liquid line and expansion devices) and low pressure side (evaporator and suction line). A pressure balance and energy balance is obtained between low pressure and high pressure sides.

Depending on the expansion device present in the system two different approaches are taken for simulating the vapor compression cycle. For systems with an orifice a 'Fixed Orifice Simulation' is used, while for systems with a thermal expansion valve 'TXV Simulation' is used. The methods differ in what values are specified for the system. While air side conditions and system charge are specified for both cases, the TXV simulation also requires a value of Evaporator super heat to be specified. The inputs required (coil and compressor date) are same for both orifice and TXV simulation. Convergence parameters are also different for the two methods; Fixed orifice simulation converges on flow equilibrium and evaporator superheat, while TXV simulation converges on condenser subcooling and calculated evaporator superheat. Figure 6.3 shows the algorithm used for fixed orifice simulation, while Figure 6.4 shows the algorithm used for TXV simulation.

A brief description of the components in the system simulation will be presented here for providing context. The simulation consists of four basic components and depending on the system can have additional components. The vapor compression system with basic components is shown in Figure 6.1.

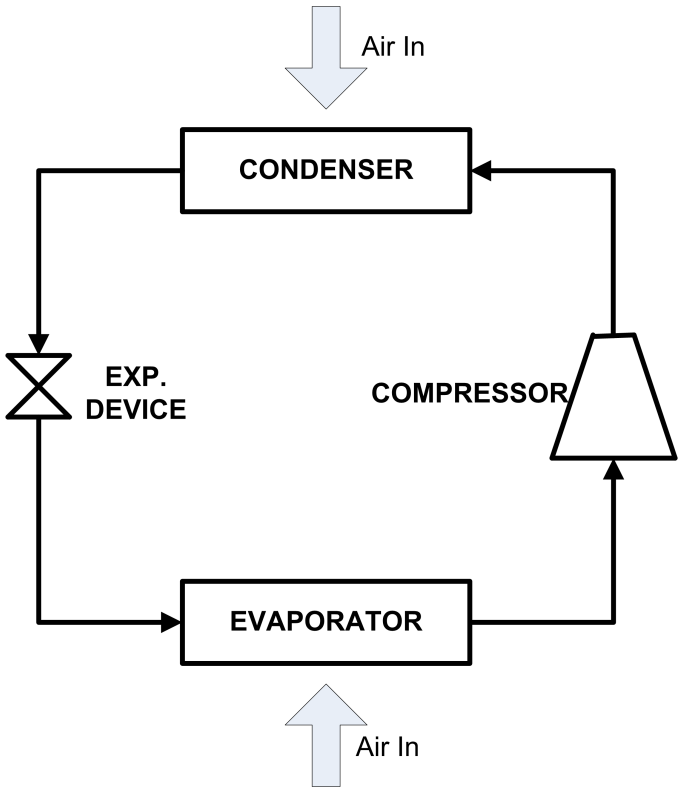

Figure 6.1: Schematic showing basic Vapor Compression System

6.1.1 Compressor

Mass flow rate and power consumption for the compressor is calculated by using a 10 coefficient polynomial model provided by ARI (1999*b*). The model takes the suction and discharge saturation temperatures as input and calculates the mass flow rate of refrigerant, power consumption and outlet enthalpy of refrigerant. With a known suction and discharge saturation temperatures, the outputs are calculated as follows

Mass flow rate of refrigerant:

$$\dot{m}_{cmp,rated} = a_1 + a_2 T_{sat,suc} + a_3 T_{sat,dis} + a_4 T_{sat,suc}^2 + a_5 T_{sat,suc} T_{sat,dis} + a_6 T_{sat,dis}^2 + a_7 T_{sat,suc}^3 + a_8 T_{sat,suc} T_{sat,dis}^2 + a_9 T_{sat,suc}^2 T_{sat,dis} + a_{10} T_{sat,dis}^3 \tag{6.1}$$

Power consumption by the compressor:

$$\dot{W}_{cmp,rated} = b_1 + b_2 T_{sat,suc} + b_3 T_{sat,dis} + b_4 T_{sat,suc}^2 + b_5 T_{sat,suc} T_{sat,dis} + b_6 T_{sat,dis}^2 + b_7 T_{sat,suc}^3 + b_8 T_{sat,suc} T_{sat,dis}^2 + b_9 T_{sat,suc}^2 T_{sat,dis} + b_{10} T_{sat,dis}^3 \tag{6.2}$$

When the compressor is working at conditions other than the ARI rated conditions, correction equations are published in the literature and takes the following form.

$$\dot{m}_{cmp,act} = \left(\frac{\rho_{ref}}{\rho_{ref,rated}} \right) \dot{m}_{cmp,rated} \tag{6.3}$$

$$\dot{W}_{cmp,act} = \left(\frac{\dot{m}_{cmp,act}}{\dot{m}_{cmp,rated}} \right) \left(\frac{\Delta i_{ref,isen}}{\Delta i_{ref,isen,rated}} \right) \dot{W}_{cmp,rated} \tag{6.4}$$

Since the discharge pressure is known to the compressor model, outlet state can be fixed by knowing outlet enthalpy. The outlet refrigerant enthalpy is calculated by employing an energy balance across the compressor.

6.1.2 Heat Exchangers

The modeling methodology for condenser and evaporator heat exchanger is described in detail in 4.4. The only difference for a condenser model from an evaporator model is that no moisture condensation calculations need to be performed during the simulation of condenser heat exchanger.

6.1.3 Expansion Device

The simulation is capable of simulating two common expansion devices used in heat pump systems, viz. short tube orifice and thermal expansion valve (TXV). The expansion device is basically modeled as a isenthalpic component, and the aim of

the model is to calculate the refrigerant flow. System simulation with short orifice plate uses the refrigerant flow to determine convergence, while for systems with TXVs, the model is used to determine the subcooling in the liquid line. The dimensionless refrigerant flow rate through a short-tube orifice plate is calculated using equations provided by Payne and O'Neal (2004) as follows:

For a single phase sub-cooled refrigerant at the inlet

$$\pi_1 = \frac{c_1 + c_2\pi_2 + c_3\pi_3 + c_4\pi_4 + c_5 \ln \pi_5}{1 + c_6\pi_2 + c_7\pi_4^2} \tag{6.5}$$

Constants $c_1 \ldots\ c_7$ are empirically determined. Dimensional quantities $\pi_1 \ldots\ \pi_7$ are calculated as

$$\begin{aligned}
\pi_1 &= \frac{G}{\sqrt{\rho_{liq} P_{crit}}}; \quad P_{crit} \text{ in Pa} \\
\pi_2 &= \frac{P_{in} - P_{sat}}{P_{crit}} \\
\pi_3 &= \frac{\rho_v}{\rho_l} \\
\pi_4 &= \frac{\Delta T_{sub}}{T_{crit}}; \quad T_{crit} \text{ in K} \\
\pi_5 &= \frac{L_{orifice}}{D_{orifice}}
\end{aligned}$$

For two phase inlet condition, the refrigerant flow is calculated by employing a correction factor to the flow at saturated conditions. The equation for two-phase refrigerant flow takes the form

$$\pi_{1,TP} = C_{TP}\pi_{1,sat} \tag{6.6}$$

C_{TP} is the correction factor and is calculated as follows:

$$C_{TP} = \frac{d_1\pi_6 + d_2\pi_6^2 + d_3(\ln \pi_6)^2 + d_4(\ln \pi_{10})^2 + d_5(\ln \pi_8)^2 + d_6(\ln \pi_5)^2}{1 + d_7\pi_6 + d_8\pi_9 + d_9\pi_7^3} \tag{6.7}$$

Dimensionless quantities $\pi_1 \ldots \pi_7$ are calculated as:

$$\pi_1 = \frac{G}{\sqrt{\rho_{liq} P_{crit}}}; \quad P_{crit} \text{ in Pa}$$
$$\pi_2 = \frac{P_{in} - P_{sat}}{P_{crit}}$$
$$\pi_3 = \frac{\rho_v}{\rho_l}$$
$$\pi_4 = \frac{\Delta T_{sub}}{T_{crit}}; \quad T_{crit} \text{ in K}$$
$$\pi_5 = \frac{L_{orifice}}{D_{orifice}}$$

6.1.4 Accumulator

In heat pump systems, the outdoor coil acts as condenser in cooling mode and thus the outlet will be subcooled liquid. When the unit switches to heating mode the outdoor coil now becomes evaporator. However the subcooled liquid at it's outlet will not evaporate at once and it could migrate to compressor suction, which is detrimental to the compressor. In order to avoid this problem an accumulator is used in heat pump systems. The function of accumulator is to avoid liquid refrigerant from entering compressor by storing it. As the system stabilizes after the mode switch, the refrigerant in the accumulator evaporates completely and leave the accumulator dry. However this might not be true in cases where the refrigerant is over-charged or during frosting conditions. Under frosting conditions, the evaporator loses capacity which will result in a reduction of superheat as time increases. When the loss in evaporator capacity is significant enough to result in

two-phase refrigerant coming out of the evaporator, the accumulator stores the liquid refrigerant.

An accumulator is essentially a storage tank with two openings, one for refrigerant inlet and one for refrigerant outlet. The refrigerant outlet sticks into the tank in the shape of a J-tube. Figure 6.2 shows the cut-away view of an accumulator.

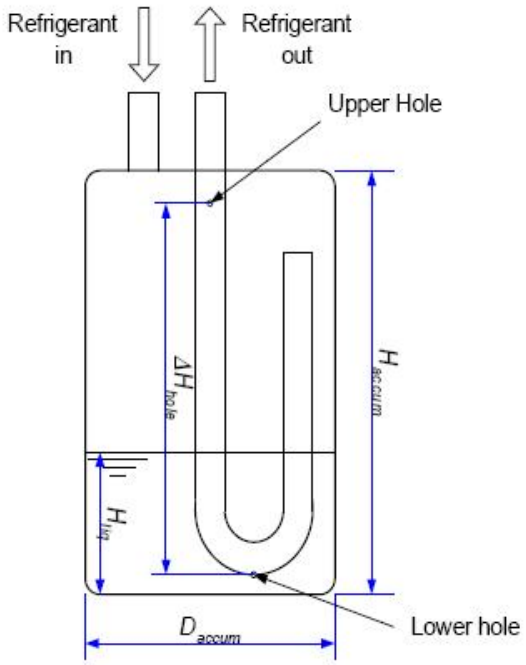

Figure 6.2: Schematic showing cut-away view of an Accumulator

Liquid phase in the two-phase refrigerant entering the accumulator will be stored at the bottom of the tank, while the vapor phase will enter the J-tube. The two holes in the J-tube will allow any residual liquid refrigerant to flow back to the tank. Liquid refrigerant could occur in the J-tube due to following reasons:

- Pressure drop in the J-tube resulting in some vapor condensing into liquid
- Poor accumulator design resulting in the inlet of the J-tube staying below the liquid level

- Turbulence in the two phase fluid causing some liquid to move into the tube where it condenses

The accumulator model basically calculates two quantities; the height of the liquid column in the accumulator (mass of liquid refrigerant) and the pressure drop introduced by the accumulator. The model is useful in frosting conditions, where towards the end of the frosting period, there may be liquid refrigerant leaving the evaporator. In such case the mass of liquid refrigerant needs to be accounted for during the whole system simulation. If the amount is not accounted for the system simulation will converge on a higher evaporator pressure thereby under-estimating the deterioration of performance due to frosting. The equation used to calculate the pressure drop in the accumulator is given as follows

$$\Delta P_{acc} = \frac{\dot{Q}_{rated}}{\dot{Q}_{max}} \Delta P_{rated} \tag{6.8}$$

Compressor rated capacity ($\dot{Q}_{rated}$) is published by manufacturers for a given pressure difference ($\dot{P}_{rated}$). A correlation for maximum accumulator capacity ($\dot{Q}_{max}$) against saturation refrigerant temperature is developed from the manufacturer's data.

6.2 System Simulation Methodology

As described previously, vapor compression system simulation is done differently depending on the type of expansion device (*Fixed orifice* or TXV). In either case the whole simulation consists of three nested loops for momentum, energy and mass balances. For either of the expansion devices the program takes heat exchanger geometry and compressor parameters as inputs.

The fixed orifice simulation, which is shown in Figure 6.3, starts with guessing the

suction and discharge saturation temperatures along with suction superheat. In addition to the heat exchanger and compressor inputs, the charge in the system is also taken as an input. Since the fixed orifice has no control on the superheat, the final converged result will give the operating superheat temperature of the system. At the high pressure side, the convergence criterion is balancing the compressor and orifice flow (momentum/pressure balance). Once the high side is converged, the simulation proceeds to the low (evaporator) side. Convergence in the low side is equalizing the calculated evaporator super heat to the guessed superheat. When the low side is converged, a new suction saturation temperature is obtained. The low side convergence results in an energy balance for the whole system. With the new suction saturation temperature the high side is re-simulated. Once both sides are converged, the system charge is calculated and compared to input system charge. If the calculated charge and input charge are beyond tolerance, a new super heat is guessed and the simulation repeated. The process repeats until the calculated charge matches input charge (mass balance) at which point superheat convergence and mass flow rate convergence are satisfied.

In systems with TXV as the expansion device, as shown in Figure 6.4, the thermal expansion valve maintains a fixed superheat by controlling the flow rate through the evaporator. As a result of fixed suction superheat, load variation results in varying subcooling. Therefore, for a TXV simulation, instead of guessing superheat the program guesses a value for subcooling. The high side convergence is based on the calculated subcooling matching the guessed subcooling. The low side convergence is similar to fixed orifice simulation with the exception that the calculated value is matched to the input value of superheat that the TXV is designed to control. For the third convergence loop, the system charge is compared to given system charge and if beyond tolerance, the guessed subcooling is changed.

Figure 6.3: Flow Chart Showing Simulation Algorithm for Systems with Orifice as Expansion Device (Iu, 2007)

Typically the effect of frost growth is not a concern for an engineer during the system design phase. Once a system is designed to meet required design criterion, it is desirable to understand how the system performs under frosting conditions. Thus the frost model developed in this study is integrated in the simulation mode. As previously discussed, the dynamics introduced by frost is slow compared to the dynamics due to the vapor compression system components. This allows use of a

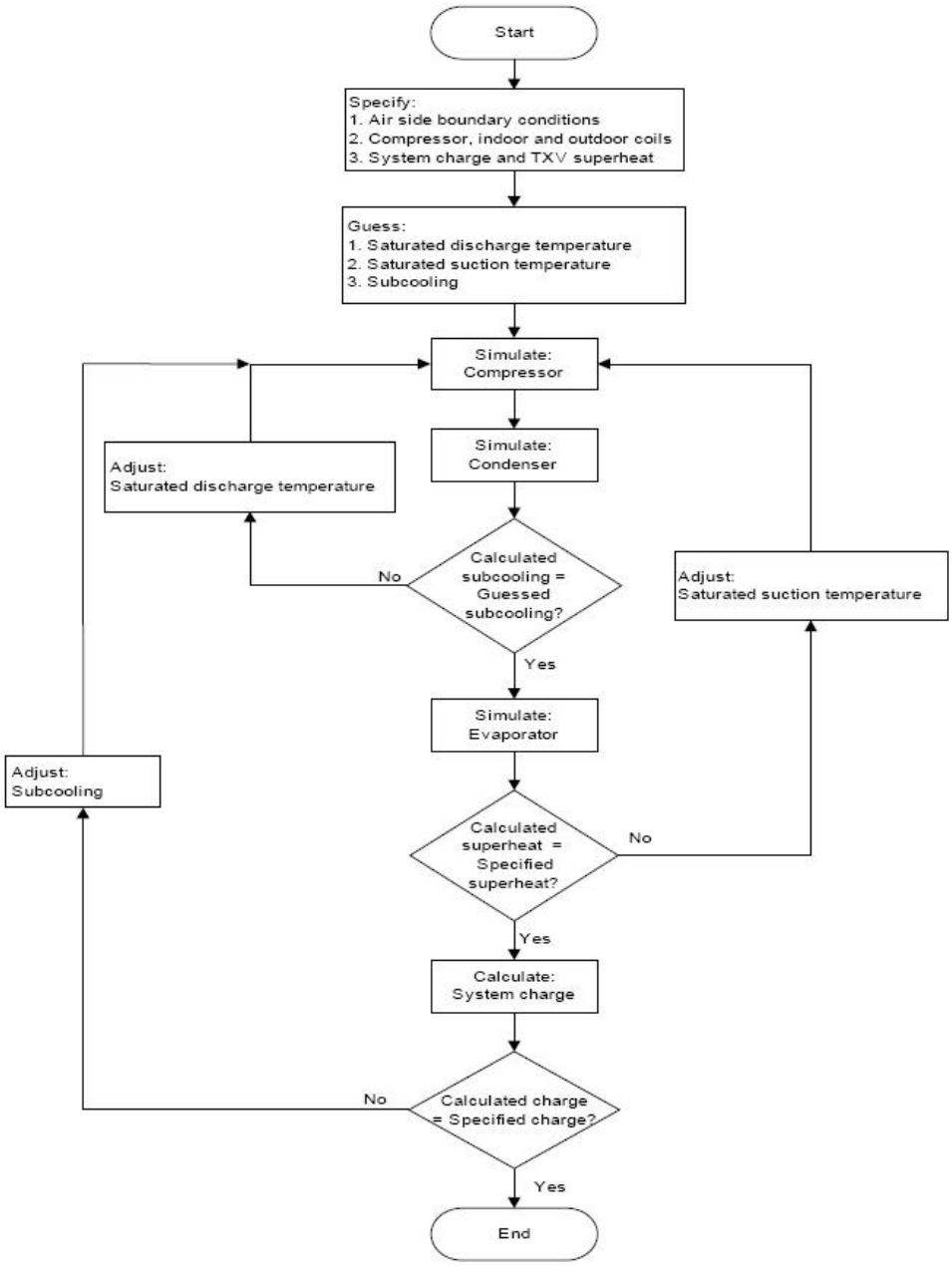

Figure 6.4: Flow Chart Showing Simulation Algorithm for Systems with TXV as Expansion Device (Iu, 2007)

quasi-steady state approach to integrate the simulation with the frost model.

At each time step the system simulation is performed first and the refrigerant conditions in the evaporator are determined. Then the frost model is called to calculate the frost thickness and frost conductivity. With the frost thickness

calculated, the evaporator air side pressure is recalculated. Recalculated evaporator air side pressure drop is used to determine the operating point of the outdoor fan. A fan curve for the outdoor fan needs to be supplied by the user to effectively vary the air flow through the heat exchanger as the coil frosts up. This new air flow rate is used for the system simulation calculations in the next time step. After the frost model is finished the defrost initiation condition is checked. If the defrost initiation condition is satisfied the simulation ends; otherwise it proceeds to the next time step. The algorithm showing the combined vapor compression simulation and frost growth model is shown in Algorithm 3.

```
repeat
    Simulate vapor compression system;
    Obtain refrigerant temperatures in each segment of evaporator;
    Solve frost model for the evaporator [Alg. 2];
    Check defrost initiate condition;
    if Defrost Initiated then
        Terminate Simulation;
    end
    else
        Determine air side pressure drop with updated frost thickness;
        Solve fan curve to obtain current operating point;
        Update the outdoor coil flow rate;
        Increment time step (t_new = t_old + Δt)
    end
until Defrost initiation ;
```

Algorithm 3: Overall Quasi-Steady Solution Algorithm for Vapor Compression System with Frost Growth

6.3 Validation of whole system simulation

The whole system simulation algorithm with the frost model is validated with the experimental data obtained from the experimental facility described in Chapter 5. For the study presented in this thesis, only the fin and tube system validation is performed. Measured and simulated results are compared for the following system

outputs

1. System capacity: Frost growth will affect the system capacity by decreasing outdoor unit heat transfer. However in the experiments the outdoor heat transfer rate was not measured. System capacity is measured across the coil (condenser in heating mode) and compressor power is measured. The validation will be carried out in two ways:

    - Model results for heat transfer across indoor coil will be compared with measured indoor coil heat transfer
    - Model results for heat transfer across outdoor coil will be compared to outdoor coil heat transfer obtained by applying energy balance between indoor coil, compressor and outdoor coil

2. System EER: Coefficient of performance for dry start cycle will be compared to the system EER value obtained from the simulation.

3. Refrigerant flow rate: As frost grows on the outdoor coil, the evaporator outlet becomes colder. This is due to reduced heat transfer across the evaporator and consequent reduction in evaporator pressure. As the evaporator outlet changes to two-phase from superheated vapor, the remaining liquid refrigerant is stored in accumulator. Since the frost continues to grow the accumulator does not run dry which would happen in other steady state conditions. As the accumulator stores more liquid, the amount of refrigerant flowing in the system drops.

The system used in the experiments consisted of a constant speed fan for the outdoor coil. As frost grows on the coil, the pressure drop increases and this causes the air flow across the coil to drop. As explained in the development of frost model

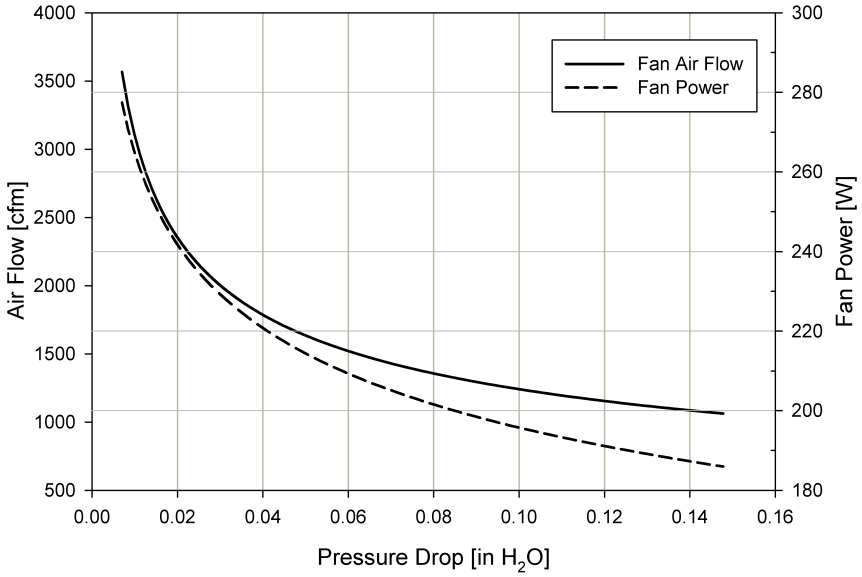

Figure 6.5: Fan Air Flow and Fan Power Curve for the Fan in the Unit

in Section 4.4, the pressure drop across the coil is obtained using the same form of correlation, but accounting for change in free flow area and total tube/fin area. The fan used in the unit is tested separately to develop the air flow - pressure drop curve. This helps to calculate the flow rate for the unit as frost grows. The fan curve developed is shown in Figure 6.5

In the experiments, the system capacity is measured at the indoor coil for both cooling and heating modes. There was no measurement of air flow across the outdoor coil or the air outlet conditions across the outdoor coil. As a result the heat transfer rate across outdoor coil is not directly measured. Air flow rate and inlet and outlet air conditions are measured across indoor coil which allows to calculate the system capacity. System capacity obtained from experiments and simulation is shown in Figure 6.6. The experiments show initial transience and the system capacity increases to maximum value as the system stabilizes. Since the simulation is quasi-steady state, the capacity at the start does not account for system dynamics. Once the system reached the steady operating conditions, the capacity

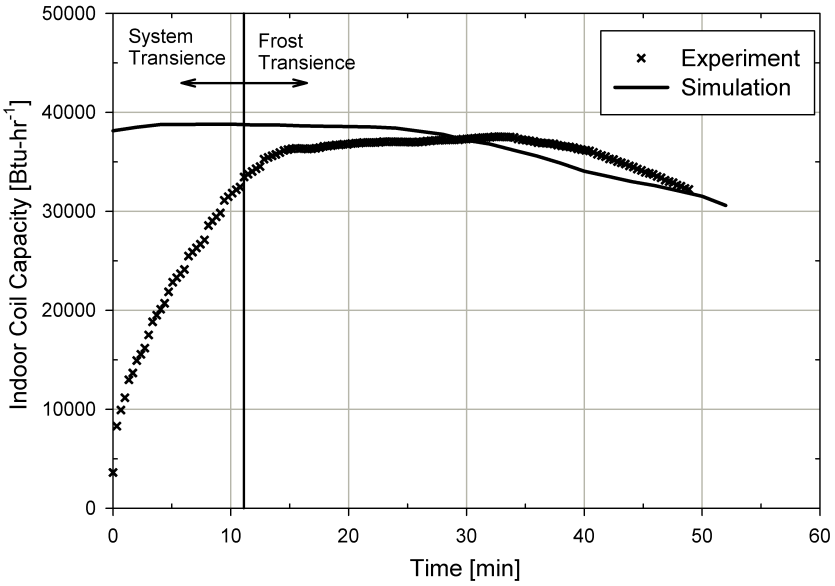

Figure 6.6: System Capacity Measured at Indoor Coil

stays almost constant for approximately 30 minutes. Similar results are obtained from the simulation, where the capacity stays constant for around 30 minutes after which it starts to drop faster.

Figure 6.7 shows the deterioration of system EER as frost grows. EER of the system is affected by all the three quantities, indoor coil capacity, compressor power and total fan power. Of the three quantities, the deterioration of EER due to to frost growth can be attributed mostly to indoor coil capacity and compressor power. The outdoor coil fan power decreases as the frost grows due to the fact that the air flow through the coil decreases. However this reduction in fan power is negligible compared to compressor power and coil capacity. As frost grows the indoor coil capacity reduces as discussed previously. The refrigerant flow in the system also drops as frost grows since the operating pressure of the outdoor coil drops. Higher pressure differential between suction and discharge across compressor results in lesser refrigerant flow which results in lower compressor power. Reduction in refrigerant flow in the experiments and the simulation is shown in Figure 6.8.

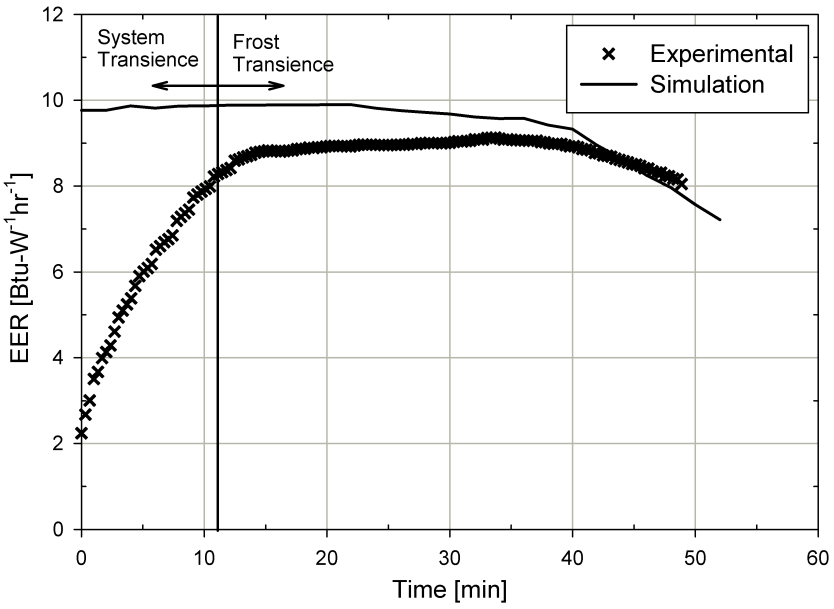

Figure 6.7: System EER

However for the whole system the drop in system capacity exceeds the reduction in compressor power and thus results in drop in EER.

As discussed previously, a major factor that causes the deteriorated performance during frost growth is the increase in pressure drop and the consequent drop in air flow. since in an evaporator, the air side capacity is the limiting factor for the heat transfer rate, a drop in air flow leads to a drop in coil capacity. Figure 6.9 shows the increase in pressure drop and drop in air flow rate through the outdoor coil as predicted by the simulation. It can be seen that the drop in capacity for outdoor coil follows the drop in air flow rate. For the first 30 minutes, the drop in air flow is not significant and thus the drop in capacity is not appreciable.

The system under consideration has 36 tubes consisting of 6 similar circuits as shown in Table 5.2. Since the system consists of refrigerant (R22), the refrigerant inlet is not the coldest part of the coil. Due to the pressure drop in the evaporator coil, the coldest part is somewhere in between the coil inlet and part where the

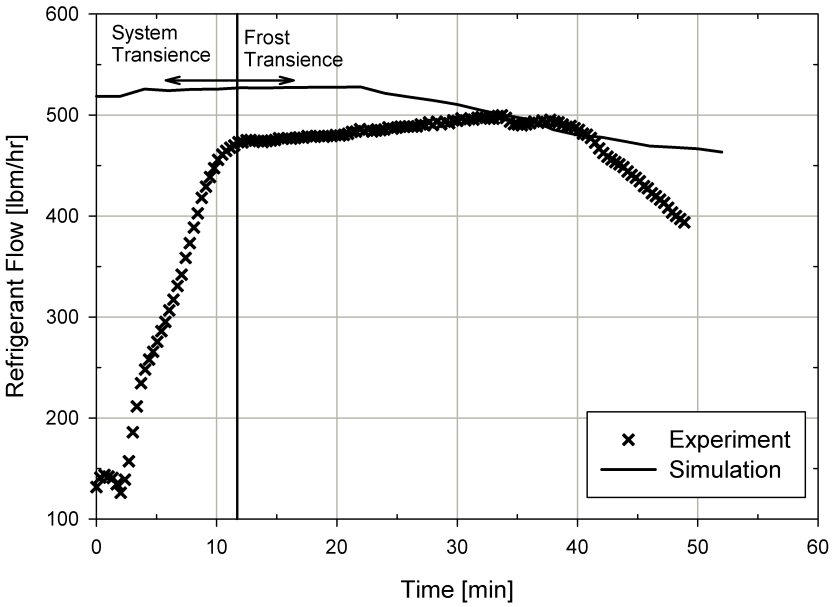

Figure 6.8: Refrigerant Flow Rate through the System

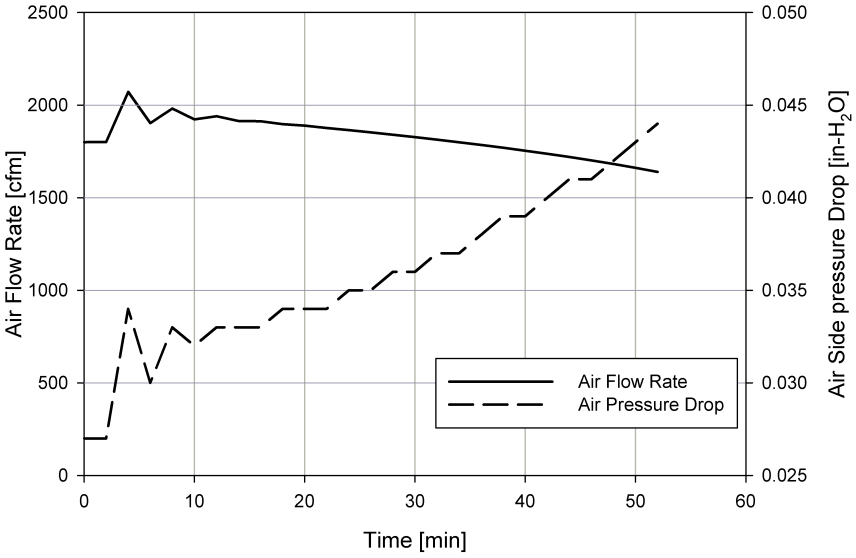

Figure 6.9: Simulated Outdoor Coil Air Flow rate and Pressure Drop

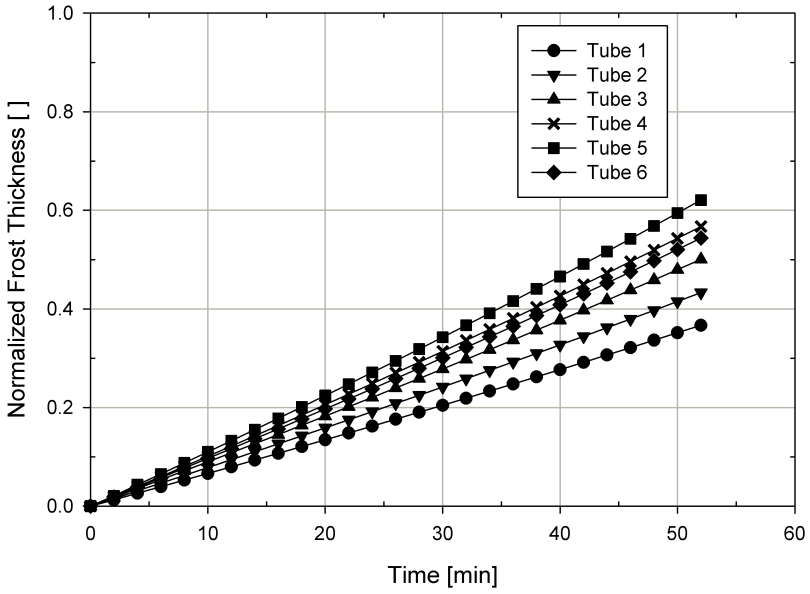

Figure 6.10: Normalized Frost Thickness (Simulated) for Different Tubes of Outdoor Coil

refrigerant becomes superheated. Figure 6.10 shows the frost thickness for tubes in one circuit. Since the coil consists of six similar circuits, the frost profile is same for remaining five circuits. From the figure it can be seen that the maximum frost thickness happens in the fifth tube followed by the fourth and then by the sixth tube. The trend in capacity drop is not directly visible from the frost thickness profile shown in the figure. However it can be deduced that initially when the capacity is flat the air redistributed across the coil to tubes one through four. During the latter part when the tubes one through four have also accumulated enough thickness, the capacity started to drop.

CHAPTER 7

CONCLUSIONS & FUTURE WORK

Frost growth on fin and tube and microchannel coils that are used as outdoor coils in heat pump systems was studied experimentally and numerically. Important conclusions that can be derived from this work is discussed here. In addition to the conclusions, a few topics that warrant further research will also be discussed.

7.1 Conclusions

7.1.1 Experimental Study

1. An experimental facility capable of performing frost tests for a wide range of air and refrigerant conditions was designed. Various key parameters related to frost growth, viz., frost thickness, frost weight, air flow and inlet and outlet air temperature and humidities can be measured. Frost tests were performed for varying glycol entering temperatures, air humidity ratios and air flow rates.

2. Frost growth was significantly affected by the glycol temperature (and consequently surface temperature) for both fin-tube and microchannel coils. The rate of frost growth for a microchannel for a given temperature is significantly greater than fin and tube.

3. Type and density of frost formed was heavily influenced by the temperature of the heat exchanger surface. Low temperatures resulted in a less dense frost

which covered the fins faster thereby reducing the air flow significantly. As a result the final frost weight accumulated for low temperature cases is approximately 16% lower than the high temperature case in fin and tube heat exchanger.

4. Air humidity ratio also affected the frost growth rate on the heat exchanger surfaces. Higher humidity ratio caused faster and higher frost accumulation. The density of frost was not significantly influenced by the air humidity ratio. A change of 20% in air relative humidity resulted in the rate of frost growth to vary by 80% (once the frost is initiated).

5. Air flow rate (air face velocity) did not have a significant impact on the rate of frost accumulation. The frost growth rate and accumulation for range of air face velocities typically seen in outdoor coils of residential and light commercial heat pumps were found to be within experimental uncertainty. The variation in frost thickness observed for a high air flow and low air flow conditions was mostly within ±5% with the highest variation being ±10%

6. The conventional method of heat transfer coefficient deduction is not suitable in the case of a non-uniformly frosted coil. The limiting range of non-uniformity on the face of the coil which can allow a uniform frost thickness assumption needs to be analyzed. For a near-uniformly frosted coil (as is the case for microchannel), the air side heat transfer coefficient can be deduced by accounting for frost layer thickness and resistance in hydraulic diameter fin efficiency calculations. For the range of conditions covered in this study for microchannel heat exchanger, it was found that a 1-D heat conduction through the frost layer is a good assumption.

7.1.2 Modeling Study

1. A new physical model was developed for predicting frost growth in heat exchangers. The frost model can be easily applied to both fin-tube and microchannel heat exchangers by changing the heat transfer correlation and fin efficiency calculations used. The model is based on scaling the frost layer properties over the entire frost thickness. This approach considers the average properties of the entire layer instead of accounting for local variations inside the layer.

2. The model is implemented as a part of the segment-by-segment heat exchanger solution algorithm, which enables us to predict the variation of frost layer in the direction of refrigerant flow. The model was able to capture the non-uniformity of frost growth due to local surface temperature variations.

3. For a non-uniformly frosted coil, the air flow on the face of the coil redistributes itself to create an equal resistance path through all segments. The model developed was able to handle the redistribution of the air and its effect on the frost growth very well. The error introduced in the frost thickness prediction by neglecting air redistribution phenomenon varied from 20% to 50% depending on the location in the heat exchanger. Accounting for air redistribution phenomenon correctly captured the trend of drop in the coil capacity, while neglecting the phenomenon resulted in a different trend and at the end of the cycle the error was as high as 42%.

4. The model predictions for frost thickness matched the experimentally measured values for all cases except for initial times of low frost growth cases. The model results matched the experimental values within $\pm 5\%$ for most of the cases. During the initial period in low frost growth cases, the model assumption of a uniform heat exchanger surface temperature caused the error

since in reality the frost did not start at the leading edge until after some time. During the low frost growth conditions (low humidity and high temperature), the error in frost thickness was as high as 9.8%.

5. The simple model was not able to predict the frost mass correctly due to assumption that frost grows uniformly over the depth of the heat exchanger. Final frost mass predicted by simple model was 4 times as high as the experimentally measured values.

6. An improved frost growth model which accounts for variation of frost growth in the depth of air flow was developed. The model performed better in capturing the frost initiation delay found for low temperature cases. For the high temperature case the difference between simulated and measured frost thickness during initial stages reduced from 125% to 25%. The improved model also predicted the frost mass on the heat exchanger within 13% for all cases.

7.1.3 System Study

1. Tests were performed on a 3-ton residential heat pump unit with both fin-tube and microchannel heat exchangers as outdoor coil. It was observed that for similar cyclical operating conditions, the unit with microchannel coil went into defrost mode twice as fast as a fin-tube coil. Under dry startup conditions the time for the system with microchannel coil to go into defrost mode was 18% less than similar system with fin-tube coil.

2. Water retention, considered to be the most important factor for faster frost growth in microchannel coils was found to be only of secondary importance. Microchannel coil with Nitrogen blow after defrost performed as badly as a

normal microchannel coil. Removal of water in the coil using nitrogen only increased the length of the frost by one minute. While draining the bulk of water from the coil is beneficial, not much improvement can be gained by draining the coil completely. The primary impact factor in a microchannel coil is the lower operating temperatures and compactness of the heat exchanger. Due to the geometry of the coil and the operating conditions, the face of the coil frosts up rapidly thereby reducing the air flow considerably.

3. In order to effectively incorporate the microchannel heat exchanger in outdoor coil of a heat pump, an holistic redesign including the defrost control strategy needs to be carried out. Using same control strategy for both fin-tube and microchannel results in different degradation of capacity for both cases. It is beneficial to design a control strategy based on the degradation of capacity rather than the outlet refrigerant temperature for microchannel coil.

4. The frost growth model developed in this study is incorporated into a heat pump simulation program. A quasi-steady approach is undertaken to couple the frost model with the vapor compression refrigeration solver algorithm. The model predicted the system parameters very well except for the initial transience period introduced by the compressor. The capacity system is predicted by the model within 6% of the measured value. The frost model predicted the EER of the system within 10% after the transient period.

7.2 Future Work

While the study covered a wide range of topics encountered in the frost growth on outdoor coils, there are still some issues that need to be addressed. A few of the areas which warrants further research are discussed here.

1. More experimental study is required to understand the effect of geometry of microchannel coil on the frost growth. It was observed in this study that for similar operating conditions, the microchannel coil frost up significantly faster than a fin and tube coil. The compactness of the microchannel heat exchanger could be a significant factor. In addition, unlike in a fin and tube coil the leading edge of a microchannel coil is at significantly lower temperature and thus the frost growth is mainly concentrated on the front face of the coil. Studies need to be performed on how the design of the fin can be modified to facilitate deeper penetration of frost and thereby spreading the frost over the entire coil depth.

2. In a non-uniformly frosted coil, current heat transfer coefficient deduction procedure will not work. This is due to the fact that the air flow across the coil is not uniform thereby causing the outlet air temperature to vary over the heat exchanger. In such a case use of an average heat transfer coefficient number will lead to significant error in calculating the capacity. A new data reduction methodology need to be developed to calculate the heat transfer coefficient for a non-uniformly frosted coil from experimental data.

3. The frost growth can be generally assumed to start instantly when the surface temperature is below the dew point and freezing point for any given atmospheric pressure. However when the surface temperatures are close to freezing point, the frost initiation might not be instant. It is possible that water vapor in the air will condense before freezing and causes the local temperatures to change. This might in turn affect the frost growth further. Impact of near freezing surface temperatures on the frost initiation has not been studied rigorously. In order to benefit the frost model, it is desired that an understanding of the frost initiation process from a fundamental physical

perspective be developed.

4. The mechanism of frost initiation at low ambient RH needs to be investigated. The model in it's current form over predicts the frost thickness at low atmospheric RH for both fin-tube and microchannel heat exchangers.

5. Further validation effort is required before adopting the improved frost model presented in this study. Experimental validation of frost thickness profile in the direction of airflow needs to be done in order to validate the results predicted by the improved frost model.

6. It was seen that the frost model was not able to capture the initial system transience occurring due to compressor effects. In order to be able to better predict the average capacity and EER/COP of the system over the entire frost cycle, it is important that we be able to capture the transient effects. Further modeling effort need to be focused on linking the initial system transience effects to the quasi steady state vapor compression cycle simulation.

7. In order for the frost model to be fully applicable for heat pump manufacturers, it is necessary that the model be able to predict the system operation during defrost. The defrost operation is significant since the energy spent during this operation is accounted in the calculation of Heating Seasonal Performance Factor ($HSPF$). While the total energy needed to be spent during defrost can be estimated based on accumulated frost weight, it is not enough since the length of defrost is of extreme importance. Modeling effort need to be concentrated in developing defrost models that can incorporated into a vapor compression cycle simulation. It is also important to be able to simulate different types of defrost control strategies.

8. Further validation of the system model needs to be performed for different

type of systems currently manufactured. This includes various type of expansion devices, different heat exchangers and other heat pump components such as accumulator.

REFERENCES

Ameen, F. (1993), 'Study of frosting of heat pump evaporators', *ASHRAE Transactions* **99**(1), 61 – 71.

ARI (1999*a*), *ARI Standard 540: Positive displacement refrigerant compressor and compressor units*, Air-Conditioning and Refrigeration Institute, Arlington, VA.

ARI (1999*b*), *ARI Std 540: Positive displacement refrigerant compressor and compressor units*, Air-conditioning and refrigeration institute, Arlington, VA.

ARI (2008), *ARI Standard 210/240-2008, Unitary air-conditioning and air-source heat pump equipment*, Air-Conditioning and Refrigeration Institute, Arlington, VA.

ASHRAE (1999), *ANSI/ASHRAE Standard 51-1999, Laboratory Methods of Testing Fans for Aerodynamic Performance Rating*, American Society of Heating Refrigerating and Air-Conditioning Engineers, Atlanta, GA.

ASHRAE (2001), *Standard 41.2-Standard Methods for Laboratory Airflow Measurement*, American Society of Heating Refrigerating and Air-Conditioning Engineers, Atlanta, GA.

ASHRAE (2005), *ASHRAE Hand book - Fundamentals*, American Society of Heating Refrigerating and Air-Conditioning Engineers, Atlanta, GA.

Auracher, H. (1987), 'Effective thermal conductivity of frost', *Heat and Mass Transfer in Refrigeration and Cryogenics* pp. 285–301.

Barrow, H. (1985), 'Note on frosting of heat pump evaporator surfaces', *Journal of Heat Recovery Systems* **5**(3), 195–201.

Biguria, G. and Wenzel, L. A. (1970), 'Measurement and correlation of water frost thermal conductivity and density', *Industrial & Engineering Chemistry Fundamentals* **9**(1), 129–138.

Brian, P., Reid, R. and Brazinsky, I. (1969), 'Cryogenic frost properties', *Cryogenic Technology* **5**, 205–212.

Cai, S. (2009), Design of an experimental facility for measurement of frost growth on heat exchangers, Master's thesis, Oklahoma State University.

Carrol, C. and Peterson, J. (2009), Design and construction of a three-axis traverse system for a image capture in frost experiments, Senior design report, Oklahoma State University.

Chen, H., Thomas, L. and Besant, R. W. (1999), 'Measurement of frost characteristics on heat exchanger fins, part II: Data and analysis', *ASHRAE Transactions* **105**(2), 294–302.

Chen, H., Thomas, L. and Besant, R. W. (2000*a*), 'Modeling frost characteristics on heat exchanger fins: Part I: Numerical model', *ASHRAE Transactions* **106**(2), 357–367.

Chen, H., Thomas, L. and Besant, R. W. (2000*b*), 'Modeling frost characteristics on heat exchanger fins: Part II: Model validation and limitations', *ASHRAE Transactions* **106**(2), 368–376.

Chepurnoi, M. N., Lomakin, V. N., Shnaider, V. E. and Chepurnoi, V. M. (1985), 'Study of the process of frost formation in finned air coolers', *Journal of*

Engineering Physics (English Translation of Inzhenerno-Fizicheskii Zhurnal) **48**(1), 34–37.

Hayashi, Y., Aoki, A., Adachi, S. and Hori, K. (1977a), 'Study of frost properties correlating with frost formation types', *Journal of heat transfer* **99**(2), 239–245.

Hayashi, Y., Aoki, K. and Yuhara, H. (1977b), 'Study of frost formation based on a theoretical model of the frost layer', *Heat transfer. Japanese research* **6**(3), 79–94.

Hern, S. (2004), Design of an experimental facility for hybrid ground source heat pump systems, Master's thesis, Oklahoma State University.

Hosoda and Uzuhashi, H. (1967), 'Effects of frost on the heat transfer coefficient', *Hitachi Rev* **16**(6), 254–259.

Incropera, F. P., DeWitt, D. P., Bergman, T. L. and Lavine, A. S. (2006), *Introduction to Heat Transfer*, 6 edn, John Wiley & Sons Inc.

Iu, I. (2007), Development of Air-to-air Heat Pump Simulation Program with Advanced Heat Exchanger Circuitry Algorithm, PhD thesis, Oklahoma State University.

Jones, B. W. and Parker, J. D. (1974), 'Frost formation with varying environmental paramaters', *American Society of Mechanical Engineers (Paper)* **97(2)**(74-HT-52), 255–259.

Kays, W. M. and London, A. L. (1984), *Compact heat exchangers*, 3 edn, McGraw Hill.

Kim, J. H. and Groll, E. A. (2003), 'Performance comparisons of a unitary split system using microchannel and fin-tube outdoor coils', *ASHRAE Transactions* **109**(2), 219 – 229.

Kim, M, H. and Bullard, C. W. (2002), 'Air-side thermal hydraulic performance of multi-louvered fin aluminum heat exchangers', *International Journal of Refrigeration* **25**, 390400.

Klein, S. and Alvarado, F. (n.d.), *EES: Engineering Equation Solver*, F-Chart Software, Middleton, WI.

Kline, S. J. and McClintock, F. (1953), 'Describing uncertainties in single-sample experiments', *Mechanical Engineering* **75**, 3–8.

Kondepudi, S. N. and O'Neal, D. L. (1987), 'The effects of frost growth on extended surface heat exchanger performance: A review', *ASHRAE Transactions* **93**(2), 258–274.

Kondepudi, S. N. and O'Neal, D. L. (1989), 'Effect of frost growth on the performance of louvered finned tube heat exchangers', *International Journal of Refrigeration* **12**(3), 151–158.

Kondepudi, S. N. and O'Neal, D. L. (1991), 'Frosting performance of tube fin heat exchangers with wavy and corrugated fins', *Experimental Heat Transfer* **4**(5), 613–618.

Kondepudi, S. N. and O'Neal, D. L. (1993), 'Simplified model of pin fin heat exchangers under frosting conditions', *ASHRAE Transactions* **99**, 754–761.

Le Gall, R., Grillot, J. and Jallut, C. (1997), 'Modelling of frost growth and densification', *International Journal of Heat and Mass Transfer* **40**(13), 3177 – 3187.

Lee, Y. and Ro, S. (2001), 'An experimental study of frost formation on a horizontal cylinder under cross flow', *International Journal of Refrigeration* **24**(6), 468 – 474.

Lee, Y. and Ro, S. (2005), 'Analysis of the frost growth on a flat plate by simple models of saturation and supersaturation', *Experimental Thermal and Fluid Science* **29**(6), 685 – 696.

Lock, G. S. H. (1990), *Growth and decay of ice*, Cambridge University Press.

Mao, Y., Besant, R. W. and Rezkallah, K. (1992), 'Measurement and correlations of frost properties with air flow over a flat plate', *ASHRAE Transactions* **98**(2), 65–78.

Martinez-Frias, J. and Aceves, S. (1999), 'Effects of evaporator frosting on the performance of an air-to-air heat pump', *Journal of Energy Resources Technology, Transactions of the ASME* **121**(1), 60 – 65.

Na, B. and Webb, R. L. (2004*a*), 'Mass transfer on and within a frost layer', *International Journal of Heat and Mass Transfer* **47**(5), 899–911.

Na, B. and Webb, R. L. (2004*b*), 'New model for frost growth rate', *International Journal of Heat and Mass Transfer* **47**(5), 925–936.

O'Neal, D. L. (1982), The Effect of Frost Formation of the Performance of Parallel Plate Heat Exchanger, PhD thesis, Purdue University.

O'Neal, D. L. and Tree, D. (1985), 'A review of frost formation in simple geometries', *ASHRAE Transactions* **91**(2a), 267–281.

Östin, R. (1992), 'A study of heat exchange under frosting conditions', *Heat Recovery Systems & CHP* **12**(2), 89–103.

Östin, R. and Andersson, S. (1991), 'Frost growth parameters in a forced air stream', *International Journal of Heat and Mass Transfer* **34**(4-5), 1009–1017.

Padhmanabhan, S., Cremaschi, L., Fisher, D. and Knight, J. (2008), Comparison of frost and defrost performance between microchannel coil and fin-and-tube coil for heat pump systems, *in* 'Proceedings of 12th International Refrigeration and Air Conditioning Conference, Purdue University, West Lafayette, IN'.

Patankar, S. V. (1980), *Numerical Heat Transfer and Fluid Flow*, Taylor & Francis.

Payne, V. and O'Neal, D. L. (2004), 'A mass flow rate correlation for refrigerants and refrigerant mixtures flowing through short tubes', *HVAC&R Research* **10**(1), 73–87.

Robinson, C. M. and Jacobi, A. M. (2001), A study of frost formation on a plain fin, Technical report, Air Conditioning and Refrigeration Center.

Şahin, A., Z. (1994), 'An experimental study on the initiation and growth of frost formation on a horizontal plate', *Experimental Heat Transfer* **7**, 101–119.

Şahin, A., Z. (2000), 'Effective thermal conductivity of frost during the crystal growth period', *International Journal of Heat and Mass Transfer* **43**(4), 539 – 553.

Sanders, C. T. (1974), The influence of frost formation and defrosting on the performance of air coolers, PhD thesis, Technische Hogeschool, Delft (Netherlands).

Schmidt, T. E. (1949), 'Heat transfer calculations for extended surfaces', *Refrigerating Engineering* **57**, 351–357.

Schneider, H. W. (1978), 'Equation of the growth rate of frost forming on cooled surfaces', *International Journal of Heat and Mass Transfer* **21**(8), 1019–1024.

Seker, D., Karatas, H. and Egrican, N. (2004a), 'Frost formation on fin-and-tube heat exchangers. part II - Experimental investigation of frost formation on

fin-and-tube heat exchangers', *International Journal of Refrigeration* **27**(4), 375–377.

Seker, D., Karatas, H. and Egrican, N. (2004b), 'Frost formation on fin-and-tube heat exchangers. part I - Modeling of frost formation on fin-and-tube heat exchangers', *International Journal of Refrigeration* **27**(4), 367–374.

Shah, Y. T. (1968), Theory of frost formation, PhD thesis, Massachusetts Institute of Technology.

Shao, L.-L., Yang, L. and Zhang, C.-L. (2010), 'Comparison of heat pump performance using fin-and-tube and microchannel heat exchangers under frost conditions', *Applied Energy* **87**(4), 1187 – 1197.

Sommers, A. D. and Jacobi, A. M. (2006), 'An exact solution to steady heat conduction in a two-dimensional annulus on a one-dimensional fin: Application to frosted heat exchangers with round tubes', *Journal of Heat Transfer* **128**, 397–404.

Stoecker, W. F. (1957), 'How frost formation on coils affects refrigeration systems', *Refrigeration Engineering* **65**(2), 42–46.

Stoecker, W. F. (1960), 'Frost formation on refrigeration coils', *ASHRAE Transactions* **66**, 91–103.

Storey, B. D. and Jacobi, A. M. (1999), 'The effect of streamwise vortices on the frost growth rate in developing laminar channel flows', *International Journal of Heat Mass Transfer* **42**, 3787–3802.

Tantakitti, C. and Howell, R. H. (1986), 'Air-to-air heat pumps operating under frosting conditions on the outdoor coil', *ASHRAE Transactions* **92**(1B), 827 – 842.

Tao, Y., Besant, R. and Rezkallah, K. (1993), 'A mathematical model for predicting the densification and growth of frost on a flat plate', *International Journal of Heat and Mass Transfer* **36**(2), 353–363.

Tao, Y. X., Besant, R. W. and Mao, Y. (1993), 'Characteristics of frost growth on a flat plate during the early growth period', *ASHRAE Transactions* **99**(1), 746–753.

Thomas, L., Chen, H. and Besant, R. W. (1999), 'Measurement of frost characteristics on heat exchanger fins part i: Test facility and instrumentation', *ASHRAE Transactions* **105**(2), 283–293.

Tso, C. P., Cheng, Y. C. and Lai, A. C. K. (2006), 'An improved model for predicting performance of finned tube heat exchanger under frosting condition, with frost thickness variation along fin', *Applied Thermal Engineering* **26**(1), 111–120.

Wang, C., Lee, C., Chang, C. and Lin, S. (1999), 'Heat transfer and friction correlation for compact louvered fin-and-tube heat exchangers', *International Journal of Heat and Mass Transfer* **42**, 1945–1956.

Xia, Y. and Jacobi, A. M. (2004), 'An exact solution to steady heat conduction in a two-dimensional slab on a one-dimensional fin: application to frosted heat exchangers', *International Journal of Heat and Mass Transfer* **47**(14-16), 3317 – 3326.

Xia, Y. and Jacobi, A. M. (2005), 'Air-side data interpretation and performance analysis for heat exchangers with simultaneous heat and mass transfer: Wet and frosted surfaces', *International Journal of Heat and Mass Transfer* **48**, 5089 5102.

Xia, Y., Zhong, Y., Hrnjak, P. S. and Jacobi, A. M. (2006), 'Frost, defrost, and refrost and its impact on the air-side thermal-hydraulic performance of

louvered-fin, flat-tube heat exchangers', *International Journal of Refrigeration* **29**(7), 1066–1079.

Yan, W.-M., Li, H.-Y. and Tsay, Y.-L. (2005), 'Thermofluid characteristics of frosted finned-tube heat exchangers', *International Journal of Heat and Mass Transfer* **48**(15), 3073–3080.

Yang, D.-K., Lee, K.-S. and Song, S. (2006b), 'Modeling for predicting frosting behavior of a fin-tube heat exchanger', *International Journal of Heat and Mass Transfer* **49**(7-8), 1472–1479.

Yonko, J, D. and Sepsy, C, F. (1967), 'An investigation of the thermal conductivity of frost while forming on a flat horizontal plate.', *ASHRAE Transactions* **73**(2), 2043–2053.

Yun, R., Kim, Y. and Min, M, K. (2002), 'Modeling of frost growth and frost properties with airflow over a flat plate', *International Journal of Refrigeration* **25**(3), 362–371.

APPENDIX A

Property Calculation Routines

A.1 Binary Diffusion coefficient

Binary diffusion coefficient for water vapor from air to frost layer is given by

$$D_{AB} = 2.302 \frac{P_0}{P_{sat}} \left(\frac{T_a}{T_0} \right)^{1.81} \times 0.00001 \tag{A.1}$$

where D_{AB} = Binary diffusion coefficient

T_a = Air temperature [K]

P_{sat} = Saturation pressure of water vapor at air temperature [Pa]

T_0 = Reference temperature ($= 256K$)

P_0 = Reference pressure ($= 0.98 \times 10^5$ Pa)

A.2 Enthalpy of Ablimation for Water Vapor

Enthalpy of ablimation of water from vapor phase to solid phase is given by

$$h_{sg} = (h_v - h_s) \times 1000 \tag{A.2}$$

where h_{sg} = Enthalpy of ablimation [J/kg]

h_v = Enthalpy of water in vapor phase [kJ/kg]

h_s = Enthalpy of water in solid phase [kJ/kg]

The enthalpy of water in vapor phase in air is given as

$$h_v = A(1) + A(2)T_a + A(3)T_a^2 + A(4)T_a^3 + A(5)T_a^4 + A(6)T_a^5 - RT_a^2 * dBP_{ice} \quad \text{(A.3)}$$

$$h_s = B(1) + B(2)T_a + D(3)T_a^2 + D(4)T_a^3 + D(5)P_{ice} \quad \text{(A.4)}$$

where T_a = Air temperature [K]

R = Gas constant

The constant arrays A and B are given as:

$$A = \begin{pmatrix} 1997.98 \\ 1.8035706 \\ 3.6400463 \times 10^{-4} \\ 1.4677622 \times 10^{-6} \\ 2.872661 \times 10^{-9} \\ -1.751 \times 10^{-12} \end{pmatrix} \quad B = \begin{pmatrix} -647.595 \\ 0.274292 \\ 2.910583 \times 10^{-3} \\ 1.083437 \times 10^{-6} \\ 1.07 \times 10^{-6} \end{pmatrix} \quad \text{(A.5)}$$

The other parameters used in the equation are calculated as

$$dB = 1.47184 \times 10^{-9} \frac{1734.29}{T_a^2} \exp\left(\frac{1734.29}{T_a}\right) \quad \text{(A.6)}$$

$$P_{ice} = 661.36 \exp(0.09575 T_{a,c}) \text{ where } T_{a,c} = \text{Air temperature [C]} \quad \text{(A.7)}$$

APPENDIX B

Fin Efficiency and Heat Transfer Coefficient Estimation for Frosted Microchannel HX

B.1 EES Program

Fin parameters

$$k_{fi} = 222 \tag{B.1}$$

$$\delta_{fi} = 0.00011 \tag{B.2}$$

$$H_f = 0.00757 \tag{B.3}$$

Heat Transfer coefficient

$$h_r = Nu_r k_r / D_r \tag{B.4}$$

Microchannel port diameter for refrigerant flow

$$D_r = 0.0012725 \tag{B.5}$$

Coil dimensions

$$Nl = 1 \tag{B.6}$$

$$Nt = 47 \tag{B.7}$$

$$L_{coil} = NlNtL_{tube} \tag{B.8}$$

$$H_{tube} = 0.0012954 \tag{B.9}$$

$$Depth_{tube} = 0.0254 \tag{B.10}$$

$$L_{tube} = 0.3048 \tag{B.11}$$

$$FP = 787 \tag{B.12}$$

Air & Refrigerant specific heats

$$cp_r = 3120 \tag{B.13}$$

$$cp_a = \mathrm{c_p}\left(AirH2O,\ \mathrm{P} = 101.325,\ \mathrm{T} = Tai,\ \mathrm{R} = 0.82\right) 1000 \tag{B.14}$$

Various areas associated in heat transfer calculations

$$A_r = 4 \cdot \pi D_r L_{tube} Nt \tag{B.15}$$

$$A_{br} = \left(\pi H_{tube} + Depth_{tube} 2\right) L_{coil} Nt \tag{B.16}$$

$$A_{fi} = 2\left(\left(\delta_{fi} + 2\delta_{fr}\right) + Depth_{tube}\right) H_f FPL_{coil} \tag{B.17}$$

$$A_{bs} = A_{br} - 2\left(\delta_{fi} + 2\delta_{fr}\right) Depth_{tube} FPL_{coil} \tag{B.18}$$

$$A_h = A_{bs} + A_{fi} \tag{B.19}$$

LMTD of counterflow HX with given inlet and outlet temperatures

$$dT_{lmcf} = \frac{\left(T_{ao} - T_{ri}\right) - \left(T_{ai} - T_{ro}\right)}{\ln\left(\frac{T_{ao} - T_{ri}}{T_{ai} - T_{ro}}\right)} \tag{B.20}$$

Calculate the correction factor for LMTD

$$P = \frac{T_{ro} - T_{ri}}{T_{ai} - T_{ri}} \tag{B.21}$$

$$R = \frac{T_{ai} - T_{ao}}{T_{ro} - T_{ri}} \tag{B.22}$$

$$F_{HX} = LMTD_{CF}(\text{`crossflow\_one\_unmixed'} \ , \ P, \ R) \tag{B.23}$$

Final LMTD for the test HX

$$dT_{lm} = dT_{lmcf} F_{HX} \tag{B.24}$$

Frost density and conductivity

$$\rho_{fs} = 670 \exp\left(0.277 T_{fs}\right) \tag{B.25}$$

$$k_{fr} = 0.132 + 3.13 \times 10^{-4} \rho_{fs} + 1.6 \times 10^{-7} \left(\rho_{fs}\right)^2 \tag{B.26}$$

Measured total and sensible capacity

$$Q_a = mdot_r cp_r ABS\left((T_{ro} - T_{ri})\right) \tag{B.27}$$

$$Q_{as} = mdot_a cp_a ABS\left((T_{ao} - T_{ai})\right) \tag{B.28}$$

Sander's Method - 1D conduction

$$UA_a = Q_{as}/dT_{lm} \tag{B.29}$$

$$UA_{a,sanders} = Q_{as}/dT_{lm} \tag{B.30}$$

Parameters for enthalpy correlation (against temperature) as presented by Sanders

$$a_0 = 9439 \tag{B.31}$$

$$b_0 = 1693 \tag{B.32}$$

Fin efficiency parameter - Sander's formulation

$$mfr = \sqrt{\frac{1}{\frac{\delta_{fr}}{k_{fr}} + \frac{cp_a}{\left(h_{a,sanders} b_0\right)}} \frac{1}{\left(\delta_{fi} k_{fi}\right)}} \tag{B.33}$$

Final fin efficiency and surface effectiveness - Sander's formulation

$$\eta_{sanders} = \frac{\tanh\left(mfrH_f/2\right)}{mfrH_f/2} \tag{B.34}$$

$$\eta_{s,sanders} = \eta_{sanders}\left(A_{fi}/A_h\right) + \left(\frac{\frac{k_{fr}}{\delta_{fr}}}{h_{a,sanders}\left(Q_a/Q_{as}\right) + \frac{k_{fr}}{\delta_{fr}}}\right)\left(\frac{A_h - A_{fi}}{A_h}\right) \tag{B.35}$$

Overall heat transfer coefficient

$$1/UA_{a,sanders} = \frac{1}{\eta_{s,sanders} h_{a,sanders} A_h} + \frac{1}{h_r A_r \left(Q_{as}/Q_a\right)} \tag{B.36}$$

Xia's Method - 2D conduction

Calculate the λ factor

$$\lambda_{num} = h_a\left(Q_a/Q_{as}\right) \tag{B.37}$$

$$\lambda_{denom} = k_{fi}\frac{\delta_{fi}}{2} + \delta_{fr}\left(k_{fi} h_a\left(Q_a/Q_{as}\right)\frac{\frac{\delta_{fi}}{2}}{k_{fr}} + k_{fr}\right) \tag{B.38}$$

$$\lambda = \delta_{fr}\sqrt{\lambda_{num}/\lambda_{denom}} \tag{B.39}$$

Final fin efficiency and surface effectiveness - Xia's formulation

$$\eta = 2\frac{\lambda}{h_a\left(Q_a/Q_{as}\right)H_f\delta_{fr}}\left(k_{fi}\frac{\delta_{fi}}{2}+k_{fr}\delta_{fr}\right)\tanh\left(\lambda\frac{H_f}{2\delta_{fr}}\right) \tag{B.40}$$

$$\eta_s = \eta\left(A_{fi}/A_h\right)+\left(\frac{\frac{k_{fr}}{\delta_{fr}}}{h_a\left(Q_a/Q_{as}\right)+\frac{k_{fr}}{\delta_{fr}}}\right)\left(\frac{A_h-A_{fi}}{A_h}\right) \tag{B.41}$$

Overall heat transfer coefficient

$$1/UA_a = \frac{1}{\eta_s h_a A_h}+\frac{1}{h_r A_r\left(Q_{as}/Q_a\right)} \tag{B.42}$$

VITA

Sankar Padhmanabhan

Candidate for the Degree of

Doctor of Philosophy

Dissertation: Study of Frost Growth on Heat Exchangers Used as Outdoor Coils in Air Source heat Pump Systems

Major Field: Mechanical Engineering

Biographical:

Personal Data: Born in Palakkad, Kerala, India on Feb 03, 1980.

Education: Received the B.S. degree in Mechanical Engineering from Regional Engineering College (Now National Institute of Technology), Durgapur, W.B, India in May 2001. Received the M.S. degree in Mechanical Engineering from Oklahoma State University, Stillwater, OK, USA in May 2005. Completed the requirements for the degree of Doctor of Philosophy with a major in your Mechanical Engineering from Oklahoma State University, Stillwater, OK, USA in May 2011.

Experience: Employed as Research Assistant in the School of Mechanical & Aerospace Engineering, Oklahoma State University, Stillwater, Oklahoma from Jan 2002 to Dec 2004 and from Feb 2007 to Dec 2011. Employed as Research Engineer in the School of Mechanical & Aerospace Engineering, Oklahoma State University, Stillwater, Oklahoma from Jan 2005 to Feb 2007. Currently employed as Heat Transfer Engineer in the heat Transfer center of Excellence at Johnson Controls Inc.

Professional Memberships: American Society of Heating, Refrigerating and Air-Conditioning Engineers (ASHRAE), International Building Performance Simulation Association (IBPSA).

Name: Sankaranarayanan Padhmanabhan Date of Degree: May, 2011

Institution: Oklahoma State University Location: Stillwater, Oklahoma

Title of Study: Study of Frost Growth on Heat Exchangers Used as Outdoor Coils in Air Source heat Pump Systems

Pages in Study: 188 Candidate for the Degree of Doctor of Philosophy

Major Field: Mechanical & Aerospace Engineering

Scope and Method of Study: During winter heating operation, the outdoor coil of a heat pump acts as an evaporator and when the ambient temperature is near freezing, the moisture in the atmospheric air freezes on the coil surface. The frost growth affects the air flow and also adds resistance to heat transfer thus reducing the capacity and the efficiency of the heat pump. An experimental facility is designed and built to test a small scale heat exchanger working in frosting conditions. Tests are carried out using small scale fin-tube and microchannel heat exchanger over a range of glycol inlet temperatures, air velocities and ambient air RH. A semi-empirical frost model based on a scaling approach is developed and applied to both fin-tube heat and microchannel heat exchangers. The model is developed to handle non-uniformities in both refrigerant and air side. The frost model is integrated with a segment-by-segment heat exchanger calculation algorithm and is validated against experimental data. Frost growth model is also incorporated in a quasi-steady state system simulation algorithm.

Findings and Conclusions: From the experimental study it was observed that the temperature of the surface and air RH affected the rate of frost growth significantly while the air velocity did not have a great influence. It is demonstrated that a dry heat transfer correlation can be used during frost growth period by correctly accounting for frost thickness in the hydraulic diameter calculations. Ignoring the phenomenon of air redistribution was found to result in errors in the range of 20% to 50% in predicted frost thickness. Frost thickness predicted by the frost model is within 5% of the measured values for most of the cases. Frost mass accumulation predicted by the simple model is higher than the measured values due to a uniform thickness assumption in the model. An improved frost model based on 1-D finite volume discretization is also presented which improved the frost mass prediction to within 13% of measured values. The system simulation is validated against experimental results and found to match reasonable well. The discrepancy between simulation and experiments were due to the effects of system transience in the initial stages.

ADVISOR'S APPROVAL: _____